Spontaneous Optical Patterns in Two and Four Level Atomic Systems

Andrew Joseph Scroggie

Thesis submitted for the degree of

Doctor of Philosophy

in the Department of Physics and Applied Physics

University of Strathclyde

Glasgow January 1995

ABSTRACT

The emergence of spatio–temporal structures (patterns) in dissipative systems has generated a great deal of interest, especially in recent years when the increased power of computers has allowed the numerical investigation of simple models of such systems in two spatial dimensions plus time. In this thesis we examine pattern formation in the context of two nonlinear optical systems: a two–level medium in a ring cavity and a four–level medium with feedback mirror. In both systems we use a combination of linear and weakly nonlinear analysis and numerical integration to identify parameter values where patterns are expected and to investigate the questions of pattern selection and stability.

In the ring cavity we find that the system shows the formation of, and competition between, roll, hexagon and inverted hexagon ("honeycomb") patterns close to threshold. As well as the three types of patterns displayed by the ring cavity the feedback mirror system is able to produce squares and rhomboids for appropriate parameter values. Finally, in the ring cavity we are able to show the existence of solitary–wave structures in both one and two dimensions and to demonstrate a technique for their control as bits in a possible optical memory.

Acknowledgments

I would like to thank all the people (too many to name individually) from whose advice and friendship I have benefited in the past three years. I am particularly grateful to Graeme Harkness for his assistance with all things computational, and to my supervisor Willie Firth without whose ideas, enthusiasm, patience and encouragement this thesis would never have been written. Finally I thank my parents for their support (in every sense) throughout the time that it's taken to get this far.

Contents

Chapter 1

Introduction

A simple first approximation which can be made in the study of nonlinear optical systems is that the fields involved are plane–waves: that is, fields with a well-defined direction of propagation and no structure in the plane transverse to that direction. In the past decade or so, however, the important realisation has been made that the complicated dynamics of the field–medium interaction which exists in a nonlinear optical system can introduce spontaneous symmetry breaking through the formation of patterns, either stationary or time–dependent, in the transverse plane. The implication is that even a plane–wave pump does not necessarily mean plane–wave fields. Of course plane–waves are themselves only idealisations of the physically meaningful situation of beams with finite transverse extent; but when the ratio of the beam width to the length scale of the pattern (the aspect ratio) is even moderately large a plane–wave analysis should still have relevance. The experimental and numerical observation of patterns in the presence of gaussian beam pumps bear this out.

Transitions (or bifurcations) from a homogeneous state to one with structure have been observed in other branches of science when a dissipative system with a mechanism for coupling different spatial points is subjected to external forcing [1] *and op. cit.*. In optics spatial coupling is provided by diffraction, or a combination of diffraction and diffusion in the medium, while the forcing is due either to the

incoherent pumping of the population inversion present in lasers or to the coherent pumping by one or more external fields which drives passive media. Whatever the system under consideration, though, the emphasis in optics, as in other fields, is on simple models which capture the pattern–forming behaviour.

In passive systems, which are the subject of this thesis, a number of different configurations have proved suitable for the study of pattern formation. Nonlinear media in optical cavities have been of interest not least because of their importance in work on optical bistability [2]; in fact the earliest theoretical investigations of pattern–forming behaviour were carried out by Moloney and co–workers in the context of mapping models of nonlinear cavities [3, 4]. Their studies of Kerr and saturable Kerr media showed the formation of solitary–wave structures in one transverse dimension, while in two transverse dimensions the breakup of rings into dynamic patterns of spots was observed. Later work by McDonald and Firth [5] showed that the one–dimensional solitary waves could be selectively addressed and thus, in principle, form the basis of an optical memory.

One simplifying approach which has been employed in cavity problems is the elimination of the propagation direction through the application of the mean field limit [6]. The technique applies to high–finesse cavities in which the effect of the medium on a single pass is small, and relies on the assumption that in such cases the changes along the propagation direction can effectively be integrated out. Theoretical investigations of mean field models have predicted the formation of many of the different planforms from which a rotationally invariant system can select when its homogeneous state becomes unstable. A two–level medium in a cavity has been shown to form stripes (rolls), hexagons and inverted hexagons ("honeycombs"), both under conditions of fast relaxation of the atomic variables (the good cavity limit) [7] and in the region of nascent optical bistability [8, 9]. Studies involving Kerr media [10–12] predict the formation of either hexagons in self–focusing media [11] or rolls, via a polarisation instability, in defocusing media [12]. Despite much theoretical work, however, experimental investigation of cavity patterns has been lacking to date, with the exception of [13] whose results are in any case difficult to interpret: the earlier work in optical bistability

was arranged to frustrate transverse effects rather than encourage them.

The problem of counterpropagating beams in a nonlinear medium, on the other hand, yielded the first experimental observation of hexagons in nonlinear optics in the work of Grynberg and co–workers [14] and later of Pender and Hesselink [15] both in sodium vapour, with later work done by the former on rubidium vapour [16]. Work on the corresponding theoretical problem, restricted to consideration of Kerr–like media, has been extensive [17–23]. The prediction of a pattern–forming instability and numerical observation of hexagonal patterns in focusing media, with both plane–wave [23] and gaussian–beam pumps [22], have been encouraging. The impossibility of eliminating the propagation direction from the problem, however, has meant that it is very difficult to work with, both analytically and computationally. Even a restriction to the case where both input fields are plane waves of the same intensity, while allowing the use of symmetry arguments to predict the formation of hexagons in focusing media and of squares in defocusing media [23], does little to increase the tractability of the problem.

A simpler system devised to remove the difficulties inherent in counterpropagation consists of a thin slice of Kerr material separated from a feedback mirror by a region of free space [24]. The propagation direction is still important, in that diffraction is necessary to convert the phase–modulation of the input field into an amplitude modulation which drives the medium. The thin slice assumption, though, means that the propagation direction only involves free space and is thus fairly easy to handle mathematically; in fact, it can be entirely removed from the problem by integration of the equations. Analysis of this system in the plane–wave limit [24, 25] predicted an instability leading to the formation of hexagons while computations carried out with a narrow gaussian input beam [26] showed that patterns of spots may appear with other than hexagonal symmetry.

The simplicity of the feedback mirror system has made it attractive from an experimental point of view as well; several experiments have already demonstrated pattern formation using either a liquid crystal [27, 28] or the hybrid liquid crystal light valve (LCLV) [29–33] as a Kerr–like material. The large Kerr coefficient of

the latter means that high enough power over a large enough area can be obtained to view medium to large aspect ratio patterns. Experiments carried out with the LCLV have thus been able to confirm predictions derived on the basis of the plane–wave analysis: the formation of hexagons and the intrinsic length scale of the pattern [29–31]. With the introduction of a rotation in the field during the free space propagation it has also been shown experimentally [31] that rolls and honeycombs can be seen as well as hexagons. In addition, a theoretical and experimental investigation of the régimes in which the LCLV deviates from Kerr–like behaviour [33] has indicated a very complicated bifurcation structure and the existence of rolls, hexagons of both types and also many more unusual solutions. Feedback mirror sytems have therefore proved a source of both useful comparison between theory and experiment and of varied and interesting pattern–forming behaviour.

This brief review of a few of the areas of interest in transverse pattern formation in passive nonlinear optics will now hopefully serve to place the work presented here in some sort of context. We begin in Chapter 2 by showing how we derive the type of coupled field–material equations which we will subsequently use to model nonlinear optical systems. We also show how the mean–field limit is applied in cavity problems to eliminate the propagation direction from the equations. The following chapter considers such a mean–field model of a two–level medium in a ring cavity. A combination of weakly nonlinear analysis and numerical integration allows us to predict and observe the existence of stable hexagon, roll and honeycomb patterns for different parameter values.

In Chapter 4 we go on to examine a feedback mirror system where the nonlinear medium is an alkali vapour rather than a Kerr–like material. Experiments on such systems have already been performed by Grynberg and co–workers [34] with rubidium vapour and by Ackemann and Lange [35] with sodium vapour, both showing the formation of transverse patterns. We find that this time the system is able to form squares and rhomboids as well as rolls, hexagons and honeycombs for appropriate parameter values.

Finally in Chapter 5 we return to the two–level ring cavity problem and use the knowledge gained in Chapter 3 to investigate a different type of solution from the pure patterns examined in the previous chapters. These consist of isolated regions of the pattern embedded in a background of a homogeneous solution. After studying such solutions in both one and two dimensions we finish by suggesting a method for their control in a possible optical memory.

Chapter 2

Mean-Field Maxwell-Bloch Equations

2.1 Introduction

Our aim is to investigate some of the aspects of the interaction of intense, coherent optical fields with collections of atoms, and to do this we require mathematical models of the systems which we will be examining. The purpose of this chapter is therefore to derive coupled matter–field equations appropriate to the problems which we will deal with in subsequent chapters. In deriving these equations we will introduce simplifying approximations based on our understanding of the physical processes taking place, in order to develop a model which is reasonably tractable mathematically, but which still captures the relevant physics. In particular, we adopt a semiclassical approach in which the optical field is treated classically and the material is described using quantum mechanics. It should be stressed that the emphasis in this derivation is not on mathematical rigour, but rather on providing reasonable justification for models whose usefulness in this field has already been demonstrated.

We begin in Section 2.2 with Maxwell's Equations and using known properties of

the fields generated by lasers, we arrive at a single, simplified partial differential equation for the slowly–varying amplitude of the electric field.

Section 2.3 deals with the description of the material variables. Using a simple quantum mechanical model we derive equations for a two–level system coupled to the optical field through an electric dipole interaction. The investigation of this system is the subject of two chapters of this thesis. At the same time, the procedure used in deriving these equations is general and will be used again in Chapter 4 where we deal with the more complicated situation of a four–level system interacting with two optical fields.

Having derived equations for a system consisting of a field coupled to a two–level medium, in Section 2.4 we place the medium in an optical cavity and use a mean field approach to eliminate one of the spatial dimensions from the problem. The resulting mean field Maxwell–Bloch equations will be the starting point for the work in Chapters 3 and 5.

2.2 The Field Equation

We begin with Maxwell's Equations:

$$\nabla \times \mathbf{E} = -\frac{\partial \mathbf{B}}{\partial t} \tag{2.1}$$

$$\nabla \cdot \mathbf{D} = \rho_f \tag{2.2}$$

$$\nabla \times \mathbf{H} = \mathbf{j}_f + \frac{\partial \mathbf{D}}{\partial t} \tag{2.3}$$

$$\nabla \cdot \mathbf{B} = 0 \tag{2.4}$$

$$\mathbf{D} = \epsilon_0 \mathbf{E} + \mathbf{P} \tag{2.5}$$

$$\mathbf{B} = \mu_0 \mathbf{H} + \mathbf{M} \tag{2.6}$$

where $\mathbf{E}$ is the electric field, $\mathbf{H}$ is the magnetic field, $\mathbf{D}$ and $\mathbf{B}$ are the electric and magnetic flux densities respectively, $\mathbf{P}$ is the polarisation and $\mathbf{M}$ is the magnetisation. ρ_f is the density of free charge and $\mathbf{j}_f$ is the free charge current density.

We will be dealing with non–magnetic media which have no free charge so from now on we assume that $\mathbf{M} = \mathbf{j}_f = \mathbf{0}$ and $\rho_f = 0$.

Operating on (2.1) with the vector operator $\nabla\times$ and using (2.3) ,(2.5) and (2.6) we obtain the following equation

$$\nabla(\nabla \cdot \mathbf{E}) - \nabla^2\mathbf{E} = -\frac{1}{c^2}\frac{\partial^2\mathbf{E}}{\partial t^2} - \mu_0\frac{\partial^2\mathbf{P}}{\partial t^2} \tag{2.7}$$

where we have used the operator identity $\nabla \times \nabla\times = \nabla(\nabla\cdot) - \nabla^2$. In free space (2.7) reduces to the wave equation.

Since we will be dealing in this thesis with passive systems driven by an external C.W. laser field, and since such fields can be well described as slowly modulated monochromatic wave trains (the Slowly Varying Envelope Approximation or S.V.E.A.) we write the electric field, $\mathbf{E}$, and polarisation, $\mathbf{P}$, in the form

$$\begin{aligned}
\mathbf{E} &= \mathbf{F}e^{i(kz-\omega t)} + c.c. \\
&= (\mathbf{F}_\perp + F_z\mathbf{k})e^{i(kz-\omega t)} + c.c. \\
\mathbf{P} &= \mathbf{P}e^{i(kz-\omega t)} + c.c. \\
&= (\mathbf{P}_\perp + P_z\mathbf{k})e^{i(kz-\omega t)} + c.c.
\end{aligned} \tag{2.8}$$

$\mathbf{k}$ is a unit vector parallel to the direction of propagation of the field. For later convenience the fields have been separated into a transverse part (perpendicular to $\mathbf{k}$) and a longitudinal part (parallel to $\mathbf{k}$).

Adapting the approach of [36], we aim to use (2.8) to reduce (2.7) to a simpler form by eliminating higher derivatives in a consistent way. To do this, though, it is necessary to know typical time and length scales for the variation of the slowly varying amplitude $\mathbf{F}$ of the field. If $\mathbf{F}$ has a maximum transverse wavevector K_{max} then a length scale for the transverse variables, x and y, is given by $\Lambda = 2\pi/K_{max}$. The longitudinal length scale can be obtained by considering Equation (2.7) in free space. If we substitute (2.8) into (2.7) then, as long as the phenomena considered do not involve changes on the scale of either an optical wavelength or an optical period, we can assume

$$\left|\frac{\partial^2\mathbf{F}}{\partial t^2}\right| \ll \omega\left|\frac{\partial\mathbf{F}}{\partial t}\right|, \quad \left|\frac{\partial^2\mathbf{F}}{\partial z^2}\right| \ll k\left|\frac{\partial\mathbf{F}}{\partial z}\right|. \tag{2.9}$$

Since the situations considered in this thesis only involve CW fields we can neglect the second order derivatives in z and t. We then have that $\mathbf{F}$ obeys

$$\frac{\partial \mathbf{F}}{\partial z} + \frac{1}{c}\frac{\partial \mathbf{F}}{\partial t} = \frac{i}{2k}\nabla_\perp^2 \mathbf{F} \tag{2.10}$$

where $\nabla_\perp^2 = \partial_{x^2} + \partial_{y^2}$. Neglecting the terms in ∂_{z^2} and ∂_{t^2} is equivalent to assuming that the curvature of the wave–fronts is small which is another way of saying that K_{max} is much smaller than k. This is known as the paraxial approximation. Equation (2.10) then defines typical length and time scales, l and τ, for $\mathbf{F}$ as the propagation distance or time over which a phase–shift of $O(1)$ occurs. Specifically we choose

$$l = \frac{4k\pi^2}{K_{max}^2} = k\Lambda^2, \qquad \tau = \frac{l}{c}. \tag{2.11}$$

In this way the paraxial approximation defines a natural smallness parameter, ε, for assessing the relative magnitude of the various spatial and temporal derivatives in Equation (2.7):

$$\varepsilon = \frac{\Lambda}{l} = \frac{1}{k\Lambda}. \tag{2.12}$$

We rescale the independent variables in terms of their natural scales

$$x \to \frac{x}{\Lambda}, \quad y \to \frac{y}{\Lambda}, \quad z \to \frac{z}{l}, \quad t \to \frac{t}{\tau}. \tag{2.13}$$

Then, using the definition of ε, and splitting Equation (2.7) into transverse and longitudinal parts, we obtain

$$\nabla_\perp \left(\varepsilon^2 \nabla_\perp \cdot \mathbf{F}_\perp + i\varepsilon F_z + \varepsilon^3 \frac{\partial F_z}{\partial z}\right) - \varepsilon^2 \nabla_\perp^2 \mathbf{F}_\perp - \varepsilon^4 \frac{\partial^2 \mathbf{F}_\perp}{\partial z^2} - 2i\varepsilon^2 \frac{\partial \mathbf{F}_\perp}{\partial z} =$$

$$-\varepsilon^4 \frac{\partial^2 \mathbf{F}_\perp}{\partial t^2} + 2i\varepsilon^2 \frac{\partial \mathbf{F}_\perp}{\partial t} - \mu_0 c^2 \left[\varepsilon^4 \frac{\partial^2 \mathbf{P}_\perp}{\partial t^2} - 2i\varepsilon^2 \frac{\partial \mathbf{P}_\perp}{\partial t} - \mathbf{P}_\perp\right] \tag{2.14}$$

for the transverse part and

$$\varepsilon^3 \frac{\partial}{\partial z}(\nabla_\perp \cdot \mathbf{F}_\perp) + i\varepsilon \nabla_\perp \cdot \mathbf{F}_\perp - \varepsilon^2 \nabla_\perp^2 F_z =$$

$$-\varepsilon^4 \frac{\partial^2 F_z}{\partial t^2} + 2i\varepsilon^2 \frac{\partial F_z}{\partial t} + F_z - \mu_0 c^2 \left[\varepsilon^4 \frac{\partial^2 P_z}{\partial t^2} - 2i\varepsilon^2 \frac{\partial P_z}{\partial t} - P_z\right] \tag{2.15}$$

for the longitudinal part.

We expand the fields in terms of ε

$$\begin{aligned}
\mathbf{F}_\perp &= \mathbf{F}_\perp^{(0)} + \varepsilon \mathbf{F}_\perp^{(1)} + \varepsilon^2 \mathbf{F}_\perp^{(2)} + \ldots \\
F_z &= F_z^{(0)} + \varepsilon F_z^{(1)} + \varepsilon^2 F_z^{(2)} + \ldots \\
\mathbf{P}_\perp &= \varepsilon^2 \mathbf{P}_\perp^{(0)} + \varepsilon^3 \mathbf{P}_\perp^{(1)} + \ldots \\
P_z &= \varepsilon^2 P_z^{(0)} + \varepsilon^3 P_z^{(1)} + \ldots
\end{aligned} \tag{2.16}$$

The choice $|\mathbf{P}| = O(\varepsilon^2)$ will be justified in Section 2.3.4.

We now collect the terms in (2.14) and (2.15) at each order in ε. At $O(\varepsilon^0)$ we find

$$F_z = 0. \tag{2.17}$$

This shows that to lowest order the field is purely transverse, although higher order longitudinal corrections must be added to ensure that the field will satisfy Maxwell's Equations.

At $O(\varepsilon)$ we get

$$F_z^{(1)} = i\nabla_\perp \cdot \mathbf{F}_\perp^{(0)} \tag{2.18}$$

$$\nabla_\perp^2 \mathbf{F}_\perp^{(0)} + 2i\frac{\partial \mathbf{F}_\perp^{(0)}}{\partial z} + 2i\frac{\partial \mathbf{F}_\perp^{(0)}}{\partial t} = -\frac{1}{\epsilon_0}\mathbf{P}_\perp^{(0)}. \tag{2.19}$$

At this order we produce a non–trivial equation describing the spatio–temporal evolution of the transverse field, $\mathbf{F}_\perp^{(0)}$, and its coupling to the material via the source term in $\mathbf{P}_\perp^{(0)}$. Undoing the scalings by performing the inverse of transformations (2.13) and (2.16) and dropping the subscripts on the field variables, we arrive at our simplified Maxwell equation

$$\nabla^2 \mathbf{F} + 2ik\left(\frac{\partial \mathbf{F}}{\partial z} + \frac{1}{c}\frac{\partial \mathbf{F}}{\partial t}\right) = -\mu_0 \omega^2 \mathbf{P}. \tag{2.20}$$

2.3 The Medium

2.3.1 Bloch Equations

Having derived an equation describing the dependence of the electric field on the material we must now describe the behaviour of the medium and its dependence on the field. We assume that each atom [†] in the medium can be described by a quantum mechanical state–vector, $|\Psi\rangle$, whose evolution is governed by the time–dependent Schrödinger equation

$$i\hbar\frac{\partial|\Psi\rangle}{\partial t} = \hat{H}|\Psi\rangle \tag{2.21}$$

$$\hat{H} = \hat{H}_0 + \hat{H}_I \tag{2.22}$$

where $\hat{H}$ is the Hamiltonian operator for the system, $\hat{H}_0$ is the Hamiltonian in the absence of an external field and $\hat{H}_I$ describes the field/atom interaction.

We assume that the medium interacts with the field through an electric dipole interaction so that $\hat{H}_I$ can be written as

$$\hat{H}_I = e\sum_{i=1}^{N}\mathbf{E}.\mathbf{r} = e\mathbf{E}.\sum_{i=1}^{N}\mathbf{r} = -\mathbf{E}.\boldsymbol{\mu} \tag{2.23}$$

where the sum is over the electron co–ordinates and $\boldsymbol{\mu}$ is the electric dipole moment of the atom. We have used the fact that for optical frequencies $\mathbf{E}$ will not vary significantly over atomic distances since $E \sim e^{\pm ikz}$ and $kz \ll 1$. For typical values of $|\mathbf{E}|$ and $|\mathbf{r}|$ (e.g. $E \sim 10^3$ to $10^6 \mathrm{Vm}^{-1}$ and $r \simeq 10^{-10}\mathrm{m}$) this means that the effect of the external field is small compared with the potential energy terms already present in the system (for example the Coulomb potential for an electron in an atom). We may therefore treat $\hat{H}_I$ as a small perturbation to $\hat{H}_0$, and write the solution, $|\Psi\rangle$, to the perturbed problem as

$$|\Psi(t)\rangle = \sum_{i=1}^{N} a_i(t)|\psi_i\rangle \tag{2.24}$$

[†] In principle we could be describing some quantum mechanical system other than an atom; we use the word "atom" for definiteness.

where the $\{|\psi_i\rangle\}$ are an orthonormal basis for solutions to the time–independent eigenvalue problem

$$\hat{H}_0|\psi_i\rangle = E_i|\psi_i\rangle \tag{2.25}$$

that is

$$\langle\psi_i|\psi_j\rangle = \delta_{ij}. \tag{2.26}$$

Using the definition of the macroscopic polarisation, $\mathbf{P}$, as the dipole moment per unit volume, and writing n_a for the number density of atoms in the system, we have

$$\mathbf{P} = -n_a e\langle\Psi|\mathbf{r}|\Psi\rangle = n_a \sum_{jk} \rho_{jk}\boldsymbol{\mu}_{kj} = n_a Tr(\boldsymbol{\mu}\rho) \tag{2.27}$$

where the $\boldsymbol{\mu}_{kj}$ are matrix elements of the electric dipole operator

$$\boldsymbol{\mu}_{kj} = \langle\psi_k|\boldsymbol{\mu}|\psi_j\rangle \tag{2.28}$$

and $\rho_{jk} = a_j a_k^*$ are matrix elements of the density operator $\hat{\rho}$ [37]; it is these, rather than the $\{a_j\}$ which correspond to observable quantities. In fact, from (2.27) we see that we can describe the polarisation by writing down evolution equations for the matrix elements of $\hat{\rho}$. This can be done by substituting (2.24) into (2.21) and using the definition of $\hat{H}_I$ and $\boldsymbol{\mu}$ (Equations (2.23) and (2.28)) and the orthonormality of the $\{\psi_i\}$. We get

$$\partial_t \rho_{jk} = -i\omega_{jk}\rho_{jk} + \frac{i\mathbf{E}}{\hbar} \cdot \sum_{l=1}^{N} \boldsymbol{\mu}_{jl}\rho_{lk} - \frac{i\mathbf{E}}{\hbar} \cdot \sum_{l=1}^{N} \boldsymbol{\mu}_{lk}\rho_{jl} \tag{2.29}$$

where $\omega_{jk} = (E_j - E_k)/\hbar$.

We remark at this point that the diagonal elements of $\boldsymbol{\mu}$ ($\{\boldsymbol{\mu}_{ii}\}$) are identically zero since for these quantities the implied integrand in (2.28) has overall odd parity and vanishes when integrated over all space. Thus the definition of $\mathbf{P}$ involves only off-diagonal matrix elements of $\hat{\rho}$. The diagonal elements ρ_{ii} of $\hat{\rho}$ describe instead the probability of an atom being in state i and are therefore related to the populations of the various states of the system.

2.3.2 Rotating Wave Approximation

From Equation (2.29) the relative magnitude of nonlinear to linear terms on the R.H.S. is given by

$$\frac{|\mathbf{E}||\boldsymbol{\mu}|}{\hbar\omega_{jk}} \tag{2.30}$$

For optical processes this ratio is very small (typically 10^{-4} to 10^{-7}) so we must ask why we cannot just neglect all but the first terms on the R.H.S. and integrate (2.29) directly. The danger comes if the nonlinear part contains terms which are resonant with ω_{jk} [38]. In that case there are forcing terms which are solutions to the homogeneous problem and the solution for ρ_{jk} is something like

$$\rho_{jk}(t) = \rho_{jk}(0)e^{-i\omega_{jk}t} + A\frac{|\mathbf{E}||\boldsymbol{\mu}|}{\hbar}te^{-i\omega_{jk}t} \tag{2.31}$$

with A some constant. The resonant nonlinear terms have an effect which grows linearly in time so that for times $\sim \hbar/(|\mathbf{E}||\boldsymbol{\mu}|)$ they are $O(1)$. It is for this reason that all terms on the R.H.S. which are resonant, or nearly resonant, with ω_{jk} must be retained while all others may be reasonably discarded. This procedure is known as the rotating wave approximation.

2.3.3 Irreversible Terms

There is one more ingredient required when writing down a set of Bloch equations and that is the inclusion of dissipative (or irreversible) terms [37,38]. These arise from a number of physical processes which we have so far failed to include. First of all there are the phenomena of spontaneous emission and inelastic collisions between atoms, both of which induce transitions between levels. These are associated with a loss of energy and affect all elements of the density matrix. Secondly there are elastic collisions which induce no transitions but which change the phases of the wavefunctions and which therefore only affect the off–diagonal elements of the density matrix. A detailed discussion of these processes is beyond the scope of this thesis; in particular, a proper treatment of spontaneous emission requires us to quantise the electromagnetic field. Here we simply add phenomeno-

logical decay terms to the Bloch equations to account for these processes. Thus, Equation (2.29) is generalised to

$$\partial_t \rho_{jk} = -i\omega_{jk}\rho_{jk} + \frac{i\mathbf{E}}{\hbar} \cdot \sum_{l=1}^{N} \boldsymbol{\mu}_{jl}\rho_{lk} - \frac{i\mathbf{E}}{\hbar} \cdot \sum_{l=1}^{N} \boldsymbol{\mu}_{lk}\rho_{jl} - \sum_{l=1}^{N}\sum_{m=1}^{N} \gamma_{jklm}\rho_{lm}. \quad (2.32)$$

2.3.4 Two Level Bloch Equations

Now that we have discussed Bloch equations in some generality we derive such equations for the specific case of a system with only two levels. We first of all assume that the electric field, **E**, is plane–polarised in the x–direction and write it as

$$\mathbf{E} = (Fe^{-i\omega t} + F^* e^{i\omega t})\hat{\mathbf{x}}. \quad (2.33)$$

For the purpose of calculating the driving terms in the Bloch equations factors of $e^{\pm ikz}$ have been omitted since, as already stated in Section 2.3.1, for optical frequencies and atomic scales $kz \ll 1$. We assume that the field induces electric dipole moments in the atoms parallel to the field polarisation so that we can write the macroscopic polarisation as

$$\mathbf{P} = (Pe^{ikz-i\omega t} + P^* e^{-ikz+i\omega t})\hat{\mathbf{x}} \quad (2.34)$$

and the non–zero dipole matrix elements as

$$\boldsymbol{\mu}_{12} = \boldsymbol{\mu}_{21}^* = \mu\hat{\mathbf{x}}. \quad (2.35)$$

μ is assumed to be real without loss of generality.

From Equations (2.27) and (2.34) we can make the identification

$$n_a \mu \rho_{21} = Pe^{ikz-i\omega t}. \quad (2.36)$$

The Bloch equations are obtained by following the procedure outlined in Sections 2.3.1 to 2.3.3.

$$\begin{aligned} \partial_t \rho_{21} &= -(\gamma_\perp + i\omega_{21})\rho_{21} + \frac{iF\mu}{\hbar}(\rho_{11} - \rho_{22})e^{-i\omega t} \\ \partial_t(\rho_{11} - \rho_{22}) &= -\gamma_\parallel(\rho_{11} - \rho_{22} - 1) - \frac{2i\mu}{\hbar}(F\rho_{12}e^{-i\omega t} - F^*\rho_{12}^* e^{i\omega t}). \end{aligned} \quad (2.37)$$

The decay rates of ρ_{21} and $(\rho_{11} - \rho_{22})$ have been written in the standard way as $\gamma_\perp$ and $\gamma_{||}$ respectively. We have assumed that there is no loss of population to other levels $(\rho_{11} + \rho_{22} = 1)$.

Since ρ_{12} is coupled to $(\rho_{11} - \rho_{22})$ we define a new macroscopic variable

$$N = n_a(\rho_{11} - \rho_{22}) \tag{2.38}$$

which represents the population difference between states 1 and 2 (state 2 is assumed to correspond to a higher energy than state 1).

The equations for P and N then read

$$\begin{aligned} \partial_t P &= -\gamma_\perp(1 + i\Delta)P + \frac{i\mu^2}{\hbar}FN \\ \\ \partial_t N &= -\gamma_{||}(N - n_a) + \frac{2i}{\hbar}(F^*P - FP^*) \end{aligned} \tag{2.39}$$

where we have introduced the atomic detuning, Δ

$$\Delta = \frac{(\omega - \omega_{21})}{\gamma_\perp}. \tag{2.40}$$

Equations (2.39) together with Equation (2.20) for the electric field form a closed system: a set of Maxwell–Bloch equations for a two–level medium.

At this point we can try to justify the choice $P = O(\varepsilon^2)$ which we made in Section 2.2 to obtain the field equation. An estimate of the order of magnitude of P is given by the magnitude, P_s, of its steady–state value

$$\begin{aligned} P_s &= \frac{n_a\mu^2}{\hbar\gamma_\perp}F \\ &= 2\varepsilon^2\epsilon_0\alpha l F. \end{aligned} \tag{2.41}$$

where, from Equation (2.12), $\varepsilon^2 = 1/kl$, α is the absorption coefficient of the field on resonance given by

$$\alpha = \frac{n_a\mu^2 k}{2\hbar\gamma_\perp\epsilon_0} \tag{2.42}$$

and l is the longitudinal length scale defined in Section 2.2. When we take the Mean Field Limit of the Maxwell–Bloch equations in the next section we will

require that the loss per pass through a thin medium be small so that αl should also be small and Equation (2.41) will indeed imply that $P = O(\epsilon^2)$.

One last task that we will perform in this section is to rescale the variables F, P and N in order to put the Maxwell–Bloch equations into a form which is used in the literature and which is slightly more convenient. We perform the transformation

$$\mathcal{F} = \frac{\mu}{\hbar(\gamma_\perp \gamma_{||})^{\frac{1}{2}}} F \quad \mathcal{P} = \frac{1}{i n_a \mu} \left(\frac{\gamma_\perp}{\gamma_{||}}\right)^{\frac{1}{2}} P \quad \mathcal{N} = \frac{N}{n_a}.$$

Finally, then, the Maxwell–Bloch equations take the form

$$\begin{aligned} \frac{\partial \mathcal{F}}{\partial z} + \frac{1}{c}\frac{\partial \mathcal{F}}{\partial t} &= \frac{i}{2k}\nabla^2 \mathcal{F} - \alpha \mathcal{P} \\ \frac{\partial \mathcal{P}}{\partial t} &= \gamma_\perp [\mathcal{N}\mathcal{F} - (1 + i\Delta)\mathcal{P}] \\ \frac{\partial \mathcal{N}}{\partial t} &= -\gamma_{||} \left[\mathcal{N} - 1 + \frac{1}{2}(\mathcal{F}\mathcal{P}^* + \mathcal{F}^*\mathcal{P})\right]. \end{aligned} \tag{2.43}$$

2.4 Mean Field Limit

We have now derived a closed set of model equations and at this point we are forced to admit that they are too much for us to handle. Equations (2.43) form a set of nonlinear partial differential equations in three spatial dimensions plus time and such problems, as well as being difficult to treat analytically, are at the limit of what anything other than a supercomputer can integrate in any reasonable time. In this section we are going to place the nonlinear medium in an optical cavity since that is one common technique for providing both feedback and large fields, and we will see that by imposing certain conditions on the system we will be able to remove the z–dependence of the variables [6]. An alternative approach to the one given here, valid for nonlinear Fabry–Perot cavities and employing a pole analysis is given in [39].

The geometry we choose is that of a ring cavity of length $\mathcal{L}$ with flat mirrors

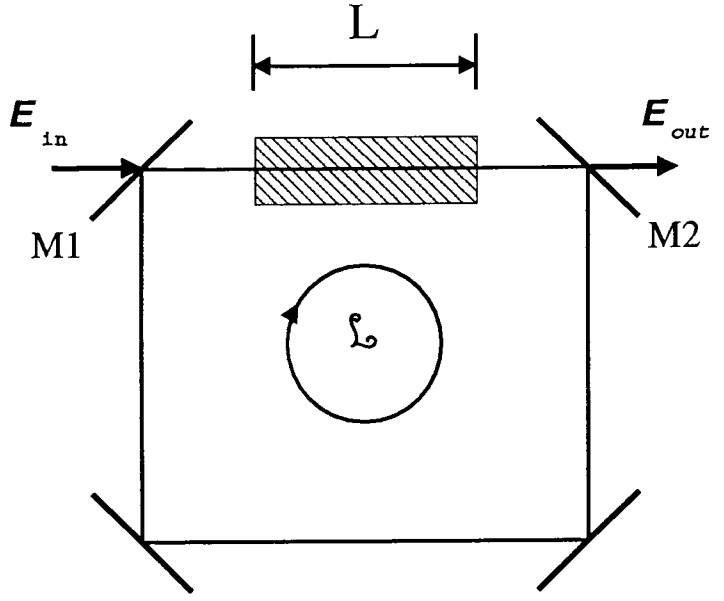

Figure 2.1: *Schematic of the ring cavity.*

containing a thin nonlinear medium of length L. The intra–cavity field is denoted by $\mathcal{F}$ and the system is pumped by an external field E_I (Figure 2.1). We will assume that the medium is thin enough that diffraction can be neglected within it. Then inside the medium the field equation takes the form

$$\frac{\partial \mathcal{F}}{\partial z} + \frac{1}{c}\frac{\partial \mathcal{F}}{\partial t} = -\alpha \mathcal{P}. \tag{2.44}$$

The boundary condition on the electric field at $z = 0$ (the entrance to the nonlinear medium) is

$$\mathcal{F}(x, y, 0, t) = e^{\hat{\mathcal{D}}} \mathcal{F}\left(x, y, L, t - \left(\frac{\mathcal{L} - L}{c}\right)\right) + T E_I(x, y) \tag{2.45}$$

where

$$\hat{\mathcal{D}} = \ln R - i\delta_0 + (\mathcal{L} - L)\frac{i}{2k}\nabla^2 \tag{2.46}$$

is a propagation operator. $R = 1 - T$ is the reflection coefficient of mirrors M1 and M2 and δ_0 is the cavity detuning defined as

$$\delta_0 = \frac{(\omega_c - \omega)\mathcal{L}}{c} \tag{2.47}$$

with ω_c the frequency of the longitudinal cavity mode closest in frequency to ω, the frequency of the input field. $E_I(x, y)$ in Equation (2.45) is the input field at the entrance to the nonlinear medium and need not be a plane wave.

In order to simplify the boundary condition on the field at the entrance and exit of the nonlinear medium we make a transformation of both dependent and independent variables. (z,t) is transformed to (z',t'):

$$\begin{aligned} z' &= z \\ t' &= t + \left(\frac{\mathcal{L}-L}{c}\right)\frac{z}{L} \end{aligned} \tag{2.48}$$

$$\Rightarrow \frac{\partial}{\partial z} + \frac{1}{c}\frac{\partial}{\partial t} = \frac{\partial}{\partial z'} + \frac{\mathcal{L}}{cL}\frac{\partial}{\partial t'}. \tag{2.49}$$

We also define a new field variable, $\tilde{F}(x,y,z',t')$

$$\tilde{F}(x,y,z',t') = \hat{\Gamma}\mathcal{F}(x,y,z',t') + TE_I(x,y)\frac{z'}{L} \tag{2.50}$$

where

$$\hat{\Gamma} = \exp\left(\frac{z'}{L}\hat{\mathcal{D}}\right). \tag{2.51}$$

Then the boundary condition on the field becomes

$$\tilde{F}(x,y,0,t') = \tilde{F}(x,y,L,t') \tag{2.52}$$

that is, the boundary condition is specified in terms of fields at the same time and is periodic in z'. By rendering the longitudinal boundary condition in this form by means of transformation (2.50) we have transferred the information on the free–space propagation which was previously contained in the boundary condition into the field equation, which now reads

$$\begin{aligned} \frac{\partial\tilde{F}}{\partial t'} + \frac{cL}{\mathcal{L}}\frac{\partial\tilde{F}}{\partial z'} &= \frac{cL}{\mathcal{L}}\left[\left(\ln R - i\delta_0 + \frac{i(\mathcal{L}-L)}{2k}\nabla^2\right)\frac{\hat{\Gamma}^{-1}}{L}\left(\tilde{F} - TE_I\frac{z'}{L}\right)\right. \\ &\quad \left. + \hat{\Gamma}\frac{\partial\mathcal{F}}{\partial z'}\right] + \hat{\Gamma}\frac{\partial\mathcal{F}}{\partial t'} + \frac{cTE_I}{\mathcal{L}} \\ &= \frac{cL}{\mathcal{L}}\left[\left(\ln R - i\delta_0 + \frac{i(\mathcal{L}-L)}{2k}\nabla^2\right)\frac{\hat{\Gamma}^{-1}}{L}\left(\tilde{F} - TE_I\frac{z'}{L}\right)\right] \\ &\quad + \frac{cTE_I}{\mathcal{L}} - \frac{c\alpha L}{\mathcal{L}}\hat{\Gamma}\mathcal{P}. \end{aligned} \tag{2.53}$$

We can see that while we may have simplified the boundary condition it appears to have been at the cost of complicating the field equation. At this point, however, we introduce some assumptions about the cavity which allow us to simplify Equation (2.53) and show that this exercise has some benefits.

We assume

$$\begin{cases} T \ll 1 \\ \delta_0 \simeq O(T) \ll 1 \\ \alpha L \simeq O(T) \ll 1 \\ C = \alpha L/T \simeq O(1) \\ \theta = \delta_0/T \simeq O(1) \\ a = (\mathcal{L} - L)/2kT \simeq O(1). \end{cases}$$

$T \ll 1$ implies that the cavity has high finesse so that the frequency spacing between longitudinal modes is large compared to their bandwidth. This condition, together with the assumption that $\delta_0 \ll 1$, ensures that the field is only interacting with one longitudinal mode of the cavity. The entire set of conditions is a requirement that any one element of the system only have a small effect on the field on a single pass, although the cumulative effect after many round trips of the cavity will be significant.

Now that we have made these assumptions we are able to simplify the field equation (2.53). We expand the operator $\hat{\Gamma}$ in the equations for the electric field, polarisation and population difference in powers of the smallness parameter T up to the first order at which the coupling between the variables is introduced; this means expanding to $O(T)$ in the field equation and to $O(1)$ in the polarisation and population difference equations. Another way of saying this is that we only keep those terms in each equation which produce coefficients of $O(1)$. We then arrive at the following set of equations

$$\begin{aligned} \frac{\partial \tilde{F}}{\partial t'} + \frac{cL}{\mathcal{L}} \frac{\partial \tilde{F}}{\partial z'} &= \kappa \left[-\tilde{F} - i\theta \tilde{F} + ia\nabla^2 \tilde{F} + E_I - 2C\mathcal{P} \right] \\ \frac{\partial \mathcal{P}}{\partial t'} &= \gamma_\perp [\mathcal{N}\tilde{F} - (1 + i\Delta)\mathcal{P}] \\ \frac{\partial \mathcal{N}}{\partial t'} &= -\gamma_\parallel \left[\mathcal{N} - 1 + \frac{1}{2} \left(\tilde{F}\mathcal{P}^* + \tilde{F}^*\mathcal{P} \right) \right] \end{aligned} \tag{2.54}$$

where $\kappa = cT/\mathcal{L}$ is the cavity decay rate. We still have an explicit z'–dependence in the equation for the electric field. However, since the longitudinal boundary

condition (2.52) on the electric field is periodic we can expand each of the variables $\tilde{F}$, $\mathcal{P}$ and $\mathcal{N}$ as a Fourier series. Only the coefficients of the zero–frequency term in each of these series will be non–zero since this is the only mode which the input field will interact with under the assumptions that we have made. This means that $\tilde{F}$, and hence $\mathcal{P}$ and $\mathcal{N}$, will be independent of z' and so we can drop the $\partial_{z'}\tilde{F}$ term from the field equation. The Mean Field Maxwell–Bloch equations that we end up with are therefore

$$\begin{aligned}
\frac{\partial \tilde{F}}{\partial t'} &= \kappa\left[-\tilde{F} - i\theta\tilde{F} + ia\nabla^2\tilde{F} + E_I - 2C\mathcal{P}\right] \\
\frac{\partial \mathcal{P}}{\partial t'} &= \gamma_\perp[\mathcal{N}\tilde{F} - (1 + i\Delta)\mathcal{P}] \\
\frac{\partial \mathcal{N}}{\partial t'} &= -\gamma_\parallel\left[\mathcal{N} - 1 + \frac{1}{2}\left(\tilde{F}\mathcal{P}^* + \tilde{F}^*\mathcal{P}\right)\right].
\end{aligned} \tag{2.55}$$

Equations (2.55) are the model equations that we have been aiming to arrive at and they form the basis for the work in Chapters 3 and 5. Before leaving this section, however, it is worth summarising what we have actually done since the procedure we have adopted is quite complicated. By defining a new electric field variable, and also new z and t variables, we have been able to integrate out formally the propagation of the field through the free space part of the cavity. The new field on one side of the nonlinear medium is then simply related to the field on the other side at the same time. In fact, both of these fields are arranged to be equal so that an expansion in a Fourier series in z is possible. The imposition of mean field conditions then ensures that only one term in the Fourier expansion is non–zero and therefore allows the removal of the z–dependence from the equations. Finally we end up with Bloch equations of the same form as when we started and a field equation which has the effects of propagation around the cavity incorporated but which has no dependence on the propagation direction.

2.5 Conclusion

The main aim of this chapter was to derive a manageable set of equations to model the interaction of the electric field with a set of two–level atoms. Starting from Maxwell's Equations and the Schrödinger Equation we were able to derive a closed set of equations describing the evolution of the optical field, the polarisation of the medium and the difference in population between the two levels of the medium. We then placed the medium in a cavity which we assumed to satisfy mean field conditions, and were able to eliminate the propagation direction from the problem. We arrived finally at a set of coupled nonlinear partial differential equations in two spatial dimensions plus time.

The important assumptions made in deriving these equations have been pointed out as they have been introduced in order to make clear the situations under which the equations may be expected to fail, as well as to justify their use in the chapters which follow.

Chapter 3

Two–Level Medium in a Ring Cavity

3.1 Introduction

In the previous chapter we derived equations for a two–level medium in a ring cavity under mean–field conditions and now we go on to examine the pattern–forming behaviour exhibited by such a system. The experimental motivation for this work lies mainly with atomic vapours since, for example, studies of bistability in sodium vapour in the eighties used this model [2], albeit with the deliberate suppression of transverse effects by the use of narrow gaussian beams. More recently, a cavity experiment involving sodium vapour [13] has shown pattern formation in the transverse plane although our model is not directly relevant to that system.

We choose to analyse the equations in the good cavity limit, where the atomic variables can be adiabatically eliminated and the system reduces to a single equation for the intra–cavity field. Unlike in the case of the laser equations [40], the adiabatic elimination procedure in the passive case introduces no spurious instabilities and in fact the stability analysis of the reduced equation gives exactly

the same threshold curves for steady–state bifurcations as does the full set of Maxwell–Bloch equations [6].

We first of all review the linear stability analysis of the model equation for the case where the pump field is a plane–wave, an analysis first performed in [6]. Since this reveals the purely absorptive case ($\Delta = 0$) to be the easiest to work with we concentrate on that initially. A weakly nonlinear analysis close to threshold allows the reduction of the problem to the study of a single partial differential equation in one real variable and predictions about the patterns expected are then made on the basis of amplitude equations. We then tackle the problem for arbitrary Δ, generalising the approach adopted for $\Delta = 0$. We find, in particular, that there is no qualitative change in the predicted behaviour of the system when Δ becomes non–zero, so that the interesting pattern–forming behaviour is captured in the purely absorptive limit.

Finally, numerical integration of the original P.D.E. confirms many of the predictions made on the basis of the nonlinear analysis, showing the power, as well as the limitations, of the amplitude equation approach.

3.2 Model Equation

We start from the mean–field Maxwell–Bloch equations derived in the previous chapter which describe the evolution of the electric field, E, polarisation, P, and population difference, N, for a two–level medium in a high–finesse ring cavity driven by an external pump field, E_I (Figure 3.1)

$$\begin{aligned}
\frac{\partial E}{\partial t} &= \kappa\left[-E - i\theta E + ia\nabla^2 E + E_I - 2CP\right] \\
\frac{\partial P}{\partial t} &= \gamma_\perp[NE - (1 + i\Delta)P] \\
\frac{\partial N}{\partial t} &= -\gamma_\parallel\left[N - 1 + \frac{1}{2}(EP^* + E^*P)\right]
\end{aligned} \tag{3.1}$$

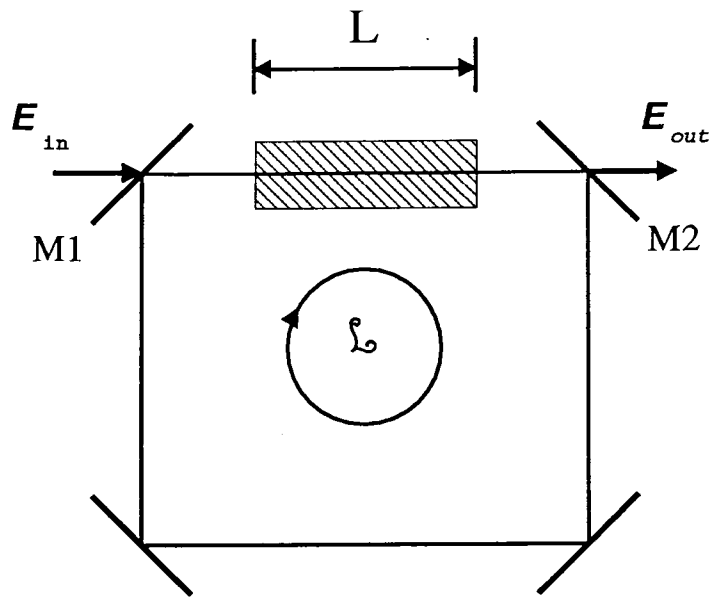

Figure 3.1: *Schematic of the ring cavity.*

with an obvious change of symbols with respect to Equations (2.55).

In the good cavity limit, when $\gamma_\perp$, $\gamma_\parallel \gg \kappa$, the electric field evolves on a much slower time scale than the atomic variables. If the separation of time scales is large enough, the electric field will be effectively constant throughout the period that the atomic variables are evolving towards equilibrium values. Looked at from the other end, on the time scale on which the field is evolving, the polarisation and population difference relax almost instantaneously to values determined by the value of the field at that time: that is, they follow the field adiabatically. In that case, we can set the time derivatives of P and N to zero and solve for them as algebraic functions of the field, E, a process known as adiabatic elimination [41]. It is then possible to reduce the problem to a single nonlinear P.D.E. for the field.

If we carry out this procedure we find that the values of P and N in terms of the field are given by

$$\begin{aligned} P &= \frac{E(1-i\Delta)}{|E|^2+1+\Delta^2} \\ N &= \frac{1+\Delta^2}{|E|^2+1+\Delta^2} \end{aligned} \tag{3.2}$$

so that the equation for the electric field reads

$$\partial_t E = -E\left[(1+i\theta) + \frac{2C(1-i\Delta)}{|E|^2+1+\Delta^2}\right] + E_I + ia\nabla^2 E \tag{3.3}$$

where the time has been scaled by the cavity decay time $1/\kappa$. This is the model equation which we will study.

3.3 Linear Stability Analysis

Equation (3.3) has stationary, homogeneous solutions, E_s, whose moduli are given by solutions of

$$E_I^2 = |E_s|^2\left[\left(1+\frac{2C}{|E_s|^2+1+\Delta^2}\right)^2 + \left(\theta - \frac{2C\Delta}{|E_s|^2+1+\Delta^2}\right)^2\right] \tag{3.4}$$

and whose phases are then obtainable through the expression

$$E_s = \frac{E_I}{(1+i\theta)+\frac{2C(1-i\Delta)}{|E|^2+1+\Delta^2}}. \tag{3.5}$$

Since we are interested in solutions with some kind of spatial structure we want to find out when the system is not attracted to the solution given by (3.4). A sufficient condition for this to be true is that the solution E_s be linearly unstable: that is, a small perturbation to E_s will grow in time. We therefore perturb E_s

$$E = E_s + \delta E \tag{3.6}$$

and examine the solutions to the resulting linear problem in δE and δE^*

$$\partial_t \begin{bmatrix} \delta E \\ \delta E^* \end{bmatrix} = \mathcal{L}(\nabla^2)\begin{bmatrix} \delta E \\ \delta E^* \end{bmatrix} \tag{3.7}$$

where

$$\mathcal{L}(\nabla^2) = \left[\begin{array}{c|c} -(1+i\theta) + \frac{2C(1-i\Delta)|E_s|^2}{(|E_s|^2+1+\Delta^2)^2} & \frac{2C(1-i\Delta)E_s^2}{(|E_s|^2+1+\Delta^2)^2} \\ -\frac{2C(1-i\Delta)}{|E_s|^2+1+\Delta^2} + ai\nabla^2 & \\ \hline \frac{2C(1+i\Delta)E_s^{*2}}{(|E_s|^2+1+\Delta^2)^2} & -(1-i\theta) + \frac{2C(1+i\Delta)|E_s|^2}{(|E_s|^2+1+\Delta^2)^2} \\ & -\frac{2C(1+i\Delta)}{|E_s|^2+1+\Delta^2} - ai\nabla^2 \end{array}\right]. \tag{3.8}$$

Since this is a linear problem we can take the Fourier Transform in which case $\nabla^2 \rightarrow -K^2$. Then

$$\partial_t \begin{bmatrix} \delta\tilde{E} \\ \delta\tilde{E}^* \end{bmatrix} = \mathcal{L}(-K^2) \begin{bmatrix} \delta\tilde{E} \\ \delta\tilde{E}^* \end{bmatrix} \tag{3.9}$$

where a tilde denotes the Fourier Transform. The general solution to such a problem is given by a linear combination of terms $\exp(\lambda_i t)$ where the $\{\lambda_i\}$ are the eigenvalues of the matrix $\mathcal{L}(-K^2)$. The real part of any of the eigenvalues being greater than zero implies exponential growth of the perturbation and therefore linear instability of E_s. If we denote by λ_u the eigenvalue with largest real part, then the locus of points in the parameter space defined by the condition $Re(\lambda_u) = 0$ constitutes a threshold surface (or stability surface) separating the region in which E_s is stable from the region in which it is unstable (Figure 3.2).

The two eigenvalues of $\mathcal{L}$ are given by

$$\lambda_\pm = -1 - \frac{2C(1+\Delta^2)}{(|E_s|^2+1+\Delta^2)^2} \pm \sqrt{\frac{4|E_s|^4C^2(1+\Delta^2)}{(|E_s|^2+1+\Delta^2)^4} - \left[\frac{2C\Delta(1+\Delta^2)}{(|E_s|^2+1+\Delta^2)^2} - (\theta + aK^2)\right]^2}. \tag{3.10}$$

It is obvious from (3.10) that for $Re(\lambda) > 0$, λ must be real so that the possibility of a Hopf bifurcation (λ pure imaginary) is excluded and only "steady–state" bifurcations are possible. The threshold condition ($Re(\lambda_+) = 0$) then implies the

following relation

$$\begin{aligned} 4C^2(1+\Delta^2)[I^2-(1+\Delta^2)] &+ 4C(1+\Delta^2)[\Delta\Theta-1][1+\Delta^2+I] \\ &- [1+\Theta^2][1+\Delta^2+I]^3 = 0 \end{aligned} \tag{3.11}$$

where

$$I = |E_s|^2, \quad \Theta = \theta + aK^2. \tag{3.12}$$

We can obtain the relationship between the values of $(\theta+aK^2)$ and I at the lowest threshold ($(\theta+aK_c^2)$ and I_c respectively) by differentiating Equation (3.11) with respect to $(\theta+aK^2)$ and setting $d(|E_s|^2)/d(\theta+aK^2)$ to zero [†]. This gives

$$(\theta+aK_c^2) = \frac{2C\Delta(1+\Delta^2)}{(1+\Delta^2+I_c)^2}. \tag{3.13}$$

K_c is then the magnitude of the most unstable wavevector and defines the length scale of the pattern which will emerge above threshold.

Using Equations (3.10) and (3.13) we find, in fact, that I_c is given by the smaller of the two roots of the following quadratic in the dummy variable z

$$2zC(1+\Delta^2)^{\frac{1}{2}} - (1+\Delta^2+z)^2 - 2C(1+\Delta^2) = 0 \tag{3.14}$$

that is,

$$I_c = C(1+\Delta^2)^{\frac{1}{2}} - (1+\Delta^2) - \sqrt{C(1+\Delta^2)(C-2) - 2C(1+\Delta^2)^{\frac{3}{2}}}. \tag{3.15}$$

Since the source of the nonlinearity in Equation (3.3) saturates as $|E|^2$ increases, then if the driving field becomes large enough the homogeneous solution E_s will become stable once more. This means that the instability region in the (I,Θ)–plane should be bounded by a closed curve (such curves are in fact cross–sections through the full stability surface defined in (I,Θ,C)–space). The other root of (3.14) therefore defines the value of I which corresponds to the other extremum of that curve (Figure 3.3). For both of these two roots to be real (that is, for an instability region to exist at all), Equation (3.15) shows that C must satisfy

$$C \geq 2[1+(1+\Delta^2)^{\frac{1}{2}}] = C_{crit}. \tag{3.16}$$

[†]By lowest threshold we mean the lowest value of I for which the stability surface is crossed for a given value of C.

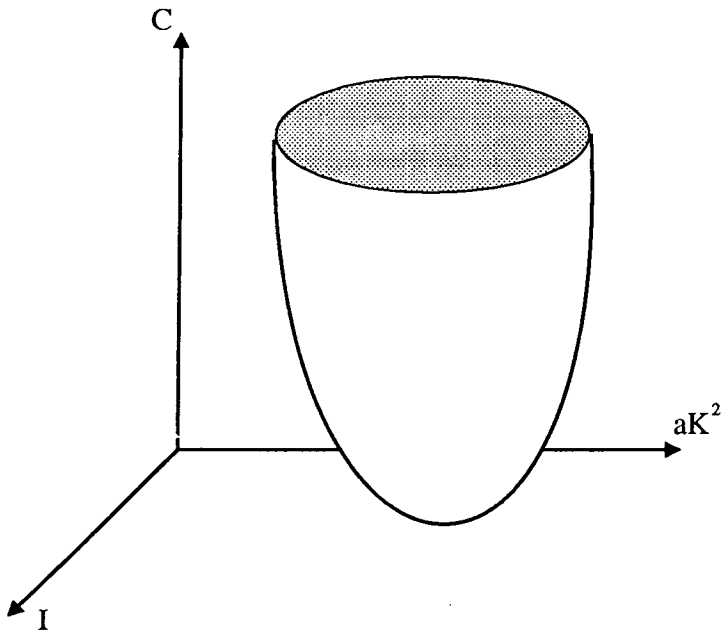

Figure 3.2: *Representation of the stability surface in* (I, aK^2, C)*-space.*

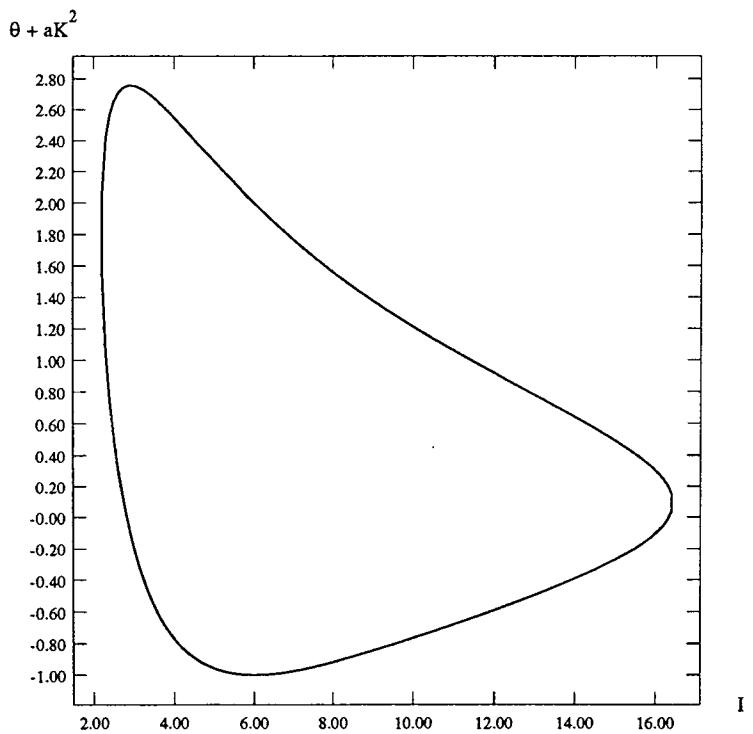

Figure 3.3: *Section through the stability surface for* $\Delta = 1$ *in the plane* $C = 8$.

This means that as well as a threshold value which the modulus of the field must exceed for each value of C there is a value of C below which no instability can occur no matter how hard the system is driven. The reason for this is that, since C represents the strength of the coupling between the nonlinear medium and the field, if this coupling is too weak then the field saturates the nonlinearity before it can become strong enough to drive an instability.

Notice that the linear analysis only provides a condition on the magnitude, K, of the wavevector of the perturbation. This is due to the fact that transverse effects only enter the problem through the operator ∇^2 which is invariant under rotations. Notice also that θ and aK^2 only appear in the combination $\theta + aK^2$ so that the only effect of changing θ is to shift the threshold surface parallel to the aK^2 axis if the surface is plotted in (I, aK^2, C)–space. Finally, we remark that the threshold surface can be crossed by varying either I or C or some combination of both. In the subsequent analysis we consider C to be the parameter which is varied (the "control parameter") since the resulting algebra is simpler. In an experiment this would correspond to varying the number density of the atomic sample.

3.4 Weakly Nonlinear Analysis

3.4.1 Amplitude Equations

We know from the linear analysis where the homogeneous solution of Equation (3.3) becomes unstable and also the characteristic length scale of the instability. As mentioned in Section 3.3 the linear analysis only gives a condition on the magnitude of any wavevector that is unstable. This means that above and close to threshold the range of values of K^2 which the linear analysis predicts will go unstable corresponds to an annulus in Fourier space. The fact that the unstable set is restricted to lie within this annulus means that the analysis of the problem, at least close to threshold, can be simplified.

We first of all have to admit that we cannot deal with the problem by analysing functions whose Fourier Transform is non–zero only within an annulus. Instead we inject some assumptions about what we expect to happen in the problem. Pure patterns which emerge as solutions from the bifurcation at the instability threshold can be described as a linear combination of a finite number of modes, each with a different amplitude, and each having a wavevector of magnitude K_c since that is the value of K which first becomes unstable. Thus

$$E - E_s = \frac{1}{2}\left(\sum_{i=1}^{N} A_i e^{i\mathbf{K}_i.\mathbf{x}} + c.c.\right). \tag{3.17}$$

The continuum problem in Fourier space has then been reduced to the consideration of a discrete (and finite) set lying on the circle of radius K_c (the critical circle). The spatio–temporal evolution of the pattern can be described by making the $\{A_i\}$ slowly varying functions of time and space [41]. The spatial dependence of the $\{A_i\}$ is something of an extra, introduced to capture some of the continuum behaviour of the problem, and is usually only useful in the study of defects in patterns. On the other hand, the temporal dependence is indispensible since without it we cannot describe evolution of any kind. We introduce "slow dependence on time" by considering "dependence on slow time"; that is, we introduce slow time scales. This is more than a mathematical gimmick since it will be seen that the introduction of multiple slow time scales is a necessary device in the type of calculation that we are going to undertake. This needs some elucidation so we resort for the moment to a formal treatment of the problem.

We write our original P.D.E. in the form

$$\partial_t \mathbf{V} = \hat{\mathcal{L}}(\nabla^2)\mathbf{V} + N(\mathbf{V}). \tag{3.18}$$

$\mathbf{V}$ contains the dependent variable(s), $\hat{\mathcal{L}}(\nabla^2)$ is a linear operator and N is a nonlinear function. We have assumed without loss of generality that $\mathbf{V} = \mathbf{0}$ is a solution; if it is not, it can be made so by a simple linear transformation of the dependent variables in the starting equation (see for example Equation (3.31) below).

We assume that close to the bifurcation point, the point where the instability surface is crossed and where a new, modulated solution appears, the amplitude

of the modulated solution is small. We then connect this amplitude to the (scaled) distance above threshold, μ, through some smallness parameter ε. We also assume that the bifurcation is steady–state. Expanding $\mathbf{V}$ and μ in powers of ε and introducing slow times $T_1, T_2, ...$ defined such that

$$\partial_t = \varepsilon\partial_{T_1} + \varepsilon^2\partial_{T_2} + ... \tag{3.19}$$

we can write the problem as

$$(\hat{\mathcal{L}}_0(\nabla^2) + \varepsilon\hat{\mathcal{L}}_1(\nabla^2) + \varepsilon^2\hat{\mathcal{L}}_2(\nabla^2) + ...)(\varepsilon\mathbf{V}_1 + \varepsilon^2\mathbf{V}_2 + \varepsilon^3\mathbf{V}_3 + ...)$$

$$= (\varepsilon\partial_{T_1} + \varepsilon^2\partial_{T_2} + ...)(\varepsilon\mathbf{V}_1 + \varepsilon^2\mathbf{V}_2 + \varepsilon^3\mathbf{V}_3 + ...)$$

$$-\varepsilon^2 N_2(\mathbf{V}_1, \mathbf{V}_1) - \varepsilon^3 N_3(\mathbf{V}_1, \mathbf{V}_2) - ... \tag{3.20}$$

The expansion of $\hat{\mathcal{L}}$ results from the fact that it will also depend on μ.

At $O(\varepsilon)$ we recover the problem solved in the linear stability analysis

$$\hat{\mathcal{L}}_0(\nabla^2)\mathbf{V}_1 = 0. \tag{3.21}$$

From this we see that the condition that $\mathbf{V}_1$ be nontrivial is that $\hat{\mathcal{L}}_0$ is singular. We know this is true since $\hat{\mathcal{L}}_0$ has a zero eigenvalue at threshold with $\nabla^2 \to -K_c^2$. Thus we write

$$\mathbf{V}_1 = \frac{1}{2}\mathbf{v}_1\left(\sum_{i=1}^{N} A_i(T_1, T_2, ...)e^{i\mathbf{K}_i\cdot\mathbf{x}} + c.c.\right) \tag{3.22}$$

with $|\mathbf{K}_i| = K_c$ and with the N wavevectors making angles of π/N with each other, since this is sufficient to describe the pure patterns which are usually observed.

At $O(\varepsilon^2)$ we get

$$\hat{\mathcal{L}}_0(\nabla^2)\mathbf{V}_2 = -\hat{\mathcal{L}}_1(\nabla^2)\mathbf{V}_1 + \partial_{T_1}\mathbf{V}_1 - N_2(\mathbf{V}_1, \mathbf{V}_1). \tag{3.23}$$

This is no problem for terms with $K \neq K_c$ since in that case $\hat{\mathcal{L}}_0(\nabla^2)$ is in principle invertible. For terms with $K = K_c$, however, $\hat{\mathcal{L}}_0$ is singular (Equation (3.21)). We therefore have a problem of the form

$$\hat{\mathcal{L}}_0\mathbf{V}_2 = \mathbf{S}_2 \tag{3.24}$$

where $\hat{\mathcal{L}}_0$ cannot be inverted. The only way to resolve this is to invoke the Fredholm Alternative Theorem [41] which states that for (3.24) to have a solution, $\mathbf{S}_2$ must be orthogonal to the null–space of $\hat{\mathcal{L}}_0^\dagger$, the adjoint of $\hat{\mathcal{L}}_0$. This is just equivalent to ensuring that $\mathbf{S}_2$ lies in the range of $\hat{\mathcal{L}}_0$. To see this, note that if $\mathbf{S}_2 = \hat{\mathcal{L}}_0\mathbf{V}_2$ for some $\mathbf{V}_2$ then if $\mathbf{U}$ is in the null–space of $\hat{\mathcal{L}}_0^\dagger$ we have that

$$\begin{aligned} \langle \mathbf{U}|\hat{\mathcal{L}}_0\mathbf{V}_2\rangle &= \langle \hat{\mathcal{L}}_0^\dagger\mathbf{U}|\mathbf{V}_2\rangle \\ &= 0 \end{aligned} \tag{3.25}$$

where $\langle\cdot|\cdot\rangle$ denotes an inner product and we have used the definition of the adjoint. For example, consider the case where $\mathbf{V}_2$ and $\mathbf{S}_2$ are vectors in $\mathcal{R}^3$ and $\hat{\mathcal{L}}_0$ is a 3x3 matrix with a one–dimensional null–space. The Fredholm Alternative theorem is then saying that for (3.24) to be solvable $\mathbf{S}_2$ must lie in the plane perpendicular to the eigenvector of $\hat{\mathcal{L}}_0^\dagger$ corresponding to a zero eigenvalue: that is, in the range of $\hat{\mathcal{L}}_0$.

Returning to the case of interest to us, Equation (3.23) shows that $\mathbf{S}_2$ contains time derivatives of the $\{A_i\}$ with respect to T_1, so that the solvability condition comes out in the form of a set of ordinary differential equations which the $\{A_i\}$ must satisfy. The purpose of the introduction of the slow time scales is thus to allow a sufficient degree of freedom in $\mathbf{S}_2$ for the problem to have a solution.

Calculations at higher orders follow the same pattern as that at $O(\varepsilon^2)$, yielding further equations for the $\{A_i\}$ in the other slow time scales. At the end of the calculation all of these equations are added together and the scalings undone to give a final set of *amplitude equations* for the time–evolution of the amplitudes $\{A_i\}$ in terms of the unscaled time t. It can be seen that this result depends upon the introduction of multiple time scales.

The introduction of spatial dependence in the $\{A_i\}$ has a different motivation. The intention is to allow more of the full spatio–temporal dynamics of the original equations to be captured by the amplitude equations so that such things as defects in patterns may be studied. From Figure 3.4 and the previous discussion we know that above threshold an annulus of wavevectors of width $\delta K = O(\varepsilon)$ is

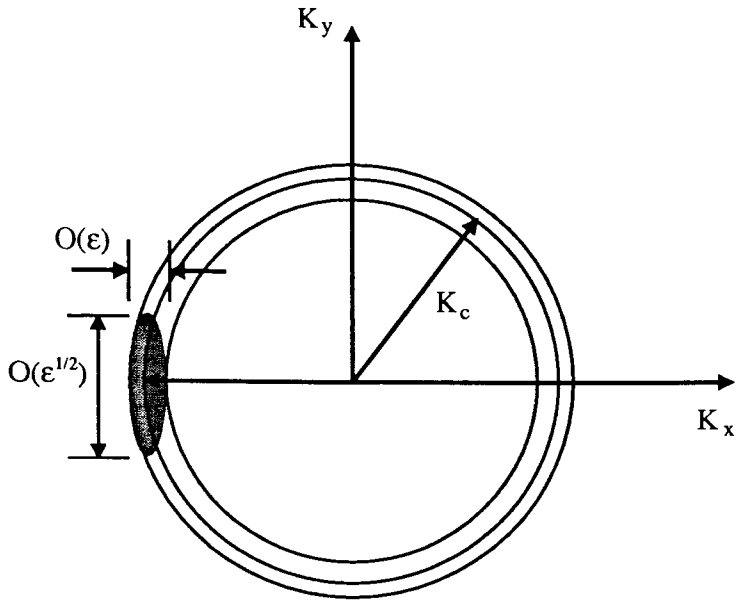

Figure 3.4: *The annulus of unstable wave-vectors. The figure shows that the unstable region around a particular wave-vector on the circle* $|K| = K_c$ *has a width* $O(\varepsilon)$ *parallel to the wave-vector and a length* $O(\varepsilon^{\frac{1}{2}})$ *perpendicular to it.*

excited. Since a small width in Fourier space corresponds to large length scales in real space, the field can be described by allowing the $\{A_i\}$ to be slowly varying functions of x and y. As with the time dependence, this is accomplished by introducing "slow" space variables. We have to be careful, however, in the relative scalings that we employ for x and y [42].

Figure 3.4 shows that if we choose the K_x–direction to lie along one of the wavevectors in the pattern, the set of unstable wavevectors around that mode has different extents in the K_x– and K_y–directions: $O(\varepsilon)$ in K_x and, by a simple geometrical construction, $O(\sqrt{\varepsilon})$ in K_y. We therefore choose slow spatial variables X and Y such that

$$\begin{aligned} \frac{\partial}{\partial x} &= \frac{\partial}{\partial x_0} + \varepsilon \frac{\partial}{\partial X_1} \\ \frac{\partial}{\partial y} &= \sqrt{\varepsilon}\, \frac{\partial}{\partial Y_1}. \end{aligned} \tag{3.26}$$

This also means that the calculation is simplest if we allow a set of different co–ordinate axes, one for each mode of the pattern: (x_i, y_i) is chosen such that K_{xi} is parallel and K_{yi} perpendicular to the wavevector of mode i. Then in each amplitude equation the spatial terms will be of the same form but will refer to

different co–ordinate bases.

It turns out that it is necessary to carry out the multiple scales calculation to at least $O(\varepsilon^3)$ since that is the first order at which the pattern solution may appear as a stable, bounded solution of the amplitude equations. In that case the amplitude equations will take the form

$$\partial_t A_i = \mu A_i + \alpha A_j^* A_k^* - \sum_{l=1}^{N} \gamma_{li} |A_l|^2 A_i + \sigma \left(\frac{\partial}{\partial x_i} - \frac{i}{2K} \frac{\partial^2}{\partial y_i} \right)^2 A_i. \qquad (3.27)$$

Here μ represents a linear growth and is proportional to the distance above threshold. The γ_{li} are coefficients of the cross– and self–cubic nonlinear terms which saturate the linear growth. The strange spatial operator is known as the Newell–Whitehead derivative and is characteristic of amplitude equations derived in systems with rotational invariance [42]. Its form is a result of the different scalings in x and y necessary in such systems. †

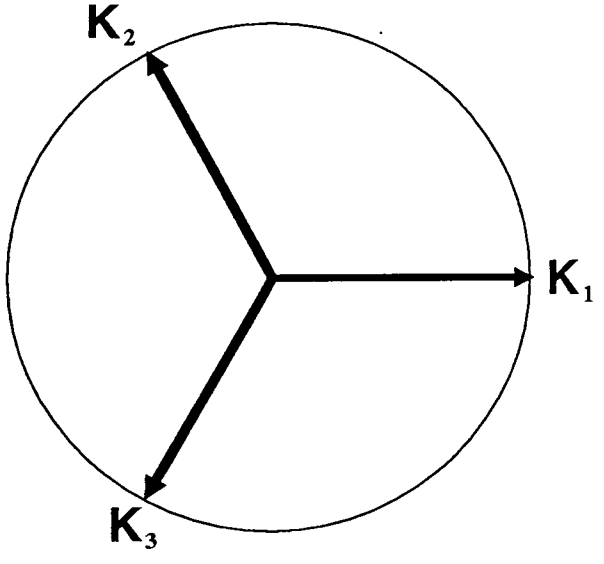

Figure 3.5: *The triad of wavevectors which make up a hexagonal pattern.*

The quadratic coefficient α is non–zero only if $\mathbf{K}_i + \mathbf{K}_j + \mathbf{K}_k = 0$ since only in that case will the wavevectors corresponding to A_j^* and A_k^* have a sum which is resonant

†This may not be the only spatial term in the amplitude equations. When such equations are derived it may turn out that there are terms involving derivatives of nonlinear functions of the amplitudes. We omit them here because they are not generic, nor will such terms appear anywhere in this thesis.

with that corresponding to A_i (Figure 3.5). Such a triad of wavevectors in Fourier space corresponds to a hexagonal pattern in real space. Because they have this mutual reinforcement property which no other pattern possesses, namely that the sum or difference of any two different wavevectors gives another wavevector in the pattern, hexagons are observed close to threshold in systems where the quadratic coefficient α does not vanish identically. For this reason we normally restrict our expansion to the three modes of a hexagonal pattern when quadratic coupling is present. In that case the amplitude equations for the three amplitudes, A, B and C of the active modes take the form

$$\begin{aligned} \partial_t A &= \mu A + \alpha B^* C^* - \zeta |A|^2 A - \gamma(|B|^2 + |C|^2)A \\ &+ \sigma \left(\frac{\partial}{\partial x_A} - \frac{i}{2K} \frac{\partial^2}{\partial y_A} \right)^2 A. \end{aligned} \tag{3.28}$$

Equations for B and C are obtained by cyclic permutation of $[ABC]$ in (3.28). In this form the amplitude equations are known as the Ginzburg–Landau Hexagon (GLH) Equations. They have several different stationary, homogeneous solutions [43]:

1) $A = B = C = 0$: stable for $\mu < 0$; unstable for $\mu > 0$.

2) $A = \sqrt{\mu/\zeta} e^{i\phi}$, $B = C = 0$ (Rolls): stable for $\mu > \alpha^2/(\gamma - \zeta)^2 = \mu_3$; unstable for $\mu < \mu_3$.

3) $A = |A|e^{i\phi_1}$, $B = |B|e^{i\phi_2}$, $C = |C|e^{i\phi_3}$ with $|A| = |B| = |C| = A_0$ where A_0 is given by a root of the equation

$$(\zeta + 2\gamma)A_0^2 - \alpha A_0 - \mu = 0$$

and either

a) $\phi_1 + \phi_2 + \phi_3 = 0$ (H^+ hexagons): stable for $\alpha > 0$ and $\mu_1 = -\alpha^2/(4(\zeta + 2\gamma)) < \mu < \mu_4 = \alpha^2(\gamma + 2\zeta)/(\gamma - \zeta)^2$

or

b) $\phi_1 + \phi_2 + \phi_3 = \pi$ (H^- hexagons or "honeycombs"): stable for $\alpha < 0$ and $\mu_1 = -\alpha^2/(4(\zeta + 2\gamma)) < \mu < \mu_4 = \alpha^2(\gamma + 2\zeta)/(\gamma - \zeta)^2$.

4) $A = Re^{i\phi_1}$, $B = Re^{i\phi_2}$, $C = Ue^{i\phi_3}$ and any circular permutation with $U = \alpha\cos(\phi_1+\phi_2+\phi_3)/(\gamma-\zeta)$, $R^2 = (\mu-\zeta U^2)/(\gamma+\zeta)$ and $\phi_1+\phi_2+\phi_3 = 0$ (π) for $\alpha > 0$ (< 0) (mixed states): these exist only for $\mu > \mu_3$ and are always unstable.

"Rolls" consist of a cosinusoidal modulation of the field and appear as a pattern of stripes. The H^+ hexagons take the form of hexagonally co–ordinated intensity peaks on a background while the H^- are intensity "holes" in the background. The H^+ are stable close to threshold when the quadratic coupling coefficient α is positive and the H^- when α is negative.

We can sketch the form that these solutions take as functions of μ on bifurcation diagrams such as Figure 3.6 which indicates the general behaviour of the co–existent roll and H^+ solutions for positive α in the six–dimensional hexagon phase–space. The amplitude of the hexagon solution is finite at $\mu = 0$ and the solution extends below threshold, disappearing at $\mu = \mu_1$. It exhibits what is known as a *subcritical bifurcation* of *transcritical* type. The hexagon solution remains stable with respect to the roll solution up to $\mu = \mu_4$ after which it becomes unstable. The roll amplitude, on the other hand, emerges continuously from zero at threshold via a *supercritical bifurcation.* Rolls are unstable with respect to hexagons up to $\mu = \mu_3$ after which they become stable. All of this behaviour is revealed through a simple linear stability analysis of the different solutions of the normal form equations represented by (3.28).

Implicit in the previous statements on the existence and stability of the different kinds of solutions is the assumption that the cubic coefficients are positive. If ζ is found to be negative then a single mode (roll) solution cannot be found because the amplitude equation for a single mode has no stable, bounded solutions. In that case the perturbation calculation would have to be carried out to the lowest order which produces nonlinear terms of the correct sign to saturate the linear

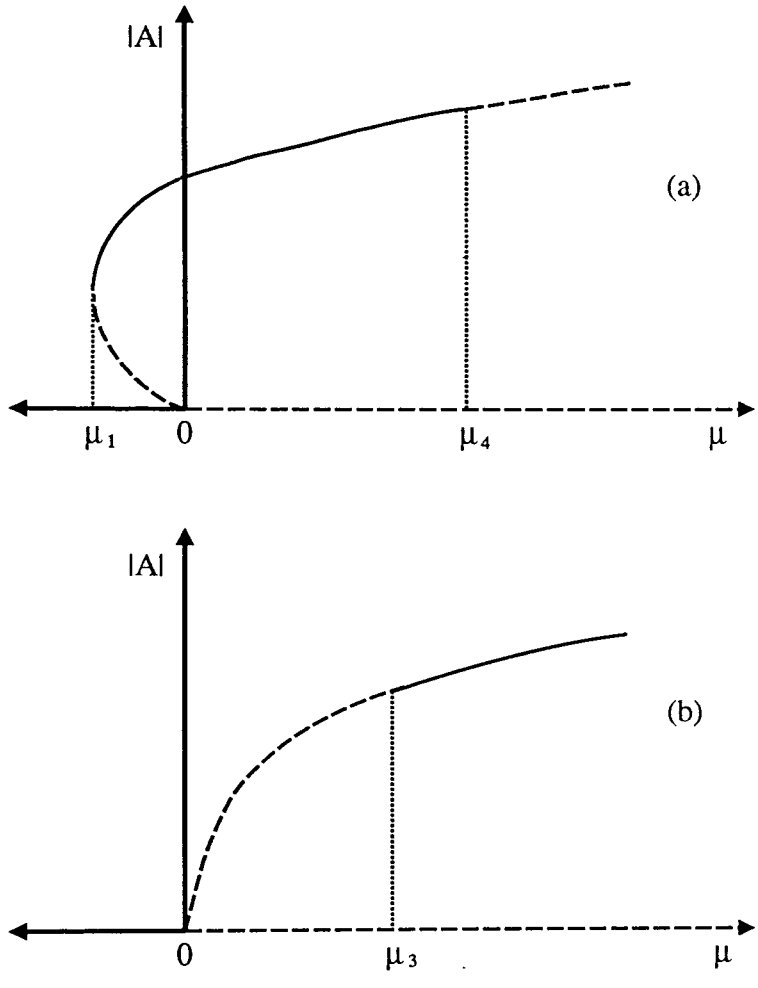

Figure 3.6: *The form and relative stability of solutions in the full six–dimensional hexagon phase–space. The figure shows the amplitudes of (a) hexagons and (b) supercritical rolls as functions of the linear growth rate μ. The dashed lines represent unstable solutions while the solid lines denote stable solutions. The linear instability threshold corresponds to $\mu = 0$. The unstable mixed states are not represented.*

growth. For rolls this means proceeding to at least fifth order in which case the roll amplitude is obtained as a stationary solution of an equation of the form

$$\partial_t A = \mu A - \zeta |A|^2 A - \kappa |A|^4 A. \tag{3.29}$$

Then the bifurcation to the roll solution becomes *subcritical* (Figure 3.7) and,as in the hexagon case, there is a region below threshold ($-\zeta^2/(4\kappa) \leq \mu < 0$) where a stable roll solution exists. We note that it is not usual to carry out the perturbation calculation to fifth order but that a change of sign of ζ is sufficient to indicate the transition from a supercritical to a subcritical bifurcation.

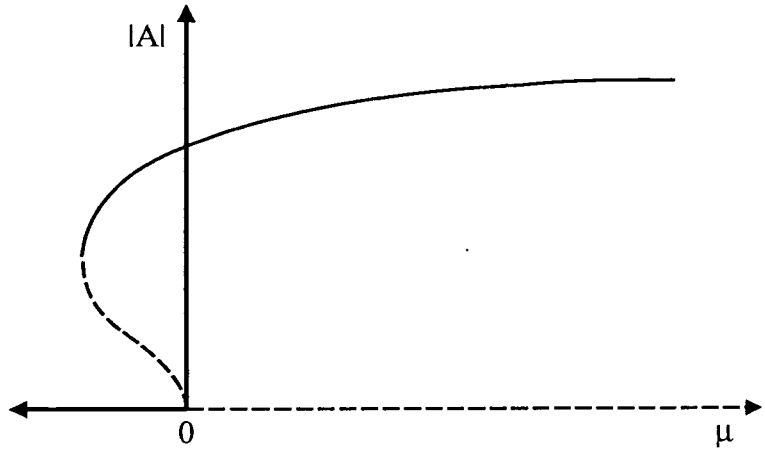

Figure 3.7: *The form of the solution as a function of the linear growth rate μ for subcritical rolls. The dashed lines represents an unstable solution. The solution branch represented by the solid line is stable in one dimension but part of it may be unstable to hexagons in two dimensions.*

Similarly, when $2\gamma + \zeta < 0$ the hexagon solutions cannot be found from the amplitude equations derived at third order. Unlike for rolls, though, this has no serious implications about the nature of the bifurcation, which is already subcritical, but merely affects the exact shape of the solution curve which, for the case of quintic saturation, becomes quartic rather than parabolic.

There is one final caveat. If the quadratic coefficient α in Equation (3.28) is too large, for example $O(1)$ then, with ζ and γ $O(1)$ too, the hexagon amplitude at threshold will be $O(1)$. This means that the multiple scales calculation, which is based on the assumption that the amplitude of the pattern is $O(\varepsilon)$, will be invalid and the amplitude equations will be meaningless. We still expect that hexagons

will be the stable pattern close to threshold, but we cannot make quantitative predictions about the location of the hexagon solution branch or its stability. On the other hand, if α is $O(\varepsilon^2)$ then with $|B|$ and $|C|$ both of $O(\varepsilon)$ the quadratic term in Equation (3.28) is properly of higher order. This means that the amplitude equations derived at $O(\varepsilon^3)$, which are expected to describe the behaviour close to threshold, will strictly contain no quadratic coupling term. Thus if α vanishes identically for some parameter values we may expect that for nearby parameter values, where α is small but not zero, we will still not see hexagons.

All of this is a bit abstract and will become clearer when the procedure is applied to specific problems in the sections which follow in this chapter, as well as in the next chapter.

3.4.2 The $\Delta = 0$ Case

We analyse this case first since it illustrates the techniques adopted later for the more general case and because for $\Delta = 0$ the instability has a clear physical interpretation.

From Equation (3.13) we see that K_c, the transverse wavevector which first becomes unstable on crossing the stability surface, is defined by

$$\theta + aK_c^2 = 0. \tag{3.30}$$

This means that the system generates an instability with a transverse wavevector which exactly cancels the effect of the cavity detuning. The field travelling off–axis has a larger resultant wavevector than a field propagating on–axis and hence oscillates at a larger frequency $\omega_c = c(k^2 + K_c^2)^{\frac{1}{2}}$. By choosing the correct transverse wavevector the system can make this new frequency equal to that of the input field and this, according to Equation (3.30), is what is happening. By this interpretation we therefore only get a pattern–forming instability for negative θ since for positive θ the cavity frequency is already larger than the frequency of the pump field and the difference between the two can only be increased by off–axis propagation. This mechanism whereby the off–axis emission compensates

for a detuning has also been identified in both lasers [44] and optical parametric oscillators [45].

Before beginning our nonlinear analysis we perform a transformation of variables which shifts the time–independent, homogeneous solution E_s to the origin

$$E = E_s(1 + \mathcal{A}). \tag{3.31}$$

In terms of the new variable $\mathcal{A}$ Equation (3.3) becomes

$$\partial_t \mathcal{A} = -(1 + i\theta)\mathcal{A} + ai\nabla^2\mathcal{A} - \frac{2C(1 + \mathcal{A})}{1 + I(1 + \mathcal{A} + \mathcal{A}^* + |\mathcal{A}|^2)} + \frac{2C}{1 + I}. \tag{3.32}$$

where $I = |E_s|^2$. If we assume $|\mathcal{A}|^2 \ll 1$ (or more accurately, $\mathcal{A} + \mathcal{A}^* + |\mathcal{A}|^2 < (1 + I)/I$) we can re–write this as

$$\partial_t \mathcal{A} = -\left(1 + i(\theta - a\nabla^2) + \frac{2C}{1 + I}\right)\mathcal{A} - \frac{2C}{1 + I}(1 + \mathcal{A})\sum \tag{3.33}$$

where

$$\sum = \sum_{j=1}^{\infty} \left(\frac{-I(\mathcal{A} + \mathcal{A}^* + \mathcal{A}\mathcal{A}^*)}{1 + I}\right)^j. \tag{3.34}$$

We now write $\mathcal{A} = R + iS$, with R and S real, and $\theta = -aK_c^2$ to give

$$\begin{aligned} \partial_t R &= -\left(1 + \frac{2C}{1 + I}\right) R - a(\nabla^2 + K_c^2)S - \frac{2C(1 + R)}{1 + I}\sum \\ \partial_t S &= -\left(1 + \frac{2C}{1 + I}\right) S + a(\nabla^2 + K_c^2)R - \frac{2CS}{1 + I}\sum. \end{aligned} \tag{3.35}$$

The linearised version of (3.35), which determines the dynamics at threshold, reads

$$\begin{aligned} \partial_t R &= -\left[1 + \frac{2C(1 - I)}{(1 + I)^2}\right] R + \left[\theta - a\nabla^2\right] S \\ \partial_t S &= -\left[1 + \frac{2C}{(1 + I)}\right] S + \left[a\nabla^2 - \theta\right] R. \end{aligned} \tag{3.36}$$

From Equation (3.14) C is related to I at threshold through the relation $2C_0 = (1 + I)^2/(I - 1)$, so that the solutions to these equations are given by

$$(\nabla^2 + K_c^2)^2 R = 0, \qquad (\nabla^2 + K_c^2)S = 0 \tag{3.37}$$

and R and S define the marginal ($\lambda = 0$) and stable ($\lambda = -2I/(I-1) < 0$) eigenvectors respectively. Since we are at threshold, where $K = K_c$, Equation (3.37) reduces to

$$(\nabla^2 + K_c^2)R = 0, \qquad S = 0 \tag{3.38}$$

This means that at threshold the behaviour of S is purely relaxational: it goes to zero. Above threshold this will still be approximately true i.e. to lowest order. The real part, R, of the field becomes unstable while S has no growth but simply takes on a form determined by R: S is *slaved* to R and can therefore be adiabatically eliminated. This involves solving formally for S in terms of R and substituting this solution into the equation for R to obtain a single P.D.E. for the real field R. When we do this, remembering to keep only terms which will contribute up to third order in R since our perturbation analysis will proceed no further than this, we get for S

$$S \simeq \frac{(1+I)^2}{[(1+I)^2 + 2C(1+I)]}\left[1 + \frac{4CIR}{[(1+I)^2 + 2C(1+I)]}\right] a(\nabla^2 + K_c^2)R \tag{3.39}$$

and so our approximate equation for R reads

$$\begin{aligned}
\partial_t R &= \left(\frac{2C(I-1)}{(1+I)^2} - 1\right) R - \frac{(1+I)a^2(\nabla^2 + K_c^2)^2}{1+I+2C} R \\
&\quad - \frac{a^2 4CI}{(1+I+2C)^2}(\nabla^2 + K_c^2)\left[R(\nabla^2 + K_c^2)R\right] \\
&\quad - \frac{2CI(I-3)}{(1+I)^3}R^2 + \frac{2CI((1+I)^2 - 8I)}{(1+I)^4}R^3 + O(R^4).
\end{aligned} \tag{3.40}$$

Now, applying the technique discussed in Section 3.4.1, we write

$$\begin{aligned}
R &= \varepsilon R_1 + \varepsilon^2 R_2 + \varepsilon^3 R_3 + \ldots \\
\partial_t &= \varepsilon \partial_{T_1} + \varepsilon^2 \partial_{T_2} + \ldots \\
\frac{\partial}{\partial x_i} &= \frac{\partial}{\partial x_{i0}} + \varepsilon \frac{\partial}{\partial X_{i1}} \\
\frac{\partial}{\partial y_i} &= \sqrt{\varepsilon}\, \frac{\partial}{\partial Y_{i1}} \\
C &= C_0 + \mu_1 \varepsilon + \mu_2 \varepsilon^2 + \ldots
\end{aligned} \tag{3.41}$$

At $O(\varepsilon)$ we just recover the results of the linear analysis:

$$0 = -\left[1 + \frac{2C_0(1-I)}{(1+I)^2}\right] R_1 - \frac{a^2(I-1)(\nabla_0^2 + K_c^2)^2}{2I} R_1 \tag{3.42}$$

which has solutions given by

$$2C_0 = \frac{(1+I)^2}{I-1}, \qquad (\nabla_0^2 + K_c^2) R_1 = 0. \tag{3.43}$$

Bearing in mind that with quadratic coupling present we expect hexagons we write

$$R_1 = \frac{1}{2}\left(A \exp(\mathbf{K_1}.\mathbf{r}) + B \exp(\mathbf{K_2}.\mathbf{r}) + D \exp(\mathbf{K_3}.\mathbf{r}) + c.c.\right) \tag{3.44}$$

where $|\mathbf{K_1}| = |\mathbf{K_2}| = |\mathbf{K_3}| = K_c$ and $\mathbf{K_1} + \mathbf{K_2} + \mathbf{K_3} = 0$–a hexagon.

At $O(\varepsilon^2)$ we get

$$\partial_{T_1} R_1 = \frac{2\mu_1(I-1)}{(1+I)^2} R_1 - \frac{(I-1)a^2}{2I}(\nabla_0^2 + K_c^2)^2 R_2 - \frac{I(I-3)}{(I^2-1)} R_1^2. \tag{3.45}$$

For the resonant terms (those with $K = K_c$) this gives

$$\begin{aligned}
\partial_{T_1} A &= \frac{2\mu_1(I-1)}{(1+I)^2} A - \frac{I(I-3)}{(I^2-1)} B^* D^* \\
\partial_{T_1} B &= \frac{2\mu_1(I-1)}{(1+I)^2} B - \frac{I(I-3)}{(I^2-1)} A^* D^* \\
\partial_{T_1} D &= \frac{2\mu_1(I-1)}{(1+I)^2} D - \frac{I(I-3)}{(I^2-1)} A^* B^*.
\end{aligned} \tag{3.46}$$

Writing R_2 as

$$\begin{aligned}
R_2 = R_{20} + \frac{1}{2}\,&(R_{24} \exp(\mathbf{K_1} - \mathbf{K_2}).\mathbf{r} + R_{25} \exp(\mathbf{K_1} - \mathbf{K_3}).\mathbf{r} \\
&+ R_{26} \exp(\mathbf{K_2} - \mathbf{K_3}).\mathbf{r} + R_{27} \exp(2\mathbf{K_1}).\mathbf{r} + R_{28} \exp(2\mathbf{K_2}).\mathbf{r} \\
&+ R_{29} \exp(2\mathbf{K_3}).\mathbf{r} + c.c.)
\end{aligned} \tag{3.47}$$

and defining

$$\xi = \frac{I^2(I-3)}{(I-1)(I^2-1)a^2 K_c^4} \tag{3.48}$$

we get

$$\begin{aligned}
R_{20} &= -\xi\left(|A|^2+|B|^2+|D|^2\right)\\
R_{24} &= -\xi\frac{AB^*}{2}\\
R_{25} &= -\xi\frac{AD^*}{2}\\
R_{26} &= -\xi\frac{BD^*}{2}\\
R_{27} &= -\xi\frac{A^2}{9}\\
R_{28} &= -\xi\frac{B^2}{9}\\
R_{29} &= -\xi\frac{D^2}{9}.
\end{aligned} \tag{3.49}$$

At $O(\varepsilon^3)$ we have

$$\begin{aligned}
\partial_{T_1}R_2+\partial_{T_2}R_1 &= \frac{2\mu_2(I-1)}{(1+I)^2}R_1+\frac{2\mu_1(I-1)}{(1+I)^2}R_2\\
&-\frac{(I-1)a^2}{2I}\left[\left(2\frac{\partial}{\partial x_{i0}}\frac{\partial}{\partial X_{i1}}+\frac{\partial^2}{\partial Y_{i1}}\right)^2 R_1\right.\\
&+2(\nabla_0^2+K_c^2)\left(2\frac{\partial}{\partial x_{i0}}\frac{\partial}{\partial_{Xi1}}+\frac{\partial^2}{\partial Y_{i1}}\right)R_2\\
&\left.+(\nabla_0^2+K_c^2)^2R_3\right]\\
&-\frac{a^2(I-1)}{2I}(\nabla_0^2+K_c^2)\left[R_1(\nabla_0^2+K_c^2)R_2\right]\\
&+\frac{\mu_1(I-1)^2a^2}{2I^2(1+I)}\left[(\nabla_0^2+K_c^2)^2R_2\right]-\frac{2I(I-3)}{(I^2-1)}R_1R_2\\
&-\frac{2\mu_1I(I-3)}{(1+I)^3}R_1^2+\frac{I((1+I)^2-8I)}{(I-1)(1+I)^2}R_1^3.
\end{aligned} \tag{3.50}$$

Looking at only the resonant terms, for example, those with K-vector $\mathbf{K_1}$, we get the solvability condition obeyed by A at third order:

$$\partial_{T_2}A = \frac{2\mu_2(I-1)}{(1+I)^2}A+\frac{2a^2K_c^2(I-1)}{I}\left(\frac{\partial}{\partial X_{A1}}-\frac{i}{2K_c}\frac{\partial^2}{\partial Y_{A1}}\right)^2 A$$

$$+\frac{2I^3(I-3)^2}{(I-1)(I^2-1)^2a^2K^4}\left(\frac{19|A|^2}{18}+\frac{5|B|^2}{4}+\frac{5|D|^2}{4}\right)A$$

$$+\frac{I((1+I)^2-8I)}{(I-1)(1+I)^2}\left(\frac{3|A|^2}{4}+\frac{3|B|^2}{2}+\frac{3|D|^2}{2}\right)A$$

$$-\frac{2\mu_1 I(I-3)}{(1+I)^3}B^*D^*. \tag{3.51}$$

Now we can add together Equations (3.46) and (3.51) and unscale the variables according to (3.41). Using Equation (3.46) to get an expression for μ_1 in terms of the steady–state amplitude and defining

$$\begin{aligned} A &\to \varepsilon A \\ B &\to \varepsilon B \\ D &\to \varepsilon D \end{aligned} \tag{3.52}$$

we can finally write the amplitude equations up to third order:

$$\begin{aligned} \partial_t A &= \frac{2(I-1)}{(1+I)^2}(C-C_0)A+\frac{4a^2K_c^2(I-1)}{2I}\left(\frac{\partial}{\partial x_A}-\frac{i}{2K_c}\frac{\partial^2}{\partial y_A}\right)^2 A \\ &\quad -\frac{I(I-3)}{(I^2-1)}B^*D^*-\frac{I^2(I-3)^2A_0}{(I^2-1)^2}B^*D^* \\ &\quad +\frac{2I^3(I-3)^2}{(I-1)(I^2-1)^2\theta^2}\left(\frac{19|A|^2}{18}+\frac{5|B|^2}{4}+\frac{5|D|^2}{4}\right)A \\ &\quad +\frac{I((1+I)^2-8I)}{(I-1)(1+I)^2}\left(\frac{3|A|^2}{4}+\frac{3|B|^2}{2}+\frac{3|D|^2}{2}\right)A \end{aligned} \tag{3.53}$$

with two other equations for the amplitudes B and D obtained by cyclic permutation of $[ABD]$. A_0 represents the value of the steady–state, homogeneous solution of system (3.53) given by $A = B = D = A_0$.

These equations become more transparent when written in the form of (3.28)

$$\partial_t A = \mu A + \alpha B^*D^* - \zeta|A|^2A - \gamma(|B|^2+|D|^2)A$$

$$+\sigma\left(\frac{\partial}{\partial x_A}-\frac{i}{2K_c}\frac{\partial^2}{\partial y_A}\right)^2 A. \tag{3.54}$$

The explicit forms of the various coefficients are obtained from a comparison between Equations (3.53) and (3.54) while the types and stability of the homogeneous solutions of (3.54) were discussed in Section 3.4.1, to which reference should be made.

Since from Equation (3.53), $sgn(\alpha) = sgn(3-I)$, we expect, roughly, that H^+ will be observed for $I < 3$ and H^- for $I > 3$. This is quite reasonable: the nonlinearity is provided by a saturable term, in this case purely absorptive, and for low values of I the effect of the background field on the nonlinearity is small and the system can form a pattern composed of intensity peaks; whereas if I is larger, the background field has gone some way towards saturating the nonlinearity and in that case it is easier for the system to form a pattern made up of intensity dips. In fact, the situation is slightly more complicated. If we imagine keeping C constant and varying I across the instability region in parameter space, the value of μ will go from zero to some maximum and back to zero again since the threshold surface is closed in the (I, K^2)–plane. In that case we might expect that for some ranges of I, for both $I < 3$ and $I > 3$, the value of μ will be such that it exceeds μ_4, the value above which the hexagon solution becomes unstable to the roll solution. Thus we anticipate a region around $I = 3$ where we observe neither H^+ nor H^- but a roll solution instead.

When $I = 3$ the quadratic coupling vanishes identically and, strictly speaking, we cannot deduce what pattern is likely to be observed from the analysis that we have done at this stage. However, since a roll pattern is expected to be seen on either side of $I = 3$, at least for C large enough, it seems quite likely that rolls will be the stable structure to emerge at $I = 3$ as well. We can actually demonstrate fairly plausibly that this should be the case.

Let us consider the case where the quadratic coefficient vanishes and assume that we have a pattern consisting of N modes. Omitting spatial terms, our set of

amplitude equations takes the form

$$\partial_t A_i = \mu A_i - \sum_{\substack{j=1 \\ j\neq i}}^{N} \gamma_{ij}|A_j|^2 A_i - \zeta|A_i|^2 A_i. \tag{3.55}$$

If we define

$$\mathcal{G} = -\left[\mu\sum_{i=1}^{N}|A_i|^2 - \frac{1}{2}\sum_{\substack{i=1 \\ i\neq j}}^{N}\sum_{j=1}^{N}\gamma_{ij}|A_i|^2|A_j|^2 - \frac{\zeta}{2}\sum_{i=1}^{N}|A_i|^4\right] \tag{3.56}$$

then we can write the amplitude equations as

$$\frac{\partial A_i}{\partial t} = -\frac{\partial \mathcal{G}}{\partial A_i^*}. \tag{3.57}$$

We then have that

$$\begin{aligned}\frac{\partial \mathcal{G}}{\partial t} &= \sum_{i=1}^{N}\left(\frac{\partial \mathcal{G}}{\partial A_i^*}\frac{\partial A_i^*}{\partial t} + \frac{\partial \mathcal{G}}{\partial A_i}\frac{\partial A_i}{\partial t}\right) \\ &= -2\sum_{i=1}^{N}\left|\frac{\partial A}{\partial t}\right|^2 \leq 0.\end{aligned} \tag{3.58}$$

Since $\mathcal{G}$ is a decreasing function of time except at fixed points of the amplitude equations, where it is stationary, the behaviour of the system can be described as a relaxation of $\mathcal{G}$ towards one of its local minima, corresponding to a stationary fixed point of the original system. A function with this property is known as a Lyapunov function and a system for which such a function exists is called gradient. † We expect that in such a system the dynamics will seek out the fixed point corresponding to the global minimum of $\mathcal{G}$. Although we cannot guarantee this, since the initial condition may lie in the basin of attraction of one of the other fixed points, it is a reasonably good guide to what the system is likely to do.

To determine the exact form of the Lyapunov function $\mathcal{G}$ we must find the form of the coefficients $\gamma_{ij} = \gamma(\vartheta_{ij})$ in Equation (3.56). These coefficients describe the

†When spatial terms are present a Lyapunov functional can be defined as an integral over the spatial domain of a functional density. The partial derivative in Equation (3.57) is then replaced by the variational (or functional) derivative. Again, the inclusion of spatial terms is here an unnecessary complication and so we stick to space–independent amplitudes.

cubic coupling between two modes labelled i and j whose wavevectors make an angle ϑ_{ij}. (We assume chiral symmetry so that $\gamma_{ij} = \gamma_{ji}$.) The exact form of the γ_{ij} can therefore be found from an examination of the two–mode problem: that is, by writing amplitude equations for a two mode pattern where the wavevectors of the two modes are orientated at an arbitrary angle and then extracting $\gamma(\vartheta)$ from the resulting amplitude equations at third order.

When we do this we find

$$\gamma(\vartheta) = -f(I)\left[1 + \frac{1}{(1+2\cos(\vartheta))^2} + \frac{1}{(1-2\cos(\vartheta))^2}\right] - g(I) \tag{3.59}$$

where

$$\begin{aligned} f(I) &= \frac{2I^3(I-3)^2}{a^2K^4(I^2-1)^2(I-1)} \\ g(I) &= \frac{3I\left((1+I)^2-8I\right)}{2(I^2-1)(I+1)}. \end{aligned} \tag{3.60}$$

We see that when $I = 3$, where the quadratic coupling term vanishes, we have the useful result that γ is independent of ϑ. In that case $\mathcal{G}$ can be evaluated explicitly for a pattern consisting of N modes:

$$\mathcal{G}(N) = -\frac{\mu^2 N}{2(\gamma(N-1)+\zeta)}. \tag{3.61}$$

From this expression for $\mathcal{G}$ we have that

$$\mathcal{G}(N+1) - \mathcal{G}(N) = \frac{\mu^2(\gamma-\zeta)}{2(\gamma N+\zeta)(\gamma(N-1)+\zeta)} > 0 \quad \begin{array}{ll} \text{if} & \gamma, \zeta, N > 0 \\ \text{and} & \gamma > \zeta. \end{array} \tag{3.62}$$

Since for $I = 3$ we have that $\gamma = 2\zeta = 9/8$ while $\mathcal{G}(N=0) = 0 > \mathcal{G}(N=1)$ we conclude that $N = 1$ corresponds to the global minimum of $\mathcal{G}$. This analysis leads us to expect that a pattern consisting of a single mode (i.e. a roll) will be observed at (and around) $I = 3$ where the quadratic coupling disappears.

This more or less concludes the nonlinear analysis for the $\Delta = 0$ case. Before going on to generalise to arbitrary values of the detuning in the next section, we point out the utility of Equation (3.40) in indicating the pattern–forming

phenomenology of the original equation (3.3). From (3.40) it is easy to see that the quadratic coupling changes sign on either side of, and vanishes at, $I = 3$. Knowing the implications of this on pattern formation one can predict the H^+ to roll to H^- transition on varying I which we have been led to expect from the amplitude equations. In addition we see that the coefficient of the cubic term can change sign and therefore that we can expect to see both sub– and supercritical rolls in one transverse dimension. This is quite a lot of information. The reason that we go on to derive amplitude equations rather than just sticking with Equation (3.40) is that the amplitude equations should be able to provide more quantitative information on such things as pattern selection and stability, pattern amplitudes and the nature of the pattern–forming bifurcation.

3.4.3 Arbitrary Δ

For general Δ the most unstable wavevector is given by

$$\theta + aK_c^2 = \frac{2C_0(1+\Delta^2)\Delta}{(1+\Delta^2+I)^2}. \tag{3.63}$$

Unlike for the zero detuning case, there is no general interpretation of the instability as compensating for a detuned cavity because the medium contributes a nonlinear dispersion and therefore an intensity dependent phase–shift.

To make things slightly easier we start by rescaling the fields and some of the parameters. We define

$$\begin{aligned}
\tilde{E} &= \frac{E}{(1+\Delta^2)^{\frac{1}{2}}} \\
\tilde{E}_I &= \frac{E_I}{(1+\Delta^2)^{\frac{1}{2}}} \\
\tilde{C} &= \frac{C}{(1+\Delta^2)} \\
\tilde{I} &= \frac{I}{(1+\Delta^2)}.
\end{aligned} \tag{3.64}$$

We also define $z = (1+\Delta^2)^{\frac{1}{2}}$. The field equation (3.3) then becomes

$$\partial_t \tilde{E} = -\tilde{E}\left[(1+i\theta) + \frac{2\tilde{C}(1-i\Delta)}{1+|\tilde{E}|^2}\right] + \tilde{E}_I + ai\nabla^2\tilde{E}. \tag{3.65}$$

The most unstable wavevector K_c is now given by

$$\theta + aK_c^2 = \frac{2\tilde{C}_0\Delta}{(1+\tilde{I})^2} \tag{3.66}$$

and the relationship between $\tilde{C}$ and $\tilde{I}$ on the threshold surface is

$$\frac{2\tilde{C}_0}{(1+\tilde{I})^2} = \frac{1}{(z\tilde{I}-1)}. \tag{3.67}$$

Once more we rewrite (3.65) in terms of the new variable $\mathcal{A}$ where $\tilde{E} = \tilde{E}_s(1+\mathcal{A})$:

$$\partial_t \mathcal{A} = -\left(1 + i(\theta - a\nabla^2) + \frac{2\tilde{C}(1-i\Delta)}{1+\tilde{I}}\right)\mathcal{A} - \frac{2\tilde{C}(1-i\Delta)}{1+\tilde{I}}(1+\mathcal{A})\sum \tag{3.68}$$

where again

$$\sum = \sum_{j=1}^{\infty}\left(\frac{-\tilde{I}(\mathcal{A}+\mathcal{A}^*+\mathcal{A}\mathcal{A}^*)}{1+\tilde{I}}\right)^j. \tag{3.69}$$

In general, however, the linearised version of (3.68) is not diagonalised at threshold when written in terms of the real and imaginary parts of $\mathcal{A}$, R and S respectively. In fact we have at threshold, with $K = K_c$,

$$\partial_t \begin{bmatrix} R \\ S \end{bmatrix} = \hat{\mathcal{L}}_0 \begin{bmatrix} R \\ S \end{bmatrix} \tag{3.70}$$

where

$$\hat{\mathcal{L}}_0 = \frac{1}{(z\tilde{I}-1)}\begin{bmatrix} \tilde{I}(1-z) & -\Delta\tilde{I} \\ -\Delta\tilde{I} & -\tilde{I}(1+z) \end{bmatrix}. \tag{3.71}$$

$\hat{\mathcal{L}}_0$ has eigenvectors

$$\mathbf{V_1} = \begin{bmatrix} (z+1) \\ -\Delta \end{bmatrix} \quad (\lambda = 0) \tag{3.72}$$

(3.73)

$$\mathbf{V_2} = \begin{bmatrix} \Delta \\ \\ (z+1) \end{bmatrix} \quad \left(\lambda = -\frac{2\tilde{I}z}{(z\tilde{I}-1)}\right). \tag{3.74}$$

We therefore define new variables ρ and σ such that

$$\begin{bmatrix} R \\ \\ S \end{bmatrix} = \frac{1}{(2z^2+2z)^{\frac{1}{2}}} \begin{bmatrix} (z+1) & \Delta \\ \\ -\Delta & (z+1) \end{bmatrix} \begin{bmatrix} \rho \\ \\ \sigma \end{bmatrix} \tag{3.75}$$

or

$$\mathbf{V} = X\mathbf{V}' \tag{3.76}$$

with $\mathbf{V} = [R, S]^T$, $\mathbf{V}' = [\rho, \sigma]^T$ and X the orthogonal matrix defined by (3.75).

If we write Equation (3.68) in the form

$$\begin{aligned} \partial_t \mathbf{V} &= \hat{\mathcal{L}}\mathbf{V} + N(R,S) \\ &= \hat{\mathcal{L}}(X\mathbf{V}') + N(R(\rho,\sigma), S(\rho,\sigma)) \end{aligned} \tag{3.77}$$

where $\hat{\mathcal{L}}$ and N denote the linear operator and nonlinear terms respectively, then we have

$$\partial_t \mathbf{V}' = (X^{-1}\hat{\mathcal{L}}X)\mathbf{V}' + X^{-1}N(R(\rho,\sigma), S(\rho,\sigma)) \tag{3.78}$$

with $X^{-1}\hat{\mathcal{L}}X$ diagonal at threshold. In terms of ρ and σ the linearised version of (3.68) can be written as

$$\begin{aligned} \partial_t \rho &= -\left[1 + \frac{2\tilde{C}(1-z\tilde{I})}{(1+\tilde{I})^2}\right]\rho - a\left[\nabla^2 + K^2\right]\sigma \\ \\ \partial_t \sigma &= -\left[1 + \frac{2\tilde{C}(1+\tilde{I}z)}{(1+\tilde{I})^2}\right]\sigma + a\left[\nabla^2 + K^2\right]\rho. \end{aligned} \tag{3.79}$$

Now we are at the same stage as we were with Equation (3.36) for the $\Delta = 0$ case. After expressing the nonlinear part in terms of ρ and σ rather than R and S we can adiabatically eliminate σ to give

$$\sigma \simeq \alpha_1\left[a(\nabla^2 + K^2)\rho + \alpha_2\rho a(\nabla^2 + K^2)\rho + \alpha_3\rho^2 + \alpha_4\rho^3\right] \tag{3.80}$$

with

$$\alpha_1 = \frac{(1+\tilde{I})^2}{\left[(1+\tilde{I})^2+2\tilde{C}(1+\tilde{I}z)\right]}$$

$$\alpha_2 = \frac{4\tilde{C}\tilde{I}(z+1)\left[z(\tilde{I}-1)+2\right]}{(2z^2+2z)^{\frac{1}{2}}(1+\tilde{I})\left[(1+\tilde{I})^2+2\tilde{C}(1+\tilde{I}z)\right]}$$

$$\alpha_3 = -\frac{2\tilde{C}\tilde{I}\Delta\left[z(\tilde{I}+3)+2\right]}{(2z^2+2z)^{\frac{1}{2}}(1+\tilde{I})^3}$$

$$\begin{aligned}\alpha_4 = & -\frac{4\tilde{C}^2\tilde{I}^2\Delta\left[z^2(\tilde{I}^2+2\tilde{I}-3)+4z(\tilde{I}+1)+4\right]}{z(1+\tilde{I})^4\left[(1+\tilde{I})^2+2\tilde{C}(1+\tilde{I}z)\right]} \\ & +\frac{2\tilde{C}\tilde{I}\Delta\left[z(\tilde{I}^2+2\tilde{I}-1)+2\tilde{I}\right]}{z(1+\tilde{I})^4}.\end{aligned} \tag{3.81}$$

Substituting (3.80) into the equation for ρ we get the following equation which is the generalisation for arbitrary Δ of Equation (3.40)

$$\begin{aligned}\partial_t\rho = & \left[\frac{2\tilde{C}(z\tilde{I}-1)}{(1+\tilde{I})^2}-1\right]\rho-\frac{a^2(1+\tilde{I})^2}{\left[(1+\tilde{I})^2+2\tilde{C}(1+z\tilde{I})\right]}(\nabla^2+K^2)^2\rho \\ & -\frac{2\tilde{C}\tilde{I}(1+z)\left[z(\tilde{I}-1)-2\right]}{(2z^2+2z)^{\frac{1}{2}}(1+\tilde{I})^3}\rho^2+\frac{2\tilde{C}\tilde{I}\left[z(\tilde{I}-1)^2-2z^2\tilde{I}-2\tilde{I}\right]}{z(1+\tilde{I})^4}\rho^3 \\ & +\frac{2a\tilde{C}\tilde{I}\Delta\left[z(\tilde{I}+3)+2\right]}{(2z^2+2z)^{\frac{1}{2}}(1+\tilde{I})\left[(1+\tilde{I})^2+2\tilde{C}(1+z\tilde{I})\right]}(\nabla^2+K^2)\rho^2 \\ & -\frac{4a\tilde{C}\tilde{I}\Delta\left[z(\tilde{I}-1)-2\right]}{(2z^2+2z)^{\frac{1}{2}}(1+\tilde{I})\left[(1+\tilde{I})^2+2\tilde{C}(1+z\tilde{I})\right]}\rho(\nabla^2+K^2)\rho \\ & -\frac{4a^2\tilde{C}\tilde{I}(1+z)(1+\tilde{I})\left[z(\tilde{I}-1)+2\right]}{(2z^2+2z)^{\frac{1}{2}}\left[(1+\tilde{I})^2+2\tilde{C}(1+z\tilde{I})\right]^2}(\nabla^2+K^2)\left[\rho(\nabla^2+K^2)\rho\right] \\ & -\frac{a(1+\tilde{I})^2\alpha_4}{\left[(1+\tilde{I})^2+2\tilde{C}(1+z\tilde{I})\right]}(\nabla^2+K^2)\rho^3\end{aligned}$$

$$+\frac{8\tilde{C}^2\tilde{I}^2\Delta^2\left[z(\tilde{I}+3)+2\right]\left[z(\tilde{I}-1)-2\right]}{(2z^2+2z)(1+\tilde{I})^4\left[(1+\tilde{I})^2+2\tilde{C}(1+z\tilde{I})\right]}\rho^3+O(\rho^4). \tag{3.82}$$

This equation looks considerably more complicated than Equation (3.40) but the same sort of information can be gained from it. All the terms which can lead to quadratic coupling vanish when $\tilde{I}=(2+z)/z$ which is the value of $\tilde{I}$ which corresponds to the absolute minimum threshold: that is, the value of $\tilde{I}$ at the "base" of the threshold surface (see Equations (3.15) and (3.16) and Figure 3.2). Thus we expect the same kind of pattern phenomonology for general Δ as we predict for the specific case $\Delta=0$: namely, the H^+ to roll to H^- transition on varying $\tilde{I}$ with $\tilde{C}$ constant. In addition Equation (3.82) indicates that the cubic coefficient of ρ can change sign and so again we anticipate the existence of subcritical bifurcations. Lastly, it is easily verified that when $\Delta=0$, $\rho=R$, $\tilde{I}=I$ and $\tilde{C}=C$, (3.82) becomes (3.40).

We now proceed to do the multiple scales analysis on Equation (3.82) for a hexagonal pattern, this time omitting multiple space scales as an unnecessary complication. The procedure is exactly the same as that described in Section 3.4.2 but with a lot more algebra, so we quote only the final result:

$$\partial_t A = \mu A+\alpha B^*D^*-\zeta|A|^2A-\gamma(|B|^2+|D|^2)A \tag{3.83}$$

with

$$\mu = \left[\frac{2\tilde{C}(z\tilde{I}-1)}{(1+\tilde{I})^2}-1\right]$$

$$\alpha = \frac{\tilde{I}(z+1)\left[z(1-\tilde{I})+2\right]}{(2z^2+2z)^{\frac{1}{2}}(z\tilde{I}-1)(1+I)}\left[1-\frac{A_0\tilde{I}(z+1)\left[z(1-\tilde{I})+2\right]}{(2z^2+2z)^{\frac{1}{2}}(z\tilde{I}-1)(1+I)}\right]$$

$$\gamma = -\frac{5\tilde{I}^3(z+1)\left[z(1-\tilde{I})+2\right]^2}{4a^2K_c^4(1+\tilde{I})^2(z\tilde{I}-1)^3}-\frac{\tilde{I}^2\Delta(z+1)\left[z(1-\tilde{I})+2\right]}{zaK_c^2(1+\tilde{I})^2(z\tilde{I}-1)^2}$$

$$-\frac{\tilde{I}}{4z^2(1+\tilde{I})^2(z\tilde{I}-1)}\left[6z\left[z(\tilde{I}-1)^2-2\tilde{I}z^2-2\tilde{I}\right]\right.$$

$$\left.-(z-1)\left[z(\tilde{I}+3)+2\right]\left[z(1-\tilde{I})+2\right]\right]$$

$$\zeta = -\frac{19\tilde{I}^3(z+1)\left[z(1-\tilde{I})+2\right]^2}{18a^2K_c^4(1+\tilde{I})^2(z\tilde{I}-1)^3} - \frac{5\Delta\tilde{I}^2(z+1)\left[z(1-\tilde{I})+2\right]}{3zaK_c^2(1+\tilde{I})^2(z\tilde{I}-1)^2}$$

$$-\frac{3\tilde{I}}{4z(1+\tilde{I})^2(z\tilde{I}-1)}\left[z(\tilde{I}-1)^2-2\tilde{I}z^2-2\tilde{I}\right] \tag{3.84}$$

and A_0 again represents the value of the steady–state solution of system (3.83) given by $A = B = D = A_0$.

Once again an examination of the two–mode problem shows that the cubic cross–coupling coefficient is independent of the angle between the two modes when quadratic coupling is absent ($\tilde{I} = (2+z)/z$):

$$\gamma_{ij} = -\frac{3\tilde{I}\left[z(\tilde{I}-1)^2-2z^2\tilde{I}-2\tilde{I}\right]}{2z(1+\tilde{I})^2(z\tilde{I}-1)} \tag{3.85}$$

and $\gamma_{ij} = \gamma = 2\zeta$. The result derived on the basis of the Lyapunov function for the $\Delta = 0$ case therefore carries over to the general case: namely, that rolls are the expected pattern when the quadratic coupling vanishes.

3.5 Numerical Analysis

We have developed two numerical codes to integrate Equation (3.3) on a square grid with periodic boundary conditions: the principal one using a split–step method, the other a finite–difference Hopscotch algorithm (Appendix A). Our initial condition is generally chosen to be small amplitude noise whose Fourier Transform is filtered to avoid large gradients in the initial field, and the length of the computational box is set at eight times the critical wavelength λ_c ($= 2\pi/K_c$).

Since the same kind of behaviour is seen with positive, negative and zero values of Δ, we concentrate on the $\Delta = 0$ case initially because analytically it is the simplest. We also choose $\theta = -1$ and $a = 1$ to give a convenient length scale ($K_c = 1$). Sequences of simulations are carried out by keeping one of the two control parameters, C or I, constant, and varying the other. In this way the

threshold values of C and I given by the linear stability analysis of Section 3.3 have been confirmed to within 1%.

Selecting a value of C greater than 4 and increasing I to cross the instability region in $(I, \theta + aK^2, C)$ space, we observe a transition in the stable pattern which forms from noise: from H^+ hexagons to rolls to H^- hexagons, with the H^+ and H^- existing on either side of $I = 3$ as the nonlinear analysis of Section 3.4.2 predicts. For $I = 3$, and in a region around $I = 3$, rolls emerge as the stable pattern arbitrarily close to threshold, again as we would expect from the analysis. Near the boundary between a region where the stable pattern is a roll and one where it is one of the two types of hexagon, we often observe roll–hexagon competition: domains of both patterns form from noise, whereupon one pattern invades the other, eventually winning (see Figures 3.8 and 3.9). The classic topological defects of two–dimensional patterns (e.g. dislocations for rolls and penta–hepta pairs for hexagons [43]) are most easily observed in these stability boundary regions: the coalescence of domain boundaries when one pattern invades a domain of another can easily lead to defects (Figure 3.9). The stable co–existence of rolls and hexagons has not been observed. If we move into the instability region by keeping I constant but varying C, we see, except in the region of $I = 3$, the formation of H^+ or H^- close to threshold followed by the expected transition to rolls on further increase of C.

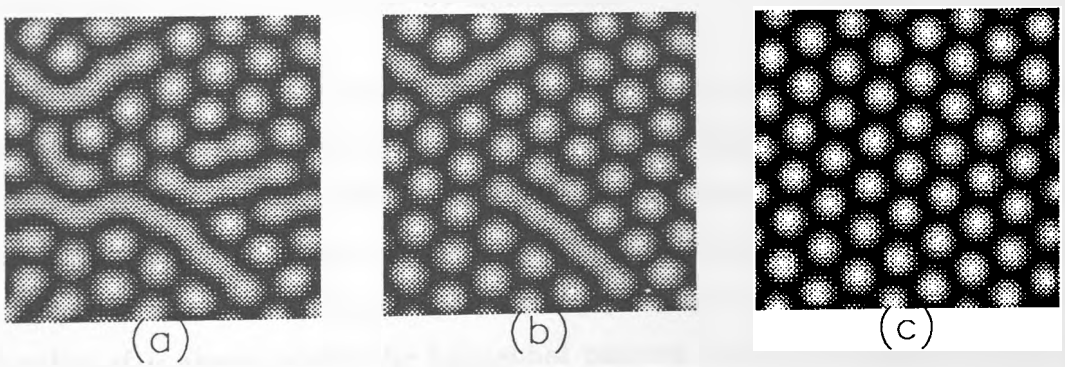

Figure 3.8: *Time sequence showing roll–hexagon competition with hexagons winning. The figures show the real part of the field at (a) t=240, (b) t=1440, (c) t=2640 cavity lifetimes.* $\Delta = 0$, $\theta = -1$, $I = 2.5$, $C = 5$. *Light grey represents high field values, dark grey represents low field values.*

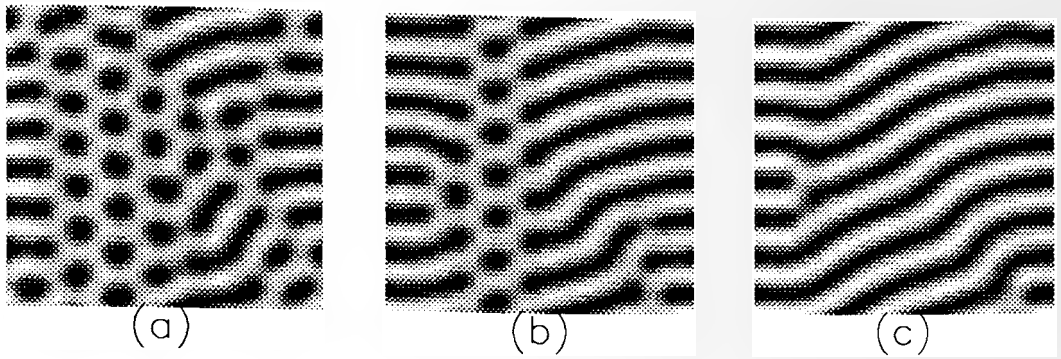

Figure 3.9: *Time sequence showing roll–H^+ competition with rolls winning. The figures show the real part of the field at (a) t=240, (b) t=400, (c) t=560 cavity lifetimes.* $\Delta = 0$, $\theta = -1$, $I = 5.5$, $C = 5$. *The defects in the roll pattern persist with no perceptible change until the end of the simulation (t=3600 cavity lifetimes).*

All of this behaviour agrees qualitatively, and much of it quantitatively, with the three-mode amplitude equations (3.54). For example for $I = 3$ Figure 3.10 compares the amplitude of the roll pattern as a function of C as predicted by the amplitude equations with the values obtained from numerical integration of the model equation; Figure 3.11 shows a similar comparison for a hexagonal pattern at $I = 2.2$. In both of these cases the quantitative agreement is quite good. We also find that the amplitude equations correctly predict the transition from a supercritical to a subcritical bifurcation in roll patterns; for $\theta = -1$ and $\Delta = 0$ we predict that rolls are supercritical for $I \in (2.143..., 4.167...)$ and subcritical elsewhere and this is borne out by simulations.

So far the analysis seems to be holding up quite well. However, when we try to predict quantitatively where the transitions between the hexagon and roll patterns occur as we vary I across the instability region we run into trouble. Figure 3.12 shows the analytical prediction for which pattern should be stable as a function of I when $C = 4.4$. The figure is a plot of $\mu_4 - \mu$ as a function of I where μ_4 is the value of μ above which the hexagonal pattern becomes unstable to the roll pattern (see Section 3.4.1). There may be some ambiguity in this as a procedure for determining which pattern should be observed since according to Figure 3.6 there exists a range of μ for which both hexagons and rolls are stable. To obtain a

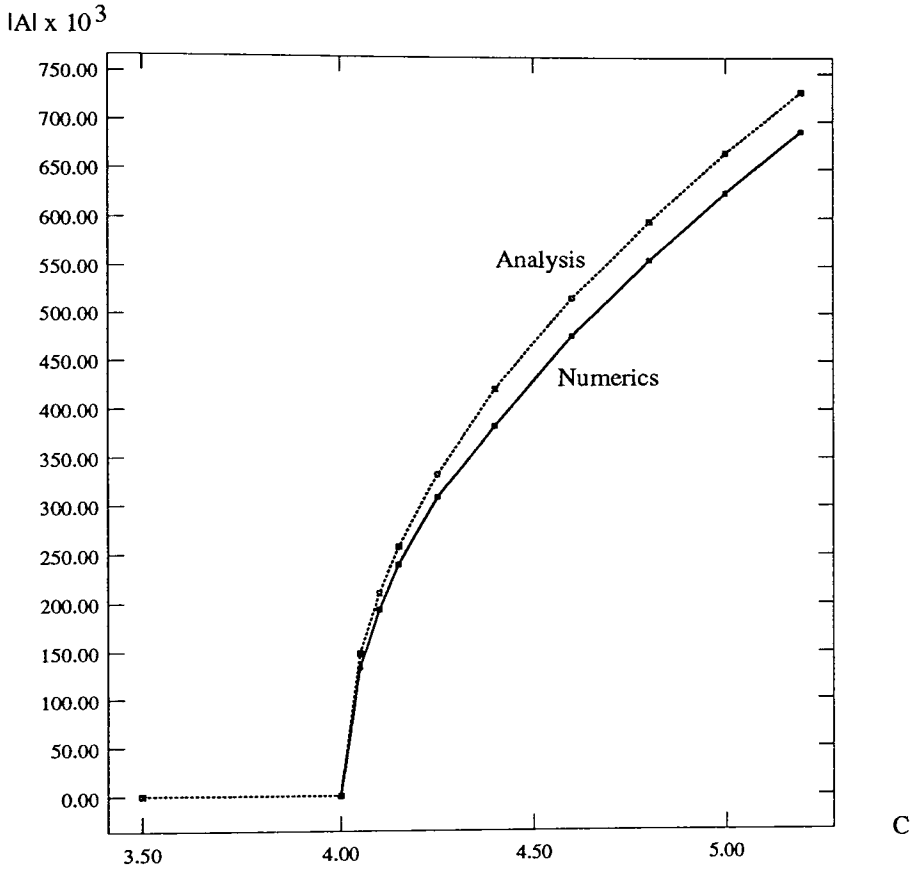

Figure 3.10: *Comparison between numerical and analytic values of the roll amplitude as a function of* C *for* $\Delta = 0$, $\theta = -1$, $I = 3$.

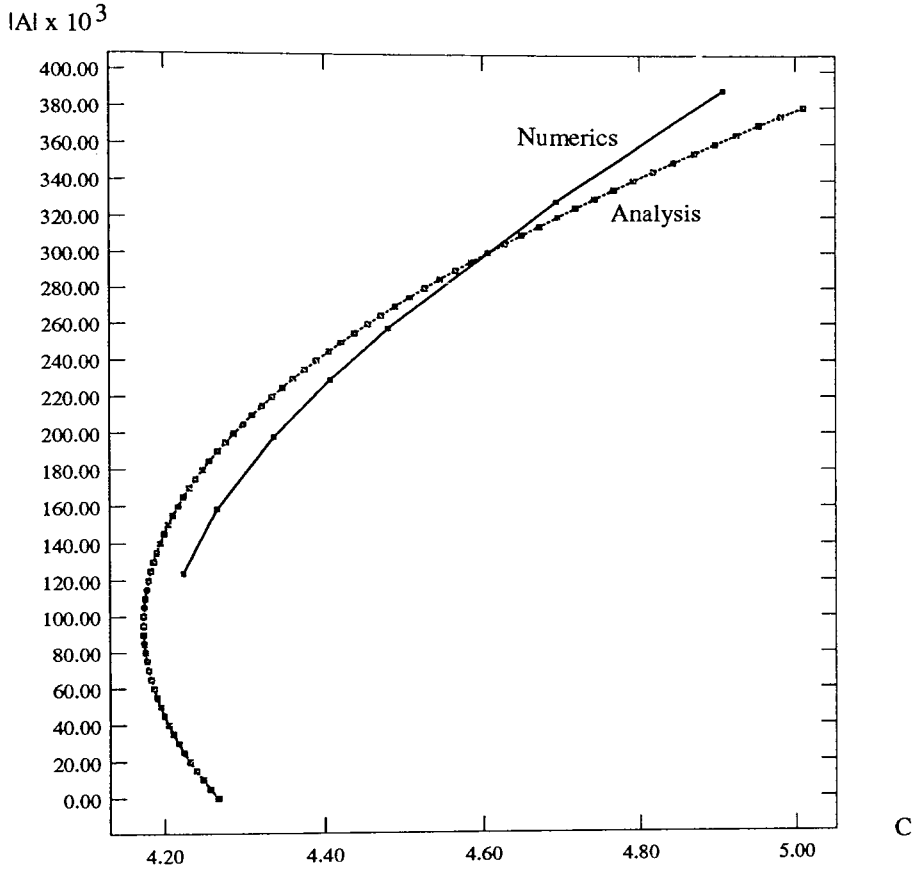

Figure 3.11: *Comparison between numerical and analytic values of the hexagon amplitude as a function of* C *for* $\Delta = 0$, $\theta = -1$, $I = 2.2$.

numerical comparison with the curve in Figure 3.12 we therefore use a hexagonal field as the initial condition so that we are determining the upper bound on the stability of the hexagons in the numerics as we are in the analysis.

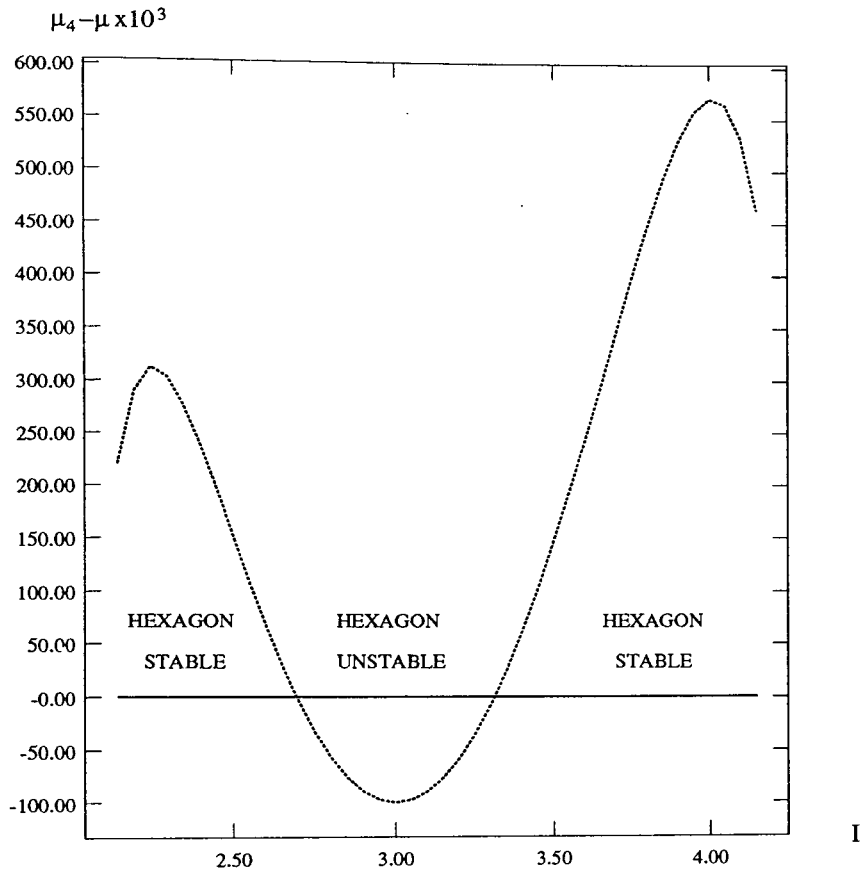

Figure 3.12: *Plot of $\mu_4 - \mu$ as a function of I for $C = 4.4$, $\theta = -1$, $\Delta = 0$ showing the expected pattern.*

We find from simulations that the H^+ go unstable to rolls somewhere in the interval $I \in (3.1..3.3)$ and that the H^- become unstable in $I \in (4.3..4.5)$. It can be seen from Figure 3.12 that the agreement between the analysis and the numerics is not too good and a reason can be found for this. One of the first assumptions we made when performing the weakly nonlinear analysis of Section 3.4.2 was that $\mathcal{A} + \mathcal{A}^* + |\mathcal{A}|^2 < (1 + I)/I$ where $\mathcal{A}_{max} \simeq R_{max} \simeq 3A_0$ for a hexagonal pattern. A glance at Figure 3.11 shows that for $I = 2.2$ this condition is violated even quite close to threshold. Since the amplitude of the hexagonal pattern at threshold increases as $|\alpha|$ increases, where α is the quadratic coupling coefficient, this situation becomes even worse the further we move from $I = 3$. Therefore,

while it may give the correct qualitative behaviour, the quantitative predictions of the weakly nonlinear analysis cannot be guaranteed for any significant distance above threshold.

In principle the situation is slightly better for rolls than for hexagons since at threshold the roll amplitude is zero and continuous while the hexagon amplitude is already non–zero. However, even for rolls the analysis eventually breaks down. For example, a hexagonal pattern is a stable solution when $I = 3$ and $C = 4.4$ (10 % above threshold) indicating that the perturbative result that the quadratic coefficient should vanish at $I = 3$ no longer holds.

Results for the case $\Delta \neq 0$ are broadly similar to those for $\Delta = 0$. For example, on increasing I with C held constant we see the same H^+ to roll to H^- transition in the observed stable pattern. The vanishing of quadratic coupling is again confirmed by the observation of roll patterns close to threshold for $\tilde{I} = (2+z)/z$. The amplitude equations also correctly predict the supercritical to subcritical transition for rolls. However, the same limitations on the validity of the nonlinear analysis obviously exist as for the $\Delta = 0$ case.

So far in this chapter all of the analysis and simulations have treated the case where the external pump field, parameterised by E_I in Equation (3.3), is a plane–wave. This enables us to obtain quantitative analytical predictions which we can compare with the results of simulations. In an experiment, however, the pump will have a variation, probably gaussian in shape, in the plane transverse to the direction of propagation. In the final part of this section we therefore briefly address the more realistic case where the pump field has a finite transverse extent.

An examination of the derivation of the mean–field model in Chapter 2 shows that we are free to regard E_I in Equation (3.3) as a function of the transverse co–ordinates so long as the spatial extent of this function is larger than the scale of the pattern. This function should represent the transverse variation of the pump field at the entrance to the nonlinear medium. With this in mind, Equation (3.3) can then be used with the constant E_I replaced by a function of the transverse

co–ordinates. In the interests of computational efficiency we use a tophat pump rather than a gaussian pump; that is, something of the form

$$E_I(x,y) = \frac{A}{2}\left[1 - \tanh\left(\kappa\left((x^2+y^2)^{\frac{1}{2}} - p\right)\right)\right]. \tag{3.86}$$

A gives the amplitude of the pump at the origin, κ determines its gradient at the edge and p fixes the width of the pump.

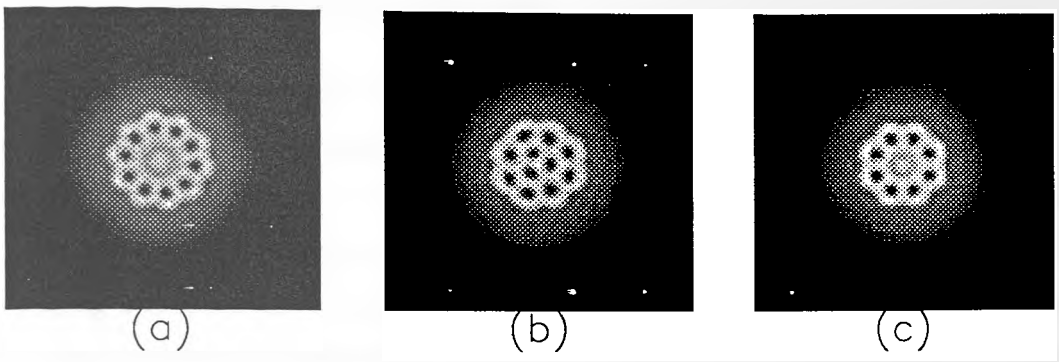

Figure 3.13: *Stationary patterns with a finite pump.* $\Delta = 0$, $\theta = -1$, $C = 5$, $A = 6.51$ *(a)* $p = 26.7$, *(b)* $p = 25.9$, *(c)* $p = 25.1$.

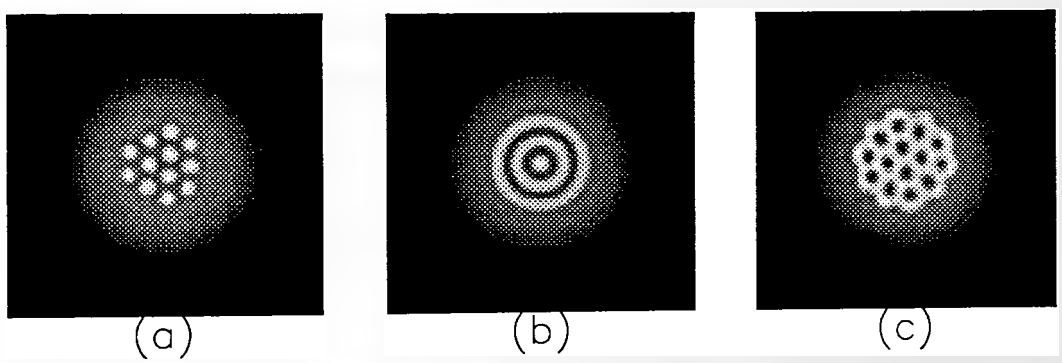

Figure 3.14: *Stationary patterns with a finite pump.* $\Delta = 0$, $\theta = -1$, $C = 5$, $p = 27.5$ *(a)* $A = 6.28$, *(b)* $A = 6.45$, *(c)* $A = 6.5$.

With a source term in Equation (3.3) which depends on the transverse co–ordinates we can no longer perform a linear stability analysis since we are unable to determine analytically the zero–order solution around which to do the analysis. It is possible to predict the kind of solution which may emerge from any symmetry breaking bifurcation, however, from considerations of the symmetry of the

full problem (equation plus boundary conditions) [26]. With a pump field which is radially symmetric the symmetry of the problem corresponds to the O_2 group, rather than to the euclidean group E_2 of the plane–wave pump case. This means that the constraint of bifurcation to patterns with discrete translational symmetries is no longer applicable i.e. in principle we are not restricted to patterns which will tile the plane. We may then expect amongst other things solutions with patterns of spots corresponding to the subgroups D_n of O_2, rather than the hexagons or rolls of the plane–wave case.

In numerical simulations of Equation 3.3 with a finite pump we observe the formation of patterns with varying numbers of "spots", consisting of both peaks on the background and dips in the background (Figure 3.13). We also see patterns consisting of concentric rings, which are just rolls bent around on themselves by the strong effects of the boundary, as in Figure 3.14. More importantly, the transition from a pattern consisting of peaks to rings to a pattern consisting of dips is observed as A is increased (Figure 3.14), just as in the plane–wave case when the pump amplitude is varied across the instability domain. It can be seen that even for the relatively narrow pump size used for Figure 3.14 the patterns of spots are still almost hexagonally co–ordinated. This suggests that the plane–wave pump results also have some relevance to the situation where a finite pump is used.

3.6 Conclusion

In this chapter we have examined pattern formation in a simple model of a two–level medium in an optical cavity. After identifying the instability domain, we used a weakly nonlinear analysis to obtain a guide to the type of pattern we would expect to see for different parameter values. While many of these predictions were borne out by numerical simulation, it was also possible to identify places where the nonlinear analysis broke down and also why. The limited range of validity of normal form equations such as (3.27) is something that should always be kept in mind. Nevertheless, their usefulness in identifying possible structures and

the nature of bifurcations has been demonstrated and the understanding of this system which they allow will be put to further use in Chapter 5.

Finally, the fact that the rich behaviour of this system may persist even when the pump beam is quite narrow leads us to hope that the same variety of patterns could be seen in an experimental realisation of this sytem as have been observed here.

Chapter 4

Four Level System with Feedback Mirror

4.1 Introduction

In the previous chapter we examined the pattern–forming characteristics of a two–level medium in an optical cavity. Such a configuration is just one way of providing the feedback necessary for a nonlinear optical system to exhibit self–organising behaviour. Another technique, valued by both theorists and experimentalists because of its elegance and simplicity, is the use of a single feedback mirror. Feedback mirror systems involving Kerr media have already proved to be very useful for the purpose of comparing simple theoretical models and numerical simulations with experiments [24–33]. The results of such comparisons have been fairly impressive.

The system studied in this chapter consists of a thin sample of an alkali vapour medium placed in front of a flat feedback mirror and driven by an incident optical field which we allow, in general, to consist of two orthogonally polarised components. The frequency of the field is chosen such that it interacts with what is effectively a four–level medium. For the special case in which the input field is

circularly polarised the system can be described by a scalar field model. It should be noted, though, that the nature of the nonlinearity is such that the material is not describable as a Kerr medium so that even in this instance the model equations do not reduce to those of D'Alessandro and Firth [24,25]. The system itself is based on an experimental arrangement used by Grynberg and co–workers [34] and is also similar to the setup used by Ackeman and Lange [35], both of which systems have recently been shown to display pattern–formation.

Following the usual approach, our linear and nonlinear analysis, as well as our numerics, examine the case where the driving fields are plane–wave, which is valid when the real fields are broad in comparison with the length scale of the pattern.

4.2 Model Equations

The system that we aim to study is shown schematically in Figure 4.1. As already mentioned in the Introduction, it consists of an alkali vapour cell placed a distance d in front of a feedback mirror which has amplitude reflection coefficient r. The medium is driven by two optical fields which have different polarisations but the same frequency, chosen such that they are nearly resonant with a $J_g = 1/2 \rightarrow J_e = 1/2$ transition in the medium (Figure 4.2). We will assume that there is no external magnetic field and hence no splitting of the Zeeman sublevels.

The relevant physics in the pattern–forming process can be described quite simply. The nonlinearity is provided by an optical pumping process [46]. The left (σ_-) and right (σ_+) circularly polarised components of the field drive the transitions in the medium shown in Figure 4.2 so that, with fast relaxation of the population from the excited state to the ground state, the effect of each field component is to transfer population from one ground state Zeeman sublevel to the other. Any difference in population between these two levels results in a non–zero value for $\langle J_z \rangle$, the expectation value of the z–component of the angular momentum. This in turn means that the medium will rotate the x– and y– components of the field

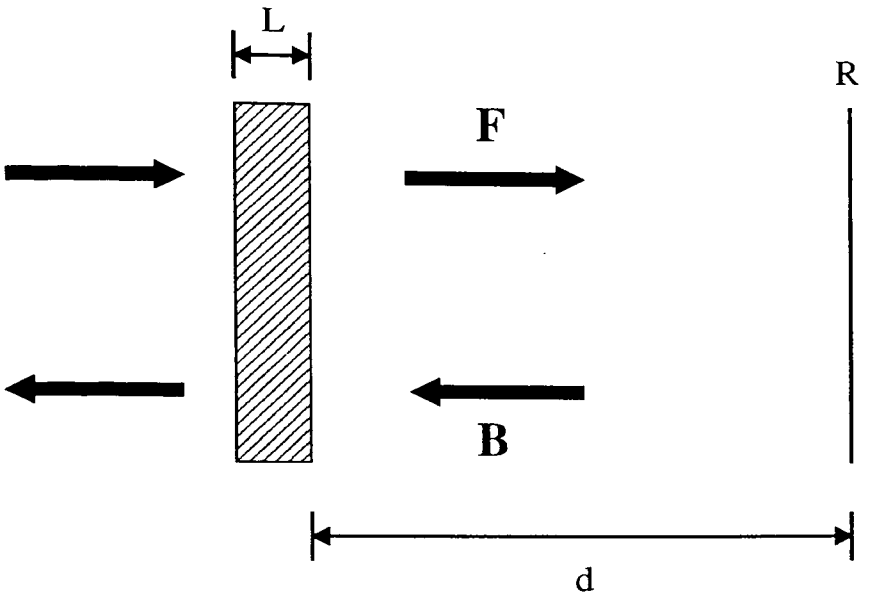

Figure 4.1: *Schematic of the feedback mirror configuration.*

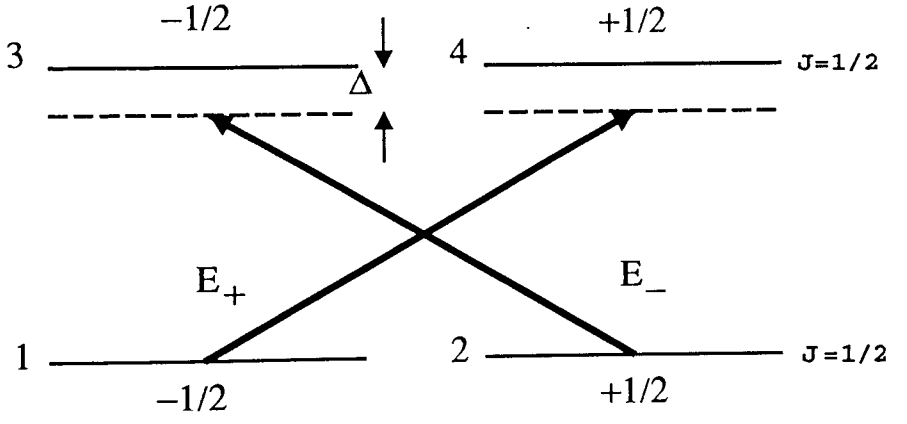

Figure 4.2: *Energy level diagram for the four–level system.*

by means of the Faraday effect. This rotation is the equivalent of a phase change in each of the circular components, and if we recognise the fact that the medium properties can vary in space, we have the possibility of a spatially dependent phase modulation of the electric field.

After passing through the medium there is then a region of free–space propagation, including reflection from the mirror, by which the phase–modulation produces an amplitude modulation. This is necessary since the medium is only driven by the intensity of the optical field and a purely phase–modulated feedback beam would carry no information to the medium. With the diffraction present, however, any spatial dependence of the medium excitation results in a spatially varying forcing when the field returns after its round–trip to the mirror and back. We have then provided the final necessary conditions for pattern formation: namely, that the nonlinear medium be able to "look at itself".

To model this process we must first of all write Bloch equations for the four–level medium. This follows the general procedure outlined in Chapter 2 and is done in Appendix B. Since in the alkali vapour media that we are modelling the relaxation from the excited state to the ground state is fast, we assume that there is essentially no population in the upper state so that

$$\rho_{33} \approx 0 \tag{4.1}$$

$$\rho_{44} \approx 0 \tag{4.2}$$

$$\rho_{34} \approx 0. \tag{4.3}$$

We also assume that we can adiabatically eliminate ρ_{13}, ρ_{14}, ρ_{23} and ρ_{24}. When we do this (Appendix B) the system reduces to an effective two–level system consisting of the ground state Zeeman sublevels which are coupled to each other via the excited state. The medium can then be described in terms of the variables u, v and w where

$$\begin{aligned} u &= \rho_{12} + \rho_{21} \\ v &= i(\rho_{12} - \rho_{21}) \\ w &= \rho_{11} - \rho_{22}. \end{aligned} \tag{4.4}$$

In the absence of an external magnetic field the equation for w decouples from the others and since it is $\langle J_z \rangle = -\hbar w/2$ which provides the interaction with the electric field we can reduce our description of the medium to the single equation for w.

The interaction with the medium is most easily described if we express the electric field in terms of circularly polarised components. We therefore write the field $\mathcal{E}$ as

$$\mathcal{E} = -\frac{1}{2}\left(E_- e^{i\omega t}\hat{e}_+ - E_-^* e^{-i\omega t}\hat{e}_- + E_+ e^{i\omega t}\hat{e}_- - E_+^* e^{-i\omega t}\hat{e}_+\right) \tag{4.5}$$

where

$$\hat{e}_\pm = \mp\frac{1}{\sqrt{2}}(\hat{e}_x \pm i\hat{e}_y) \tag{4.6}$$

so that

$$\begin{aligned} E_+ &= -\frac{1}{\sqrt{2}}(E_x + iE_y) \\ E_- &= \frac{1}{\sqrt{2}}(E_x - iE_y) \\ E_x &= -\frac{1}{\sqrt{2}}(E_+ - E_-) \\ E_y &= \frac{i}{\sqrt{2}}(E_+ + E_-)\,. \end{aligned} \tag{4.7}$$

Then the equation for w reads (Appendix B)

$$\partial_t w = -\left(\gamma + \frac{\mu_E^2(|E_+|^2 + |E_-|^2)}{4\hbar^2\Gamma(1+\bar{\Delta}^2)}\right)w + \frac{\mu_E^2(|E_-|^2 - |E_+|^2)}{4\hbar^2\Gamma(1+\bar{\Delta}^2)} \tag{4.8}$$

where μ_E is the reduced electric dipole matrix element, Γ is the decay rate of the coherences ρ_{13}, ρ_{14}, ρ_{23} and ρ_{24}, $\bar{\Delta} = \Delta/\Gamma$ where $\Delta = \omega_0 - \omega$ is the atomic detuning and ω_0 is the frequency of the atomic transition. The intrinsic relaxation time, $1/\gamma$, of w is on the order of microseconds [46]. Note that w is driven by the difference between the two polarisations' intensities, while its decay rate increases with their sum.

We can define a polarisation for the medium using the relation

$$\mathcal{P} = n_a Tr(\boldsymbol{\mu}\rho) \tag{4.9}$$

with n_a the atomic number density and

$$\mathcal{P} = -\frac{1}{2}\left(P_- e^{i\omega t}\hat{e}_+ - P_-^* e^{-i\omega t}\hat{e}_- + P_+ e^{i\omega t}\hat{e}_- - P_+^* e^{-i\omega t}\hat{e}_+\right). \tag{4.10}$$

Doing this we find (Appendix B)

$$\begin{aligned} P_\pm &= \frac{n_a \mu_E^2 (\bar{\Delta} - i)}{2\hbar\Gamma(1+\bar{\Delta}^2)}(1 \pm w)E_\pm \\ &= \epsilon_0 \chi_\pm E_\pm. \end{aligned} \tag{4.11}$$

The influence of the medium on the field can therefore be described in terms of complex nonlinear susceptibilities $\chi_\pm$ which in turn depend on the electric field via the variable w. To simplify the problem we assume that our medium exists as a thin slice so that, for reasonable detunings, we can neglect absorption [34]; in other words we ignore the imaginary part of $\chi_\pm$. In this way we have that w is independent of z, making the problem reasonably tractable both analytically and numerically. In that case we write

$$P_\pm = \epsilon_0 \chi_0 (1 \pm w) E_\pm \tag{4.12}$$

where

$$\chi_0 = \frac{n_a \mu_E^2 \bar{\Delta}}{2\hbar\Gamma\epsilon_0(1+\bar{\Delta}^2)}. \tag{4.13}$$

Now we note that in this system we actually have both forward and backward propagating fields of each polarisation:

$$\begin{aligned} E_+ &= F_+ e^{-ikz} + B_+ e^{+ikz} \\ E_- &= F_- e^{-ikz} + B_- e^{+ikz}. \end{aligned} \tag{4.14}$$

We will neglect the terms which go like $\cos(2kz)$ resulting from the interference between the counter–propagating beams, assuming that the atomic motion "washes out" the effect of these terms, in which case

$$\begin{aligned} |E_+|^2 &= |F_+|^2 + |B_+|^2 \\ |E_-|^2 &= |F_-|^2 + |B_-|^2. \end{aligned} \tag{4.15}$$

Equations (4.12) and (4.13) show that the polarisation is basically of the same form as the polarisation for the two–level system and therefore the field equation

(2.19) is applicable here. If in addition we assume that the dynamics of the fields are almost instantaneous on the slower time scale of the medium dynamics, we can make an adiabatic approximation and write the equations describing the propagation of the forward and backward travelling fields through the medium as

$$\begin{aligned} \partial_z F_\pm &= -\frac{ik\chi_0}{2}(1 \pm w)F_\pm \\ \partial_z B_\pm &= -\frac{ik\chi_0}{2}(1 \mp w)B_\pm. \end{aligned} \tag{4.16}$$

Along with these we have the equation which describes the medium dynamics to which we will add a term to represent diffusion in the medium since this is a process which is likely to be taking place:

$$\partial_t w = -\left(\gamma + \frac{\mu_E^2(|E_+|^2 + |E_-|^2)}{4\hbar^2\Gamma(1+\bar{\Delta}^2)}\right)w + \frac{\mu_E^2(|E_-|^2 - |E_+|^2)}{4\hbar^2\Gamma(1+\bar{\Delta}^2)} + \gamma D\nabla^2 w \tag{4.17}$$

where $D = l_D^2$ is the diffusion coefficient and l_D is the diffusion length.

To make things easier to handle and to make sure that the parameters and variables are all roughly of $O(1)$ we perform the following rescalings

$$\begin{aligned} (x,y,z) &\rightarrow l_D^{-1}(x,y,z) \\ t &\rightarrow \gamma t \\ E &\rightarrow \frac{\mu_E E}{2\hbar\sqrt{\Gamma\gamma(1+\bar{\Delta}^2)}} \end{aligned} \tag{4.18}$$

and define

$$\begin{aligned} \phi &= -\frac{1}{2}w \\ k' &= kl_D \\ \alpha &= k'\chi_0. \end{aligned} \tag{4.19}$$

Then in the medium we finally have that

$$\partial_z F_\pm = \pm i\alpha\phi F_\pm \tag{4.20}$$

$$\partial_z B_\pm = \mp i\alpha\phi B_\pm \tag{4.21}$$

$$\begin{aligned}\partial_t\phi &= -\left(1+|F_+|^2+|B_+|^2+|F_-|^2+|B_-|^2\right)\phi \\ &\quad +\frac{1}{2}\left(|F_+|^2+|B_+|^2-|F_-|^2-|B_-|^2\right)+\nabla^2\phi. \qquad (4.22)\end{aligned}$$

Notice that we have omitted the terms in (4.20) and (4.21) representing a constant phase shift. Because of the nature of the driving terms in (4.22) these constant phase shifts play no rôle in the field–medium interaction and leaving them in just makes for unnecessary algebra.

To close the system we have to add equations governing the propagation of the optical fields to the mirror and back through free space. These are

$$\partial_z F_\pm = \frac{i}{2k'}\nabla^2 F_\pm \qquad (4.23)$$

$$\partial_z B_\pm = -\frac{i}{2k'}\nabla^2 B_\pm. \qquad (4.24)$$

The set of equations (4.20) to (4.24) then constitutes our model of the feedback mirror system.

At this stage a small quirk of nomenclature should be pointed out. After reflection from the feedback mirror a circularly polarised field changes its polarisation: $\sigma_\pm \rightarrow \sigma_\mp$. However, the direction of the vector representing the angular momentum carried by the field does not change on reflection so that the field drives the same transition on its way back from the mirror as it does on its way to the mirror. For this reason we use the subscript "+" to refer to a field which drives the $J_g = 1/2, m = -1/2 \rightarrow J_e = 1/2, m = 1/2$ transition irrespective of its polarisation. Similarly, the "−" subscript denotes a field which drives the other transition. Thus the longitudinal boundary condition at the mirror ($z = d$) reads

$$B_\pm(z=d) = rF_\pm(z=d). \qquad (4.25)$$

4.3 Linear Stability Analysis

The system (4.20) to (4.24) possesses a homogeneous, time–independent solution given by

$$\begin{aligned}\phi_0 &= \frac{|F_+^0|^2 + |B_+^0|^2 - |F_-^0|^2 - |B_-^0|^2}{2 + 2(|F_+^0|^2 + |B_+^0|^2 + |F_-^0|^2 + |B_-^0|^2)} \\ &= \frac{(1+R)(I_+ - I_-)}{2 + 2(1+R)(I_+ + I_-)}\end{aligned} \tag{4.26}$$

$$\left.\begin{aligned} F_\pm^0(z) &= e^{\pm i\alpha\phi_0 z} F_\pm^0(0) \\ B_\pm^0(z) &= re^{\pm i\alpha\phi_0(2L-z)} F_\pm^0(0) \end{aligned}\right\} 0 \le z < L$$

where $R = |r|^2$ and $I_+ = |F_+^0|^2 = |B_+^0|^2/R$, $I_- = |F_-^0|^2 = |B_-^0|^2/R$.

The linear stability analysis of this solution is most easily performed by formally integrating the field equations and reducing the whole system to a single nonlinear P.D.E. for ϕ. We will do this in any case when we turn to nonlinear analysis to investigate pattern selection. For the linear analysis, however, we will follow a procedure similar to that adopted for the Kerr slice problem [24] which has the advantage of making clear the physical origins of the pattern–forming instability.

We consider a perturbation, $\Delta\phi$, to the medium excitation which in turn produces perturbations in the fields propagating forwards through the medium. After travelling to the mirror and back these perturbations re–enter the problem as perturbations to the backward fields which drive the medium. Thus we write

$$\begin{aligned}\phi &= \phi_0 + \Delta\phi \\ B_+ &= B_+^0(1 + b_+(x,t)) \\ B_- &= B_-^0(1 + b_-(x,t))\end{aligned} \tag{4.27}$$

and substitute (4.27) into (4.22), the equation for the medium, keeping only terms

up to first order in $\Delta\phi$ and $b_\pm$:

$$\begin{aligned} & \partial_t(\Delta\phi) + \Delta\phi - \nabla^2(\Delta\phi) + (1+R)(I_+ + I_-)\Delta\phi \\ = \; & \frac{R}{2}\left(I_+(b_+ + b_+^*)(1-2\phi_0) - I_-(b_- + b_-^*)(1+2\phi_0)\right). \end{aligned} \tag{4.28}$$

We can relate the Fourier transform of $b_\pm$ to the Fourier transform of $\Delta\phi$ at an earlier time by using first Equation (4.20) to propagate the input fields through the nonlinear medium and then (4.23) and (4.24) to propagate to the mirror and back. The result is

$$\begin{aligned} \tilde{b}_+(t+t_R, K) &= i\alpha L e^{-i\theta}\Delta\tilde{\phi}(t,K) \\ \tilde{b}_-(t+t_R, K) &= -i\alpha L e^{-i\theta}\Delta\tilde{\phi}(t,K) \end{aligned} \tag{4.29}$$

where a tilde denotes the Fourier Transform, t_R is the round-trip time to the mirror and back and

$$\theta = 2\left(\frac{K^2 d}{2k'}.\right) \tag{4.30}$$

At an instability threshold we can write $\Delta\tilde{\phi} = \beta Re(e^{-i\Omega t})$ where we allow for the fact that the bifurcation may be Hopf rather than steady-state. Substituting this into the Fourier Transform of Equation (4.28) gives the defining equation for the stability surface

$$1+K^2+(1+R)(I_+ + I_-) - i\Omega = \frac{R\alpha L\sin(\theta)e^{i\Omega t_R}}{1+(1+R)(I_+ + I_-)}(I_+ + I_- + 4(1+R)I_+I_-). \tag{4.31}$$

As a first step in analysing (4.31) we can show that the steady-state bifurcation ($\Omega = 0$) has the lowest threshold and is therefore the relevant one.

From Equation (4.31) we have

$$\frac{|\Gamma|\,(I_+ + I_- + 4(1+R)I_+I_-)}{(1+(1+R)\,(I_+ + I_-))\,(1+K^2+(1+R)\,(I_+ + I_-))} = |\sec(\Omega t_R)| \tag{4.32}$$

where $\Gamma = R\alpha L\sin(\theta)$ and Ω is a solution of

$$\frac{-\Omega}{1+K^2+(1+R)\,(I_+ + I_-)} = \tan(\Omega t_R). \tag{4.33}$$

There are obviously an infinite number of solutions to (4.33), but $\Omega = 0$ is the one which minimises the right hand side of (4.32). Since the left hand side of (4.32) is a function which is zero when there is no input field and is continuous for all physically meaningful values of its arguments, the threshold for $\Omega = 0$ is the one which will be crossed first when either I_+ or I_- (or both) is/are increased from 0. From now on we will therefore ignore the case $\Omega \neq 0$.

With $\Omega = 0$ in Equation (4.31) we immediately obtain the condition $\alpha L \sin(\theta) > 0$. For $\alpha > 0$ (a "self–focusing" medium) this can first be satisfied for $0 < \theta < \pi$ while for $\alpha < 0$ the condition is first satisfied for $\pi < \theta < 2\pi$. This means that the spatial scale of near threshold patterns for focusing media will be larger than that for defocusing media.

The problem can now be analysed in the space of the parameters I_+, I_- and K^2. We can write (4.31) in the form

$$F(I_+, I_-, K^2) = 0 \tag{4.34}$$

with $F(I_+, I_-, K^2) \equiv F(I_-, I_+, K^2)$. The symmetry with respect to exchange of I_+ and I_- suggests that we work with the new variables

$$x = \frac{1}{\sqrt{2}}(I_+ + I_-) \qquad y = \frac{1}{\sqrt{2}}(I_+ - I_-) \tag{4.35}$$

in which case the equation for the stability surface can be written as

$$\begin{aligned} &2(1+R)\left[(1+R) - \Gamma\right]x^2 + \sqrt{2}\left[(1+R)\left(2+K^2\right) - \Gamma\right]x \\ &+2\Gamma(1+R)y^2 + \left(1+K^2\right) = 0. \end{aligned} \tag{4.36}$$

For each value of K^2 Equation (4.36) obviously represents a conic section in the (I_+, I_-)–plane if it represents anything at all. In fact, it is straightforward to show that (4.36) defines a meaningful curve if and only if

$$\Delta = \Gamma - (1+R) > 0 \tag{4.37}$$

in which case the level curves $K^2 = constant$ are hyperbolae of the form

$$z^2 - by^2 = c^2 \tag{4.38}$$

where

$$
\begin{aligned}
z &= x - a \\
a &= \frac{1}{2\sqrt{2}}\left(\frac{(1+K^2)}{\Delta} - \frac{1}{(1+R)}\right) \\
b &= (1+R)\left(\frac{1}{\Delta} + \frac{1}{(1+R)}\right) \\
c &= \frac{1}{2\sqrt{2}}\left(\frac{(1+K^2)}{\Delta} + \frac{1}{(1+R)}\right)
\end{aligned}
\tag{4.39}
$$

with asymptotes given by

$$y = \pm\frac{z}{\sqrt{b}}. \tag{4.40}$$

Equation (4.37) defines a necessary and sufficient condition for the existence of an instability region. Since Δ is periodic in K^2 what we in fact have is a series of surfaces whose cross–sections in the planes $K^2 = \textit{constant}$ are hyperbolae and which are "sandwiched between" (i.e. asymptotic to) the planes $\Delta = 0$. These surfaces are obviously symmetric with respect to the plane $I_+ = I_-$. In the absence of diffusion these surfaces would just be copies of each other, displaced with respect to K^2. Diffusion, however, favours lower wavevectors so that the "lowest–lying" surface is also the one with the lowest threshold.

We imagine that a stability surface is crossed by, for example, fixing one of I_+ or I_- and varying the other. If, say, we increase I_+ sufficiently, keeping I_- constant, then Figure 4.3 shows that we will eventually pass outside the instability region once more: as we would expect, the nonlinearity saturates. From Equation (4.31) the value of I_+ where the stability surface is first crossed, the threshold value I_+^0, is given by the smaller of the two roots of

$$
\begin{aligned}
&(1+R)^2 I_+^2 + \left[(1+R)\left(2 + K^2 + 2(1+R)I_- - 4\Gamma I_-\right) - \Gamma\right] I_+ \\
&+ \left[(1+R)I_-\left(2 + K^2 + (1+R)I_-\right) + (1+K^2) - \Gamma I_-\right] = 0.
\end{aligned}
\tag{4.41}
$$

The value of K^2 which minimises I_+^0 then corresponds to the critical wavevector which determines the pattern scale close to threshold. No explicit expression

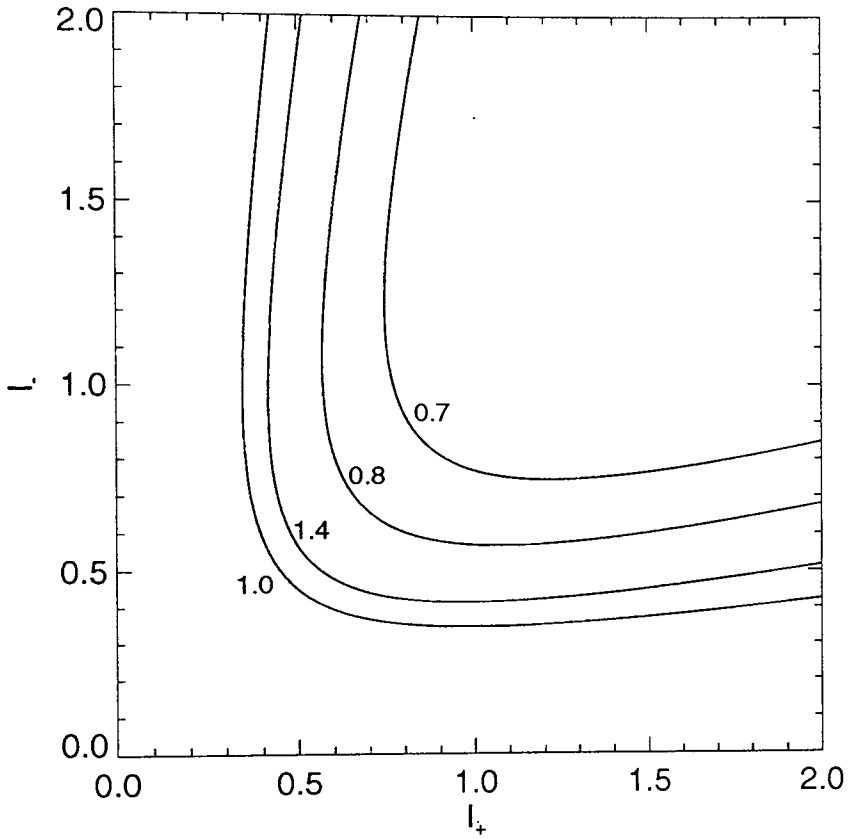

Figure 4.3: *Level curves of the stability surface in the* (I_+, I_-)*-plane for four different values of* K^2*, indicated next to each curve, and* $\sigma = 1$*,* $R = 0.9$ *and* $\kappa = 5$*.*

exists for this value of K^2 and it has to be found numerically from Equation (4.41) in each case.

One question that we can ask is whether it is possible to produce an instability with an input field of only one circular polarisation. This is equivalent to asking whether the asymptotes to any of the hyperbolae which make up the level curves of the stability surface intersect the lines $y = \pm x$ for positive x. That is, with reference to Equations (4.39), we want to know if the line $y = (x-a)/\sqrt{b}$ intersects the line $y = x$ for $x > 0$. Since $b > 1$ always, this will only happen if $a < 0$ which implies

$$\Gamma > (1 + R)(2 + K^2). \tag{4.42}$$

It is possible to satisfy Equation (4.42) with a suitable choice of parameters. It is clear, however, from considering the geometry of the stability surfaces in parameter space that driving with a circularly polarised input field represents the highest threshold in terms of total intensity $(I_+ + I_-)$.

At the other extreme we have that the absolute minimum of each stability surface occurs for $y = 0$ $(I_+ = I_- = I)$. This is the situation which obtains when the input field is plane–polarised and is therefore convenient physically, as well as giving the lowest threshold in terms of total power. We will also see in the next section that this choice of parameters is interesting from the point of view of pattern selection. It is therefore worthwhile to investigate it as a special case.

For $I_+ = I_- = I$ and $\Omega = 0$ Equation (4.31) becomes

$$1 + K^2 = 2I(R\alpha L \sin(\theta) - (1 + R)) \tag{4.43}$$

so that the threshold intensity, I_0, is given by

$$I_0 = \frac{1 + K^2}{2(R\alpha \sin(\theta)L - (1 + R))}. \tag{4.44}$$

The magnitude squared of the critical wavevector, K_c^2, is given by minimising I_0 with respect to K^2 and is therefore the smallest solution of

$$R\alpha L \left[\sin(\sigma K^2) - \sigma(1 + K^2)\cos(\sigma K^2)\right] = (1 + R) \tag{4.45}$$

where

$$\sigma = \frac{\theta}{K^2} = 2\left(\frac{d}{2k'}\cdot\right) \tag{4.46}$$

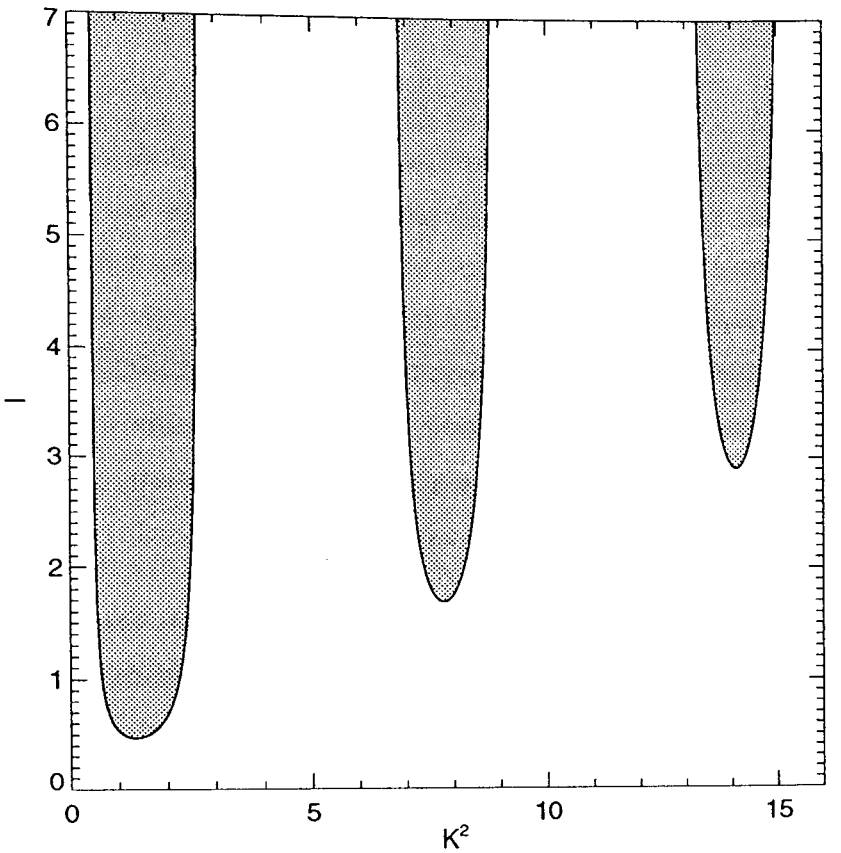

Figure 4.4: *Threshold curves for* $I_+ = I_-$, $\sigma = 1$, $R = 0.9$ *and* $\kappa = 5$. *The shaded parts represent the regions where the homogeneous solution is unstable.*

Again, K_c^2 has to be computed by solving (4.45) numerically. An example of the threshold curves obtained for this case where $I_+ = I_-$ is given in Figure 4.4. These curves represent the intersection of the stability surfaces in (I_+, I_-, K^2)–space with the plane $I_+ = I_-$. Since this plane contains the transverse axis of each of the hyperbolic level curves, the threshold curves in this case are open: the nonlinearity does not saturate.

4.4 Nonlinear Analysis and Numerics

A glance at Equations (4.20) to (4.24) reveals that they have the interesting property that they are invariant under the following discrete transformation:

$$[\sigma_+, \sigma_-, \phi] \rightarrow [\sigma_-, \sigma_+, -\phi]. \tag{4.47}$$

This, by itself, reveals a lot about the expected pattern–forming behaviour of the system. First of all we know that with all other parameters the same $\phi(x, y, t; I_+, I_-)$ and $-\phi(x, y, t; I_-, I_+)$ must both be solutions. In the case where $I_+ = I_- = I$ this means that if ϕ_1 is a solution $-\phi_1$ must be as well. This in turn means that in any expansion in powers of ϕ that we may make, for example in a multiple scales calculation, all even power terms must vanish identically; in particular there will be no quadratic coupling term and so we would not expect the system to form hexagons.

When $I_+ \neq I_-$ quadratic coupling will be present and we may expect hexagons close to threshold, but of what type? Suppose that $(I_+ - I_-) > 0$ and that close to threshold we may make an expansion of the form

$$\partial_t \phi_1 = \mu_1 \phi_1 + \alpha_1 \phi_1^2 + \gamma_1 \phi_1^3 + O(\phi_1^4). \tag{4.48}$$

Now take the corresponding situation where we exchange I_+ and I_- so that $|I_+ - I_-|$ is the same as before but now $(I_+ - I_-) < 0$. Starting from the same initial condition our new solution will be $\phi_2 = -\phi_1$ and will obey

$$\begin{aligned} \partial_t \phi_2 &= \mu_2 \phi_2 + \alpha_2 \phi_2^2 + \gamma_2 \phi_2^3 + O(\phi_2^4) \\ \Rightarrow \partial_t(-\phi_1) &= -\mu_2 \phi_1 + \alpha_2 \phi_1^2 - \gamma_2 \phi_1^3 + O(\phi_1^4). \end{aligned} \tag{4.49}$$

For consistency we must have that $\mu_1 = \mu_2$, $\alpha_1 = -\alpha_2$ and $\gamma_1 = \gamma_2$. From this we can see that changing the sign of $(I_+ - I_-)$ has the effect of changing the sign of the quadratic coupling. For one sign of $(I_+ - I_-)$ we therefore expect that ϕ will form H^+ patterns while for the other sign of $(I_+ - I_-)$ we anticipate H^- patterns. Which sign of pattern goes with which sign of $(I_+ - I_-)$ is something which cannot be determined by this symmetry argument alone but will have to await the derivation of amplitude equations.

We must now ask what effect the different types of hexagonal patterns will have on the optical fields since it is these, after all, which are observable rather than the excitation of the nonlinear medium. Equations (4.20) and (4.21) show that a positive value of ϕ acts to focus σ_+ light while a negative value defocuses it. The opposite is true for σ_- light. This means that if the medium excitation organises itself into an H^+ pattern, the peaks of ϕ will act as focusing lenses for the σ_+ component of the field and this will then form hexagonally co–ordinated intensity peaks: the σ_+ component will take on the same pattern as ϕ. The σ_- component, on the other hand, will see a set of defocusing lenses and so it will have intensity minima at the places where ϕ has its maxima. In contrast to the σ_+ component, the σ_- field will form an H^- pattern. If, instead, ϕ forms an H^- pattern, the σ_+ field will also exhibit this pattern while the σ_- field will exhibit an H^+ structure.

We have deduced quite a lot about the sytem from this simple symmetry argument but to get any further we must do some weakly nonlinear analysis. As a first step we remove the electric field variables from the problem by formal integration of the propagation equations, reducing the system to a single nonlinear P.D.E. for ϕ, the medium excitation:

$$\begin{aligned}\partial_t\phi &= -\left[1+I_+ + RI_+\left|e^{i\sigma\nabla^2-t_R\partial_t}e^{i\kappa\phi}\right|^2 + I_- + RI_-\left|e^{i\sigma\nabla^2-t_R\partial_t}e^{-i\kappa\phi}\right|^2\right]\phi \\ &\quad +\frac{1}{2}\left[I_+ + RI_+\left|e^{i\sigma\nabla^2-t_R\partial_t}e^{i\kappa\phi}\right|^2 - I_- - RI_-\left|e^{i\sigma\nabla^2-t_R\partial_t}e^{-i\kappa\phi}\right|^2\right] \\ &\quad +\nabla^2\phi \qquad (4.50)\end{aligned}$$

where

$$\sigma = 2\left(\frac{d}{2k'}\right), \qquad \kappa = \alpha L. \qquad (4.51)$$

The delay in the system has been included via the formal operator $\exp(-t_R\partial_t)$ so that all of the terms in ϕ on the right hand side of (4.50) are evaluated at the same time. Since the round trip time, t_R, will be on the order of nanoseconds and so orders of magnitude smaller than the time scale of the medium dynamics ($\sim 1\mu$s) it is a reasonable approximation to neglect the delay anyway and so that is what we will do, both in the subsequent analysis and in our numerical

simulations.

Now we write $\phi = \phi_0 + \psi$ where ϕ_0 is the homogeneous solution of (4.50) defined in Equation (4.27), and expand (4.50) in powers of ψ keeping terms up to $O(\psi^3)$. For convenience we also define

$$\hat{\mathcal{L}} = e^{i\sigma\nabla^2}. \tag{4.52}$$

The result of this expansion is

$$\begin{aligned}
\partial_t\psi \;=\; & -\left[1 + I_+ + RI_+\left|\hat{\mathcal{L}}\left(1 + i\kappa\psi - \frac{\kappa^2\psi^2}{2} - \frac{i\kappa^3\psi^3}{6}\right)\right|^2 + \right. \\
& \left. I_- + RI_-\left|\hat{\mathcal{L}}\left(1 - i\kappa\psi - \frac{\kappa^2\psi^2}{2} + \frac{i\kappa^3\psi^3}{6}\right)\right|^2\right](\phi_0 + \psi) \\
& + \frac{1}{2}\left[I_+ + RI_+\left|\hat{\mathcal{L}}\left(1 + i\kappa\psi - \frac{\kappa^2\psi^2}{2} - \frac{i\kappa^3\psi^3}{6}\right)\right|^2 - \right. \\
& \left. I_- - RI_-\left|\hat{\mathcal{L}}\left(1 - i\kappa\psi - \frac{\kappa^2\psi^2}{2} + \frac{i\kappa^3\psi^3}{6}\right)\right|^2\right] \\
& + \nabla^2\psi + O(\psi^4)
\end{aligned} \tag{4.53}$$

or

$$\begin{aligned}
\partial_t\psi \;=\; & -R\phi_0\left\{(I_+ - I_-)\left[i\kappa\left(\hat{\mathcal{L}}\psi\right) - \frac{i\kappa^3}{6}\left(\hat{\mathcal{L}}\psi^3\right) + \frac{i\kappa^3}{2}\left(\hat{\mathcal{L}}\psi^2\right)\left(\hat{\mathcal{L}}^\dagger\psi\right) + H.C.\right] + \right. \\
& \left. (I_+ + I_-)\left[\frac{\kappa^2}{2}\left(\hat{\mathcal{L}}\psi\right)\left(\hat{\mathcal{L}}^\dagger\psi\right) - \frac{\kappa^2}{2}\left(\hat{\mathcal{L}}\psi^2\right) + H.C.\right]\right\} \\
& -\psi\left\{1 + (1+R)(I_+ + I_-) + R(I_+ - I_-)\left[i\kappa\left(\hat{\mathcal{L}}\psi\right) + H.C.\right]\right. \\
& \left. + R(I_+ + I_-)\left[\frac{\kappa^2}{2}\left(\hat{\mathcal{L}}\psi\right)\left(\hat{\mathcal{L}}^\dagger\psi\right) - \frac{\kappa^2}{2}\left(\hat{\mathcal{L}}\psi^2\right) + H.C.\right]\right\} \\
& + \frac{R}{2}\left\{(I_+ + I_-)\left[i\kappa\left(\hat{\mathcal{L}}\psi\right) - i\frac{\kappa^3}{6}\left(\hat{\mathcal{L}}\psi^3\right) + i\frac{\kappa^3}{2}\left(\hat{\mathcal{L}}\psi^2\right)\left(\hat{\mathcal{L}}^\dagger\psi\right) + H.C.\right]\right. \\
& \left. + (I_+ - I_-)\left[\frac{\kappa^2}{2}\left(\hat{\mathcal{L}}\psi\right)\left(\hat{\mathcal{L}}^\dagger\psi\right) - \frac{\kappa^2}{2}\left(\hat{\mathcal{L}}\psi^2\right) + H.C.\right]\right\}
\end{aligned}$$

$$+\nabla^2\psi + O(\psi^4). \tag{4.54}$$

H.C. is used to denote the Hermitian conjugate.

4.4.1 $I_+ = I_-$ (Plane polarised driving field)

Equation (4.54) shows that when $I_+ = I_-$ all terms quadratic in ψ disappear as we deduced from symmetry considerations. As this is potentially the most interesting situation (everywhere else we just expect hexagons) we will examine it first. The techniques we will employ are those used in Chapter 3: amplitude equations and the Lyapunov function formalism. So once more we write

$$\begin{aligned} \psi &= \varepsilon\psi_1 + \varepsilon^2\psi_2 + \varepsilon^3\psi_3 + ... \\ I &= I_0 + \varepsilon I_1 + \varepsilon^2 I_2 + ... \\ \partial_t &= \varepsilon\partial_{T_1} + \varepsilon^2\partial_{T_2} + ... \end{aligned} \tag{4.55}$$

Again we have omitted multiple space scales to avoid unnecessary complications.

We substitute (4.55) into (4.54) and get at $O(\varepsilon)$

$$\left[-1 - K_c^2 - 2(1+R)I_0 + 2I_0 R\kappa \sin\left(\sigma K_c^2\right)\right]\psi_1 = 0 \tag{4.56}$$

assuming that $\nabla^2\psi_1 = -K_c^2\psi_1$. As we showed in Chapter 3 the key to the pattern selection problem in the absence of quadratic coupling lies in the study of the two–mode problem. We therefore write

$$\psi_1 = \frac{1}{2}\left(A\exp(\mathbf{K}_1.\mathbf{x}) + B\exp(\mathbf{K}_2.\mathbf{x}) + c.c.\right) \tag{4.57}$$

with $|\mathbf{K}_1| = |\mathbf{K}_2| = K_c$ and $\mathbf{K}_1.\mathbf{K}_2/K_c^2 = \cos(\vartheta)$.

At $O(\varepsilon^2)$ we have

$$\begin{aligned} \partial_{T_1}\psi_1 &= -\left[1 + 2(1+R)I_0\right]\psi_2 - 2I_1(1+R)\psi_1 \\ &\quad + R\kappa I_0\left[i\hat{\mathcal{L}}\psi_2 - i\hat{\mathcal{L}}^\dagger\psi_2\right] \\ &\quad + R\kappa I_1\left[i\hat{\mathcal{L}}\psi_1 - i\hat{\mathcal{L}}^\dagger\psi_1\right] + \nabla^2\psi_2. \end{aligned} \tag{4.58}$$

Since there are no nonlinear terms at this order ψ_2 need only contain terms at $|\mathbf{K}| = K_c$ which implies that all terms in ψ_2 vanish. The remaining equation in ψ_1 is then

$$\partial_{T_1}\psi_1 = \frac{I_1\left(1+K_c^2\right)}{I_0}\psi_1 \tag{4.59}$$

where we have used the result at $O(\varepsilon)$. If I_1 is non–zero (4.59) implies that on this time scale ψ_1 grows or decays exponentially, depending on the sign of I_1. To obtain a bounded, non–zero solution for ψ_1 our only choice is to set $I_1 = 0$ in which case $\partial_{T_1}\psi_1 \equiv 0$. In fact, when there is no quadratic coupling present we can save some time by omitting I_1 and ∂_{T_1} from the start [41], as this calculation shows.

At $O(\varepsilon^3)$ we get

$$\begin{aligned}
\partial_{T_2}\psi_1 \;=\; & -\left[1+2(1+R)I_0\right]\psi_3 - 2I_2(1+R)\psi_1 \\
& -2RI_0\kappa^2\left[\left(\hat{\mathcal{L}}\psi_1\right)\left(\hat{\mathcal{L}}^\dagger\psi_1\right) - \frac{1}{2}\hat{\mathcal{L}}\left(\psi_1^2\right) - \frac{1}{2}\hat{\mathcal{L}}^\dagger\left(\psi_1^2\right)\right]\psi_1 \\
& -RI_0\kappa^3\left[\frac{i}{6}\hat{\mathcal{L}}\left(\psi_1^3\right) - \frac{i}{2}\left(\hat{\mathcal{L}}\left(\psi_1^2\right)\right)\left(\hat{\mathcal{L}}^\dagger\psi_1\right) - \frac{i}{6}\hat{\mathcal{L}}^\dagger\left(\psi_1^3\right)\right. \\
& \left.+\frac{i}{2}\left(\hat{\mathcal{L}}^\dagger\left(\psi_1^2\right)\right)\left(\hat{\mathcal{L}}\psi_1\right)\right] \\
& +RI_0\kappa\left[i\hat{\mathcal{L}}\psi_3 - i\hat{\mathcal{L}}^\dagger\psi_3\right] + RI_2\kappa\left[i\hat{\mathcal{L}}\psi_1 - i\hat{\mathcal{L}}^\dagger\psi_1\right] + \nabla^2\psi_3.
\end{aligned} \tag{4.60}$$

For terms with $|\mathbf{K}| = K_c$ all terms in ψ_3 vanish. The remaining terms in ψ_1 require a lot of algebra to work out, but after unscaling through the inverse of transformations (4.55) and defining

$$A \to \varepsilon A \qquad B \to \varepsilon B \tag{4.61}$$

the end result is

$$\partial_t A \;=\; \left[2\left(I-I_0\right)\left(R\kappa\sin\left(\sigma K_c^2\right) - (1+R)\right)\right]A$$

$$+RI_0\kappa^2\left[\frac{1}{2}\cos\left(4\sigma K_c^2\right)-\frac{1}{2}+\frac{\kappa}{4}\sin\left(3\sigma K_c^2\right)-\frac{3\kappa}{4}\sin\left(\sigma K_c^2\right)\right]|A|^2A$$

$$+RI_0\kappa^2\left[\cos\left(2\sigma K_c^2\left(1+\cos(\vartheta)\right)\right)-2+\cos\left(2\sigma K_c^2\left(1-\cos(\vartheta)\right)\right)\right.$$

$$+\frac{\kappa}{2}\sin\left(\sigma K_c^2\left(1+2\cos(\vartheta)\right)\right)$$

$$\left.+\frac{\kappa}{2}\sin\left(\sigma K_c^2\left(1-2\cos(\vartheta)\right)\right)-\kappa\sin\left(\sigma K_c^2\right)\right]|B|^2A \tag{4.62}$$

with a corresponding equation for B.

The cross–cubic coefficient, $\gamma(\vartheta)$, is given by

$$\begin{aligned}\gamma(\vartheta) &= RI_0\kappa^2\left[2-\cos\left(2\sigma K_c^2\left(1+\cos(\vartheta)\right)\right)-\cos\left(2\sigma K_c^2\left(1-\cos(\vartheta)\right)\right)\right.\\ &\quad -\frac{\kappa}{2}\sin\left(\sigma K_c^2\left(1+2\cos(\vartheta)\right)\right)-\frac{\kappa}{2}\sin\left(\sigma K_c^2\left(1-2\cos(\vartheta)\right)\right)\\ &\quad \left.+\kappa\sin\left(\sigma K_c^2\right)\right].\end{aligned} \tag{4.63}$$

A comparison with Equation (3.59) shows that, unlike in the case of the two–level ring cavity problem of Chapter 3, here the dependence of γ on ϑ is not trivial. In fact its dependence on the other parameters of the system is not trivial either since K_c^2 is an implicit nonlinear function of R, κ and σ and has to be calculated by solving a transcendental equation. This means that no hard and fast rules can be given about the precise conditions under which different patterns may be found. We will, however, demonstrate that the system has the potential to show both one (rolls) and two (squares) mode patterns.

We first of all recall the definition of the Lyapunov function given in Equation (3.56)

$$\mathcal{G}=-\left[\mu\sum_{i=1}^{N}|A_i|^2-\frac{1}{2}\sum_{\substack{i=1\\ i\neq j}}^{N}\sum_{j=1}^{N}\gamma_{ij}|A_i|^2|A_j|^2-\frac{\zeta}{2}\sum_{i=1}^{N}|A_i|^4\right]. \tag{4.64}$$

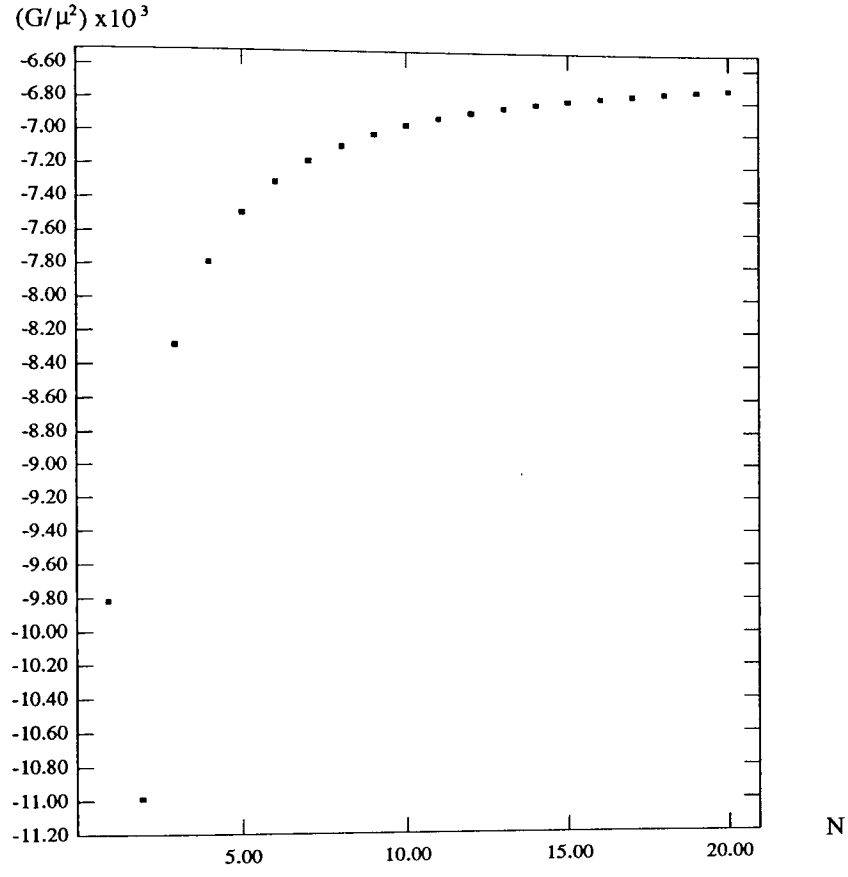

Figure 4.5: *Plot of $\mathcal{G}/\mu^2$ as a function of N, the number of modes for $\kappa = 5$, $\sigma = 1$ and $R = 0.9$ showing that the two–mode pattern minimises $\mathcal{G}$.*

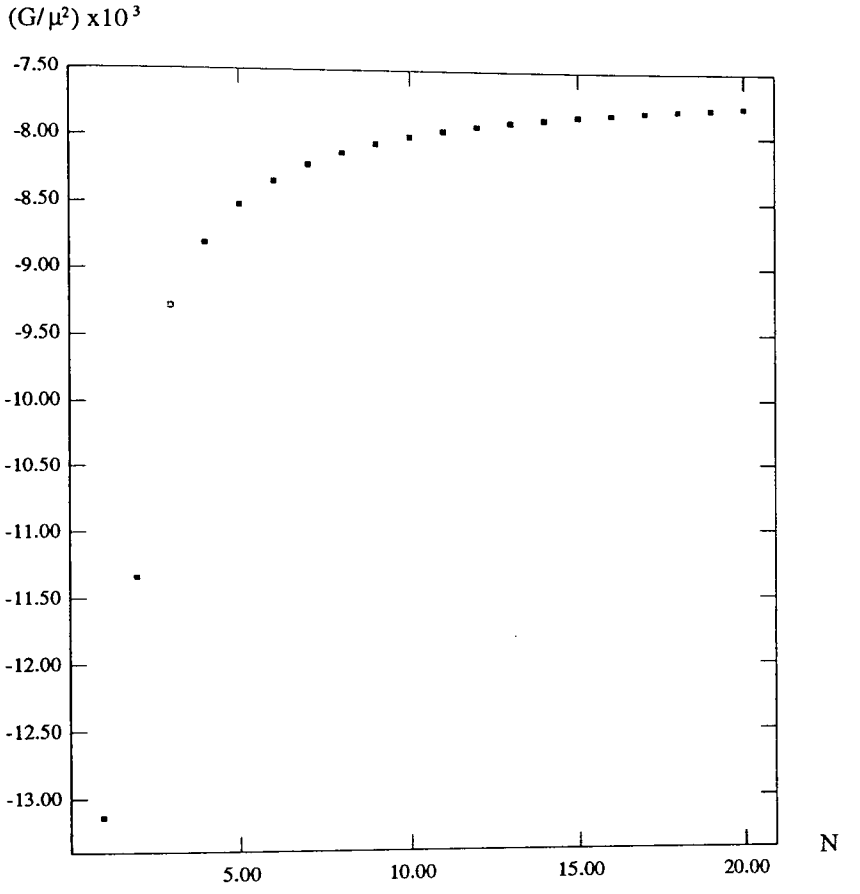

Figure 4.6: *Plot of $\mathcal{G}/\mu^2$ as a function of N, the number of modes for $\kappa = 3$, $\sigma = 1$ and $R = 0.9$ showing that the one-mode pattern minimises $\mathcal{G}$.*

If we pick a set of parameters we can evaluate the steady state value of $\mathcal{G}$ as a function of N for the case of N modes separated by an angle of π/N. One such plot of $\mathcal{G}$ versus N is given in Figure 4.5 showing that for the parameters chosen squares give the lowest value of $\mathcal{G}$ and would therefore be the expected stable pattern. Figure 4.6 is the corresponding plot for a slightly different value of κ, representing for example a different value of detuning. It shows that this time the $N = 1$ pattern (rolls) minimises $\mathcal{G}$ and hence is the most likely to be observed. Note in each case that as $N \rightarrow \infty$, $\mathcal{G}$ tends to a value given by the continuum limit of (4.64).

To verify these assertions we must turn to numerical integration of the model. Our code propagates the optical fields from the ouput face of the nonlinear medium to the mirror and back using a Fast Fourier Transform [47], while a finite difference Hopscotch method (Appendix A) is used to integrate the material equation (4.22). As in the nonlinear analysis we neglect the delay introduced by the roundtrip time of the fields. We use a square periodic domain of typically 128x128 grid points and filtered noise as the initial condition.

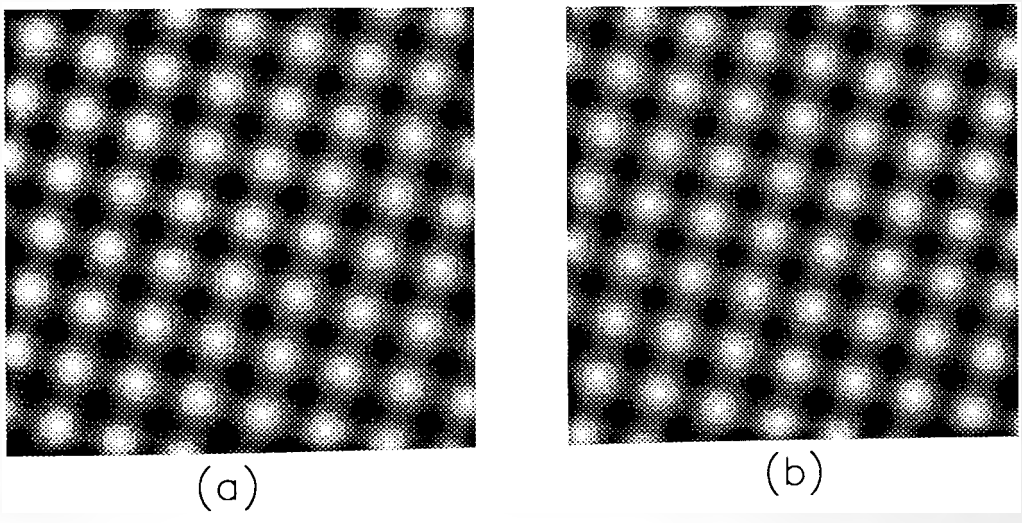

Figure 4.7: *The asymptotic states reached by the backward fields for* $I_+ = I_- = 0.53$ *(12 % above threshold),* $\kappa = 5$, $\sigma = 1$ *and* $R = 0.9$*: (a) the* σ_+ *field, (b) the* σ_- *field.*

Our simulations verify the values of I_0, the threshold pump intensity, and K_c given

by the linear analysis of Section 4.3. Figure 4.7 shows that when we integrate the equations for the parameter values corresponding to Figure 4.5 we do indeed get a square pattern in the ouput fields. Notice that the patterns in the left and right circularly polarised components are displaced with respect to each other. This is consistent with the idea that the focusing and defocusing properties of the medium are reversed for σ_+ and σ_- light: for a square pattern a sign reversal is equivalent to a translation.

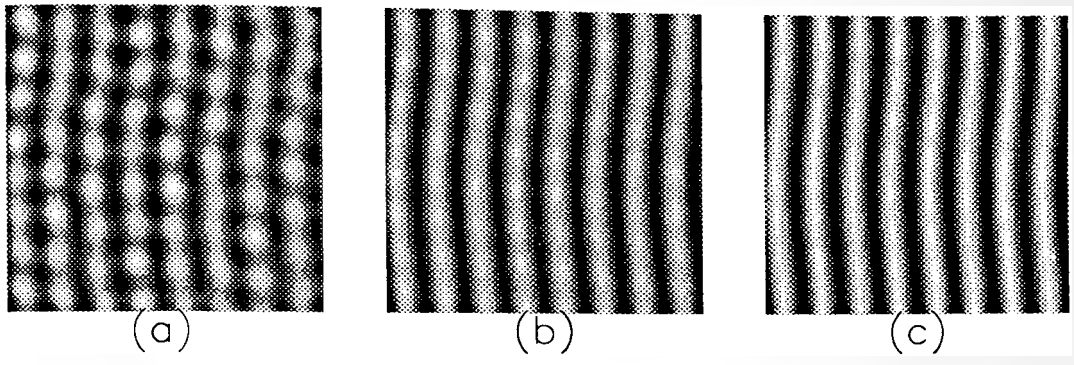

Figure 4.8: *Time sequence showing the formation of rolls in the intensity of the σ_+ component of the field $I_+ = I_- = 1.65$ (5 % above threshold), $\kappa = 3$, $\sigma = 1$ and $R = 0.9$. (a) t=40, (b) t=80, (c) t=120.*

If we change the value of κ so that our parameter values coincide with those of Figure 4.6, we get a roll pattern instead as Figure 4.8 shows. Once again (although it is not shown) the patterns in the σ_+ and σ_- components are displaced. It is also interesting to note that the system seems to go through a transient square pattern before settling down to the roll solution.

The above numerical results confirm our analytical predictions. As a quantitative comparative test of the two–mode amplitude equations and the numerical code we plot in Figure 4.9 the amplitude of a set of stable squares as a function of the degree above threshold. It can be seen that the agreement is quite good, increasing our confidence in both the numerics and the analysis.

Since it is possible to observe a two–mode pattern where the wavevectors of the modes are orthogonal, we could ask whether we can expect to find other two–mode patterns: in other words, rhomboids. This question can be answered using

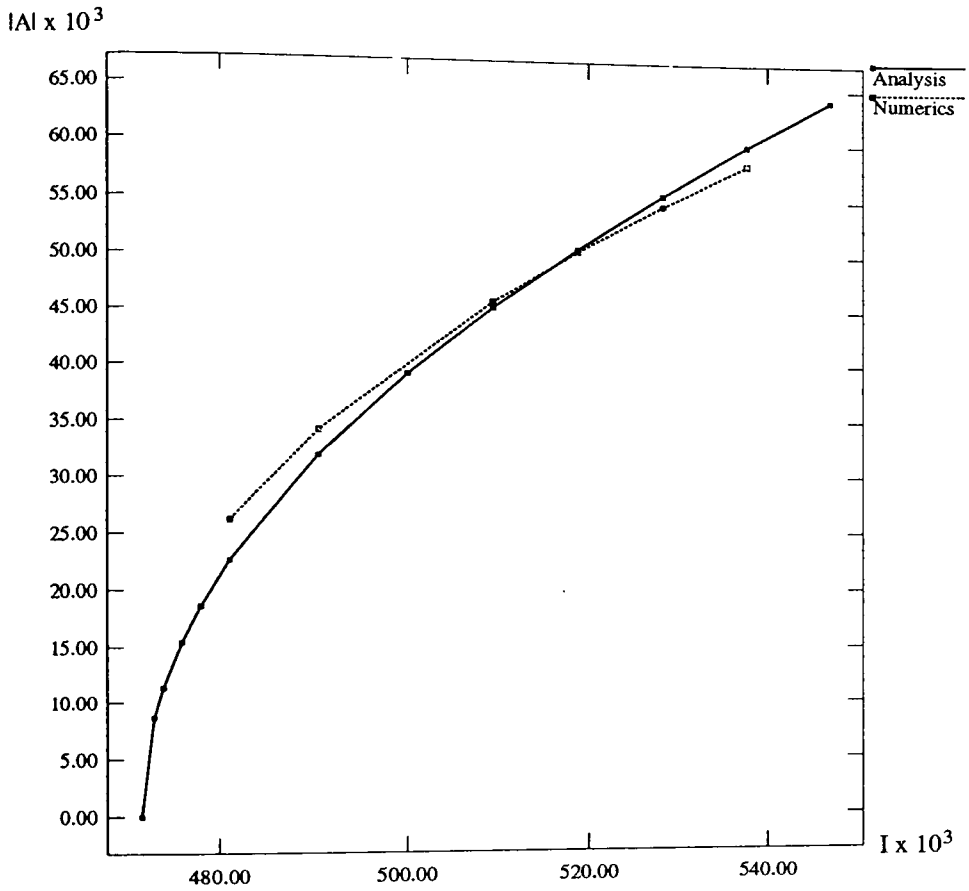

Figure 4.9: *Comparison between numerical and analytic values of the square amplitude as a function of I for $\kappa = 5$, $\sigma = 1$ and $R = 0.9$.*

Equation (4.63).

We restrict ourselves to the two–mode case and write the Lyapunov function as a function of γ which in turn is a function of the angle, ϑ, between the wavevectors of the two modes:

$$\mathcal{G}(two\ \ modes) = -\frac{\mu^2}{\zeta + \gamma(\vartheta)}. \tag{4.65}$$

At the same time, the value of $\mathcal{G}$ for a roll pattern is given by

$$\mathcal{G}(roll) = -\frac{\mu^2}{2\zeta}. \tag{4.66}$$

The first question to be answered is whether we can expect a two–mode pattern at all: that is, whether rolls give a lower value of $\mathcal{G}$ than any pattern characterised by two wavevectors. We see that rolls are stable with respect to rhomboids iff $\gamma(\vartheta) > \zeta$, $\forall\ \vartheta\ \epsilon\ [0, 2\pi)$. If, however, there exist ranges of values of ϑ such that $\zeta > \gamma(\vartheta)$ then two–mode patterns corresponding to values of ϑ in those ranges will be stable with respect to rolls. Furthermore, the value of ϑ which minimises γ also minimises $\mathcal{G}$.

From Equation (4.63) the conditions which identify stationary points of $\gamma(\vartheta)$ are

$$\sin(\vartheta) = 0 \quad \text{or} \quad 2\sigma K_c^2 \cos(\vartheta) = n\pi. \tag{4.67}$$

Equations (4.44) and (4.45) show that for $\kappa > 0$ (focusing) $\pi/2 > \sigma K_c^2 > 0$ and $\sigma K_c^2 \to \pi/2^-$ as $\sigma \to \infty$; while for $\kappa < 0$ (defocusing) $3\pi/2 > \sigma K_c^2 > \pi/2$ and $\sigma K_c^2 \to 3\pi/2^-$ as $\sigma \to \infty$; in both cases we must have that $|\kappa| > 2$. This means that the extrema defined by $\sin(\vartheta) = 0$ are local maxima of γ while the others are local minima for n even and local maxima for n odd. It also means that for $\kappa > 0$ the second condition, $2\sigma K_c^2 \cos(\vartheta) = n\pi$, can only be satisfied for $n = 0$ (squares) and the stationary points defined in this way are minima (Figure 4.10). For $\kappa < 0$, on the other hand, extrema *may* be found for $n = 0, \pm 2$ (minima) and $n = \pm 1$ (maxima). The values of ϑ corresponding to $n = \pm 2$ can in principle yield rhomboidal patterns which are not square; but since $n = 0$ and $n = \pm 2$ give the same value for $\mathcal{G}$, the one that is observed will depend on which basin of attraction the initial condition lies in (Figure 4.11).

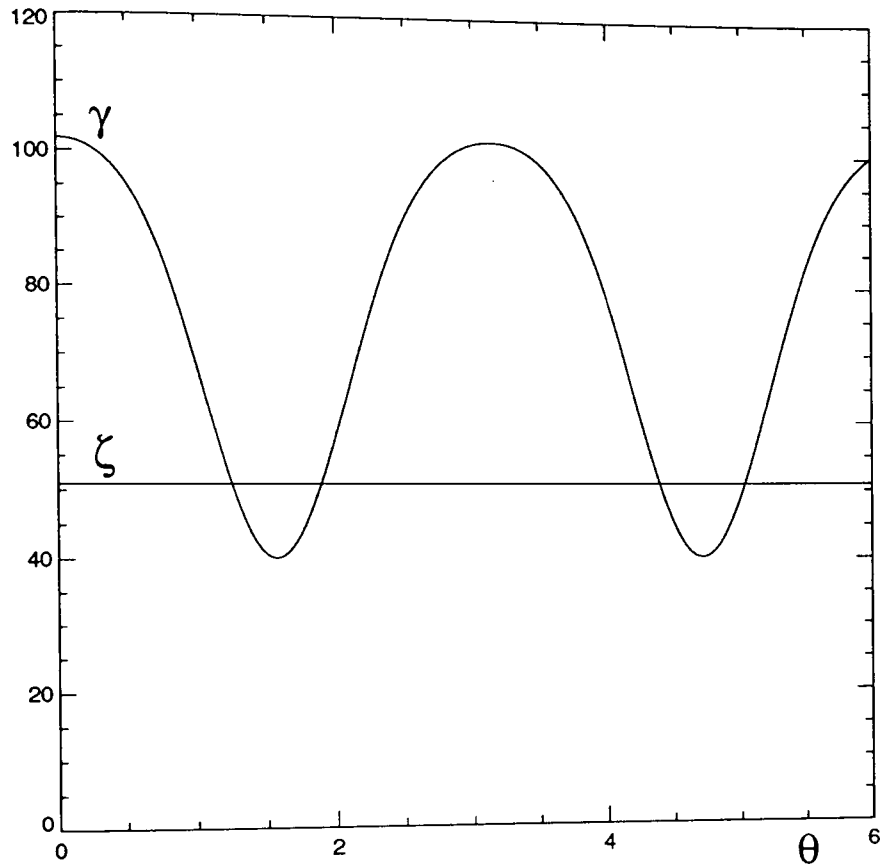

Figure 4.10: *Plot of both γ, the cross–cubic coefficient, and ζ, the self–cubic coefficient, as functions of the angle ϑ in radians for $\kappa = 5$, $\sigma = 1$ and $R = 0.9$.*

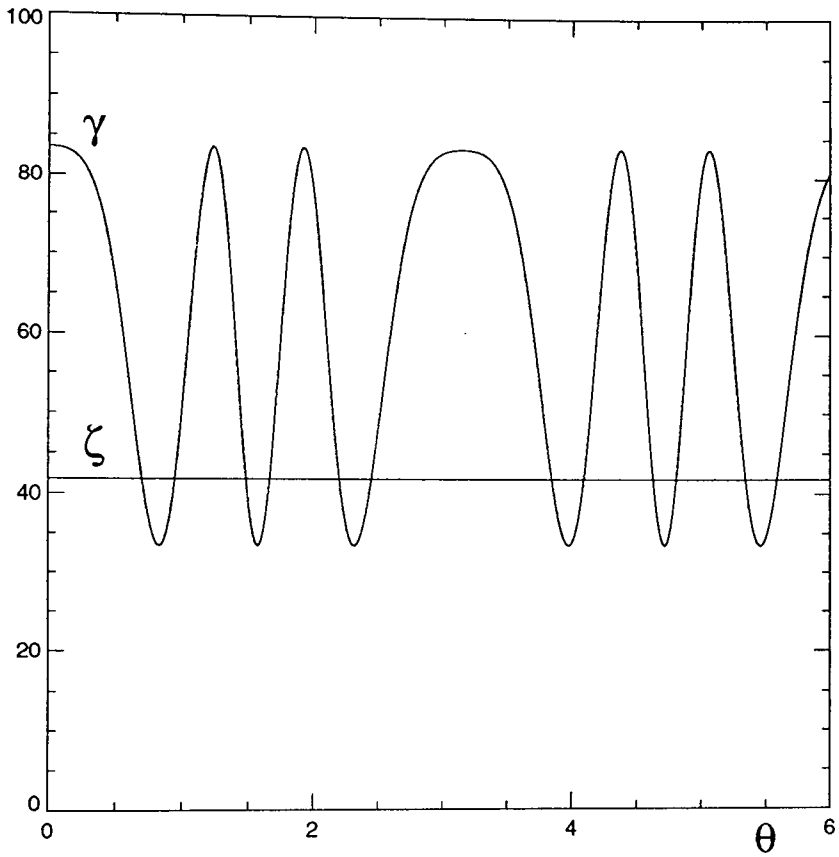

Figure 4.11: *Plot of both γ, the cross-cubic coefficient, and ζ, the self-cubic coefficient, as functions of the angle ϑ in radians for $\kappa = -5$, $\sigma = 5$ and $R = 0.9$.*

We can check this hypothesis for the parameters corresponding to Figure 4.11 for which we predict that there is a stable square solution and one consisting of rhomboids corresponding to an angle of about 48 degrees between the two wavevectors. When we run the simulations with a square grid and square periodic domain we find that the system always selects the square pattern. When the system of equations is integrated on a non–orthogonal grid (one whose lattice points lie at the vertices of a set of parallelograms rather than a set of squares) it is found that the system can instead select the rhomboidal pattern. This indicates that the square grid may introduce a slight bias in the pattern selection process which favours the square pattern over the rhomboids. This is most likely to be an effect of the boundary conditions since the square pattern produced is not always aligned with the grid. It does give an example, however, of how computational parameters can influence the evolution of a dynamical system.

4.4.2 $I_+ \neq I_-$

Now we tackle the more general situation where $I_+ \neq I_-$. Equation (4.54) shows that in that case we have quadratic coupling and so we will perform our multiple scales analysis based on a lowest order solution which consists of a hexagon. It is just a matter of grinding through the by now familiar procedure and seeing what comes out the other end.

We define

$$\beta_+ = (I_+ + I_-)\,, \qquad \beta_- = (I_+ - I_-) \tag{4.68}$$

and expand in the following way

$$\begin{aligned} \psi &= \varepsilon\psi_1 + \varepsilon^2\psi_2 + \varepsilon^3\psi_3 + \cdots \\ \beta_+ &= \beta_{+0} + \varepsilon\beta_{+1} + \varepsilon^2\beta_{+2} + \cdots \\ \beta_- &= \beta_{-0} + \varepsilon\beta_{-1} + \varepsilon^2\beta_{-2} + \cdots \\ \partial_t &= \varepsilon\partial_{T_1} + \varepsilon^2\partial_{T_2} + \cdots \end{aligned} \tag{4.69}$$

We must also remember that ϕ_0, the homogeneous solution, depends on β_+ and β_- and must therefore be expanded in powers of ε as well:

$$\phi_0 = f_0 + \varepsilon f_1 + \varepsilon^2 f_2 + ... \tag{4.70}$$

Now we just write

$$\psi_1 = \frac{1}{2}\left(A\exp(\mathbf{K_1}.\mathbf{x}) + B\exp(\mathbf{K_2}.\mathbf{x}) + C\exp(\mathbf{K_3}.\mathbf{x}) + c.c.\right) \tag{4.71}$$

with $\mathbf{K_1} + \mathbf{K_2} + \mathbf{K_3} = 0$, and substitute all these expansions into (4.54) solving at each order in ε. After completing the calculation up to $O(\varepsilon^3)$ and unscaling in the usual way we get a set of equations for A, B and C of the form

$$\partial_t A = \mu A + \alpha B^* C^* - \zeta|A|^2 A - \gamma(|B|^2 + |C|^2)A \tag{4.72}$$

with

$$\mu = \left\{R\kappa\sin\left(\sigma K_c^2\right)\left[(\beta_+ - \beta_{+0}) - 2\left(\beta_-\phi_0 - \beta_{-0}f_0\right)\right] - (1+R)\left[\beta_+ - \beta_{+0}\right]\right\}$$

$$\alpha = R\kappa\beta_-\left\{\frac{\kappa}{2}\left(1-\cos\left(\sigma K_c^2\right)\right)\left(\frac{1}{1+(1+R)\beta_+}\right) - 2\sin\left(\sigma K_c^2\right)\right\}$$

$$\begin{aligned}\zeta = -R\kappa\Bigg\{&\frac{\kappa^2}{4}\left(f_0\beta_{-0} - \frac{\beta_{+0}}{2}\right)\left(3\sin\left(\sigma K_c^2\right) - \sin\left(3\sigma K_c^2\right)\right)\\ &+\frac{\kappa\Lambda(4)}{4}\left(f_0\beta_{+0} - \frac{\beta_{-0}}{2}\right)\left(\cos\left(3\sigma K_c^2\right) - \cos\left(\sigma K_c^2\right)\right)\\ &-\frac{\beta_{-0}}{4}\left(\sin\left(\sigma K_c^2\right)\left(2\Lambda(0)+\Lambda(4)\right) + \Lambda(4)\sin\left(4\sigma K_c^2\right)\right)\\ &-\frac{\kappa\beta_{+0}}{4}\left(1-\cos\left(4\sigma K_c^2\right)\right)\Bigg\}\end{aligned}$$

$$\begin{aligned}\gamma = -R\kappa\Bigg\{&\frac{\kappa^2}{2}\left(f_0\beta_{-0} - \frac{\beta_{+0}}{2}\right)\left(2\sin\left(\sigma K_c^2\right) - \sin\left(2\sigma K_c^2\right)\right)\\ &-\frac{\kappa\Lambda(3)}{2}\left(f_0\beta_{+0} - \frac{\beta_{-0}}{2}\right)\left(\cos\left(2\sigma K_c^2\right) - \cos\left(\sigma K_c^2\right)\right)\end{aligned}$$

$$-\frac{\beta_{-0}}{2}\left((\Lambda(0)+\Lambda(3))\sin\left(\sigma K_c^2\right)+\Lambda(3)\sin\left(3\sigma K_c^2\right)\right)$$

$$-\frac{\kappa\beta_{+0}}{2}\left(2-\cos\left(\sigma K_c^2\right)-\cos\left(3\sigma K_c^2\right)\right)\Bigg\} \tag{4.73}$$

and

$$\Lambda(n) = \frac{R\kappa^2\left(1-\cos\left(n\sigma K_c^2\right)\right)\left(\beta_{-0}-2\beta_{+0}f_0\right)-4R\kappa\beta_{-0}\sin\left(\sigma K_c^2\right)}{1+nK_c^2+(1+R)\beta_{+0}-R\kappa\sin\left(n\sigma K_c^2\right)\left(\beta_{+0}-f_0\beta_{-0}\right)}. \tag{4.74}$$

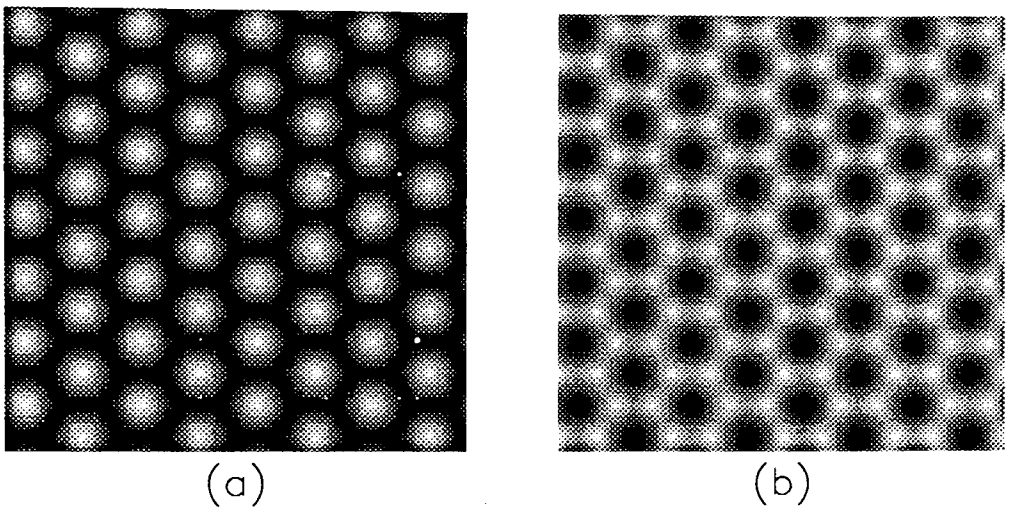

Figure 4.12: *The asymptotic states reached by the backward fields for* $I_+ = 0.57$, $I_- = 3$, $\kappa = 5$, $\sigma = 1$ *and* $R = 0.9$ *(*$K_c^2 = 1.21$*): (a) the* σ_+ *field, (b) the* σ_- *field.*

The coefficients in the amplitude equations are quite complicated. The one important point, however, is that the quadratic coefficient, α, is proportional to $\beta_- = (I_+ - I_-)$ so that a change of sign of β_- implies a change of sign of α. While we can make no firm statement about the sign of the term multiplying β_- we can at least determine it for a given set of parameters. For example, Figure 4.12 shows the asymptotic states reached by the σ_+ and σ_- components of the field for a set of parameters which give $\alpha > 0$. In this case we predict that the medium excitation, ϕ, forms an H^+ pattern and, by the argument of Section 4.4, so does the σ_+ field, while the σ_- field forms H^-. Figure 4.12 indicates that this

is so. If the simulation is run with the opposite sign of β_-, but all other parameters the same, we find that the patterns in the circularly polarised components of the electric field switch: H^- for σ_+ and H^+ for σ_-.

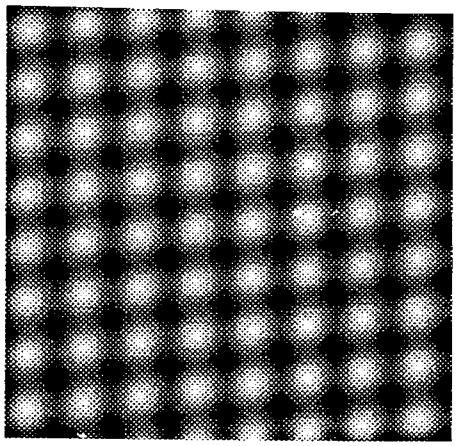

Figure 4.13: *The asymptotic states reached by the backward σ_+ field for $I_+ = 0.65$, $I_- = 0.53$, $\kappa = 5$, $\sigma = 1$ and $R = 0.9$.*

We also note that when $|I_+ - I_-|$ is small, we get either distorted squares (rhomboids) or rolls, depending on whether squares or rolls are the preferred pattern when $I_+ = I_-$. The distorted squares (Figure 4.13) are a sort of intermediate state between the pure squares and the hexagons.

A final interesting implication of the antisymmetry in α with respect to exchange of I_+ and I_- is that if the system is driven with a single circularly polarised input field, the observed pattern will be independent of whether the field is σ_+ or σ_-. This has been confirmed numerically. If energy is put into only one component of the field, the other component will be zero at all times since the only effect of the medium is to provide a phase modulation and there is therefore no mechanism for the transfer of energy. This means that in some sense this situation is like a saturable version of the Kerr slice with feedback mirror [24, 25]. As stated in Section 4.3, however, driving with a circularly polarised field gives the highest threshold in terms of total power and is therefore the most inefficient way, in this system, of generating a pattern–forming instability.

4.5 Addition of Quarter–Wave plate

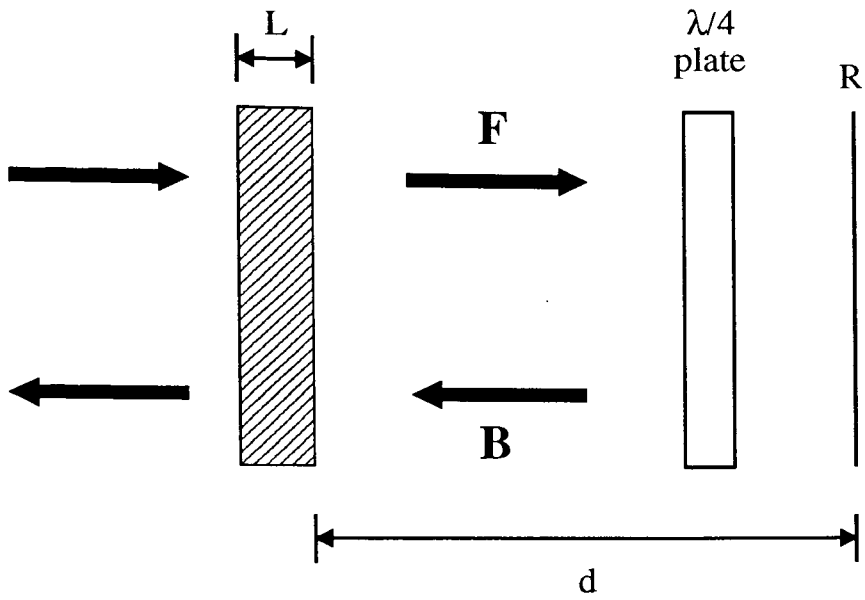

Figure 4.14: *Sketch of the feedback mirror configuration with a quarter–wave plate present.*

In the system we have been studying, the only effect of the feedback mirror, apart from reducing the energy in the field, is to reverse the direction of propagation of the field so that each circularly polarised field component interacts with the same medium transition on its way back from the mirror as it did on its way to the mirror. As we have seen, the system can then be described by the self–contained equation for ϕ

$$\begin{aligned}\partial_t\phi &= -\left[1 + I_+ + RI_+\left|e^{i\sigma\nabla^2 - t_R\partial_t}e^{i\kappa\phi}\right|^2 + I_- + RI_-\left|e^{i\sigma\nabla^2 - t_R\partial_t}e^{-i\kappa\phi}\right|^2\right]\phi \\ &\quad + \frac{1}{2}\left[I_+ + RI_+\left|e^{i\sigma\nabla^2 - t_R\partial_t}e^{i\kappa\phi}\right|^2 - I_- - RI_-\left|e^{i\sigma\nabla^2 - t_R\partial_t}e^{-i\kappa\phi}\right|^2\right] \\ &\quad + \nabla^2\phi. \end{aligned} \tag{4.75}$$

If we were to put a $\lambda/4$ plate in front of the feedback mirror (Figure 4.14) then the longitudinal boundary condition would be instead

$$B_\pm(z = d) = rF_\mp(z = d) \tag{4.76}$$

and the corresponding equation for ϕ would read

$$\begin{aligned}\partial_t\phi &= -\left[1+I_+ + RI_+\left|e^{i\sigma\nabla^2 - t_R\partial_t}e^{i\kappa\phi}\right|^2 + I_- + RI_-\left|e^{i\sigma\nabla^2 - t_R\partial_t}e^{-i\kappa\phi}\right|^2\right]\phi \\ &\quad +\frac{1}{2}\left[I_+ + RI_-\left|e^{i\sigma\nabla^2 - t_R\partial_t}e^{-i\kappa\phi}\right|^2 - I_- - RI_+\left|e^{i\sigma\nabla^2 - t_R\partial_t}e^{i\kappa\phi}\right|^2\right] \\ &\quad +\nabla^2\phi. \qquad (4.77)\end{aligned}$$

A comparison of Equations (4.75) and (4.77) shows that in general there is no transformation of parameters or variables which will take one into the other. In the special case when the pump field is plane–polarised, however, there is such a transformation, namely $\kappa \to -\kappa$: that is, putting in the $\lambda/4$ plate is equivalent to changing the sign of the detuning. Since for $\kappa > 0$, $0 < \sigma K_c^2 < \pi/2$ while for $\kappa < 0$, $\pi/2 < \sigma K_c^2 < 3\pi/2$, the addition of the quarter–wave plate should produce a change in the length scale of the pattern. This is an effect which should be experimentally verifiable.

4.6 Conclusion

In this chapter we examined a feedback mirror system where the nonlinear medium was an alkali vapour driven by an external field with two orthogonally polarised components. We found that the patterns formed by the system could be predicted by a combination of an argument based on a simple symmetry of the model equations and a multiple scales analysis. The analytical predictions were borne out by numerical simulations. In particular, we found that the system could form stable squares, rolls and rhomboids, as well as both types of hexagon. Finally, we predict that a simple modification of the system should lead to an experimentally observable change in the length scale of the pattern under conditions of a plane–polarised driving field.

Chapter 5

Localised States in the Two Level Ring Cavity

5.1 Introduction

In the previous two chapters we have examined, both analytically and numerically, the near–threshold pattern forming behaviour of two nonlinear optical systems. In this chapter we will point out a further type of behaviour which may exist in such systems below the modulational instability threshold. As well as being of intrinsic interest as are the previous phenomena studied, the structures which we are going to look at here may have the possibility of being used in applications, albeit quite a long time in the future.

The basic idea is that if we have a system where there are two dynamically stable fixed points then there is a possibility that there may also exist solutions which connect these fixed points. This is an idea which has been explored, for example, in the context of complex Ginzburg–Landau equations [1,48,49] where such solutions correspond in one dimension to kinks or anti–kinks. In the systems we have been looking at a coexistence of stable solutions can be found below the bifurcation point when there is a subcritical bifurcation, either to a roll solution

in one dimension or to a hexagon solution in two dimensions.

The solutions which we specifically refer to as localised states connect a homogeneous solution of the system to one which corresponds to a pattern. What this amounts to is that we may produce a localised region of the pattern solution embedded in a background of the homogeneous solution. Such solutions have already been found in several areas, including optics [50]. In fact, the existence of solitary–wave structures in one–dimensional cavity models was already demonstrated in the early eighties by Moloney and co–workers [3], while the possibility of creating such structures using address pulses in a 1D optical memory was investigated by McDonald and Firth [5].

Since we wish to study this phenomenon in the context of one of the optical systems which we have dealt with previously, we choose the two–level ring cavity system of Chapter 3 and for simplicity we restrict ourselves to the purely absorptive ($\Delta = 0$) case.

In two transverse dimensions an isolated peak of a hexagonal pattern suggests itself as a potential optical "bit" for the storage of information. If, for example, we can control the position of such 2D localised states as well as being able to create and destroy them, we have the basis of an optical memory. We turn our attention to these issues at the end of the chapter after we have made some sort of preliminary investigation of localised states in both one and two transverse dimensions.

5.2 Localised States in 1D

Localised states are more easily visualised in one spatial dimension than in two and so that is where we begin. We recall that the model which we are using is

$$\partial_t E = -E\left[(1+i\theta) + \frac{2C(1-i\Delta)}{|E|^2+1+\Delta^2}\right] + E_I + ia\nabla^2 E \tag{5.1}$$

with $\Delta = 0$. A stable localised state (L.S.), that is one which is time–independent, can be described in terms of the four–dimensional dynamical system that we get when we take Equation (5.1) and set $\partial_t E = 0$. It is more convenient to discuss things, though, in terms of the equation for A where $E = E_s(1 + A)$, since then the fixed point corresponding to the homogeneous solution lies at the origin. We therefore write

$$\partial_t A = -(1 + i\theta)A + ai\nabla^2 A - \frac{2C(1 + A)}{1 + I(1 + A + A^* + |A|^2)} + \frac{2C}{1 + I} \tag{5.2}$$

where we have set $\Delta = 0$. After setting $\partial_t A = 0$ the remaining problem can then be written as the following "dynamical system" in x

$$\begin{aligned}
\frac{dU}{dx} &= \theta R + S + \frac{2CS}{1 + I\,(1 + 2R + R^2 + S^2)} \\
\frac{dR}{dx} &= U \\
\frac{dV}{dx} &= \theta S - R + \frac{2C(1 + R)}{1 + I\,(1 + 2R + R^2 + S^2)} + \frac{2C}{1 + I} \\
\frac{dS}{dx} &= V
\end{aligned} \tag{5.3}$$

where R and S are the real and imaginary parts of A respectively and $I = |E_s|^2$ as in Chapter 3. We also set $a = 1$ since it can always be scaled away by a suitable rescaling of the transverse variables. We can think of time–independent solutions to the full P.D.E. as fixed points or orbits in the four–dimensional phase space of the variables (U, R, V, S). Thus the homogeneous solution corresponds to a fixed point at the origin while the roll solution is a limit cycle. A localised state, which approaches the plane–wave fixed point as $x \to -\infty$, passes "near" the roll solution and then returns to the fixed point as $x \to \infty$ is then a homoclinic orbit [51].

From the above argument one necessary condition for the existence of localised states is that the origin have both an unstable manifold along which the homoclinic orbit leaves the origin and a stable manifold along which the homoclinic orbit approaches the origin [51]. We can, in fact, determine the nature of the origin by a linear stability analysis (one of the few things which we can do analytically). This is most easily done in terms of the variables A, A^*, $d_x A = \dot{A}$ and

$d_x A^* = \dot{A}^*$ rather than U, R, V and S although the result is obviously the same. Then when we linearise around the origin we get

$$\frac{d}{dx}\begin{bmatrix} \delta\dot{A} \\ \delta A \\ \delta\dot{A}^* \\ \delta A^* \end{bmatrix} = \begin{bmatrix} 0 & 1 & 0 & 0 \\ \theta - i - \frac{2Ci}{(1+I)^2} & 0 & \frac{2CIi}{(1+I)^2} & 0 \\ 0 & 0 & 0 & 1 \\ -\frac{2CIi}{(1+I)^2} & 0 & \theta + i + \frac{2Ci}{(1+I)^2} & 0 \end{bmatrix} \begin{bmatrix} \delta\dot{A} \\ \delta A \\ \delta\dot{A}^* \\ \delta A^* \end{bmatrix}. \tag{5.4}$$

The eigenvalues of the stability matrix are given by

$$\lambda^2 = \theta \pm \sqrt{\left(\frac{2CI}{(1+I)^2}\right)^2 - \left(1 + \frac{2C}{(1+I)^2}\right)^2}. \tag{5.5}$$

Below the modulational instability threshold of the full P.D.E., which is a necessary condition for the dynamic stability of the plane–wave fixed point, and hence of the localised state, the quantity under the square root sign in Equation (5.5) is negative and λ^2 can therefore be written as

$$\lambda^2 = \theta \pm i\alpha \tag{5.6}$$

where α is real and positive. The four eigenvalues then take the form

$$\lambda = \begin{cases} \gamma \pm iK \\ -\gamma \pm iK \end{cases}$$

with

$$K^2 = \gamma^2 + K_c^2 > K_c^2, \quad 2\gamma K = \pm\alpha. \tag{5.7}$$

From this it is obvious that the origin is always a fixed point with two stable directions and two unstable directions.

Of course the other thing we must do is identify where a subcritical roll solution exists and we can do that analytically using the amplitude equations which were derived in Chapter 3. All we have to do is find regions where the self–cubic coefficient becomes negative. For the parameter values we concentrated on in Chapter 3 ($\Delta = 0$, $\theta = -1$) and which we will also use here, the bifurcation to the roll solution is supercritical for $I \in (2.143..., 4.167...)$ and subcritical elsewhere.

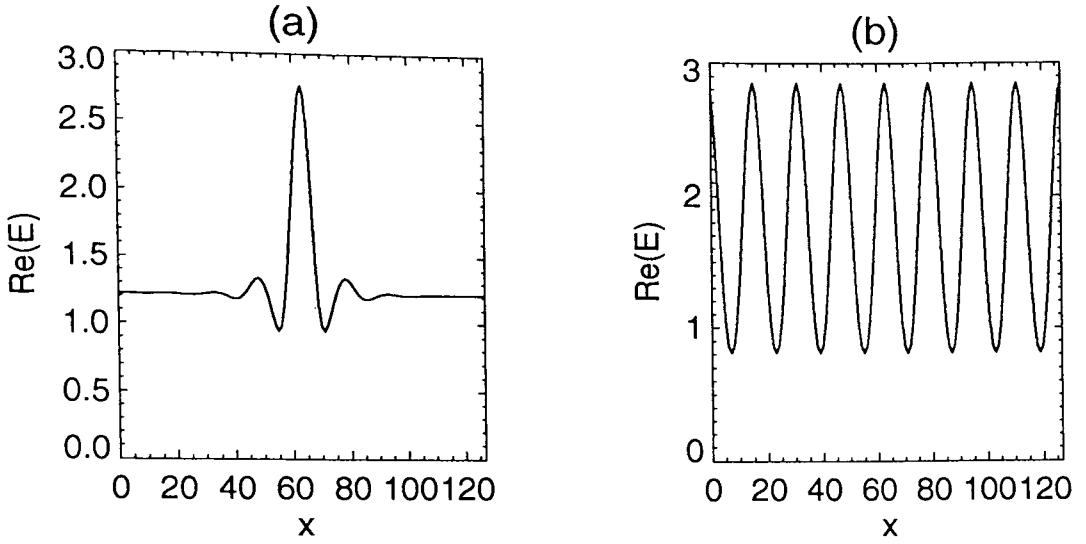

Figure 5.1: *Re(E) plotted as a function of the transverse co-ordinate x for (a) the 1D localised state and (b) the stable roll solution.* $\Delta = 0$, $\theta = -1$, $I = 1.53$ *and* $C = 5.1$

We have identified two of the necessary conditions for the existence of localised states. To actually look at these structures and examine their dynamical stability we turn to numerical integration of Equation (5.1). The L.S. is initialised by using an initial condition which is a narrow pulse (for example, a gaussian) of a height comparable to the amplitude of the subcritical roll and a width of about one wavelength of the roll pattern. An example of an L.S. is shown in Figure 5.1 together with a plot of the corresponding roll solution for comparison. The similarity between the L.S. and a single "peak" of the roll is evident. A better comparison between the L.S. and the roll can be obtained by plotting $Im(E)$ against $Re(E)$ for both on the same diagram. This is done in Figure 5.2 which shows that the L.S. follows the roll solution closely until it goes off to the homogeneous solution for large x. It should be noted that there is no overall phase change accumulated in going across a localised state so that, while they can be classed as defects, they do not appear to be topological, a fact already suggested by the phenomenology of their creation.

We find that the L.S. is not stable in time at all points where the subcritical roll solution exists. There is a dynamic stability threshold above which the presence of a pulse of sufficient amplitude causes the whole field to switch up to the roll

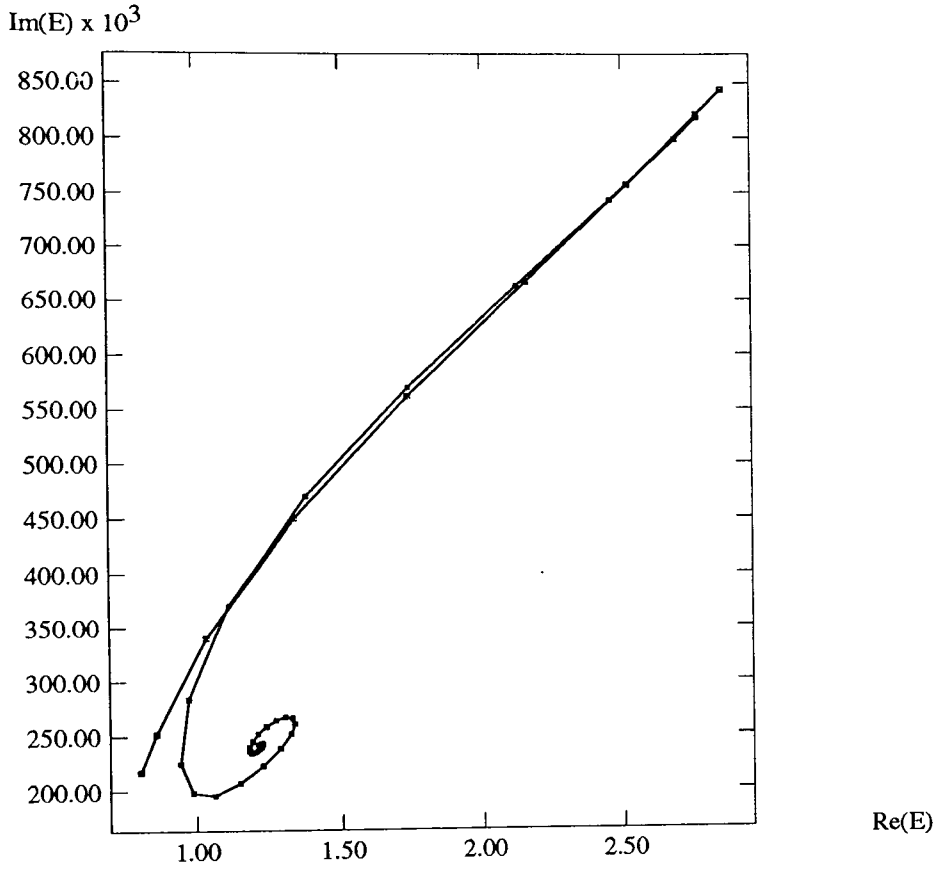

Figure 5.2: *$Im(E)$ plotted against $Re(E)$ for both the 1D localised state and the stable roll solution. The localised state spirals out from the plane-wave fixed point, tracks the roll solution and then spirals back in to the fixed point.* $\Delta = 0$, $\theta = -1$, $I = 1.53$ *and* $C = 5.1$

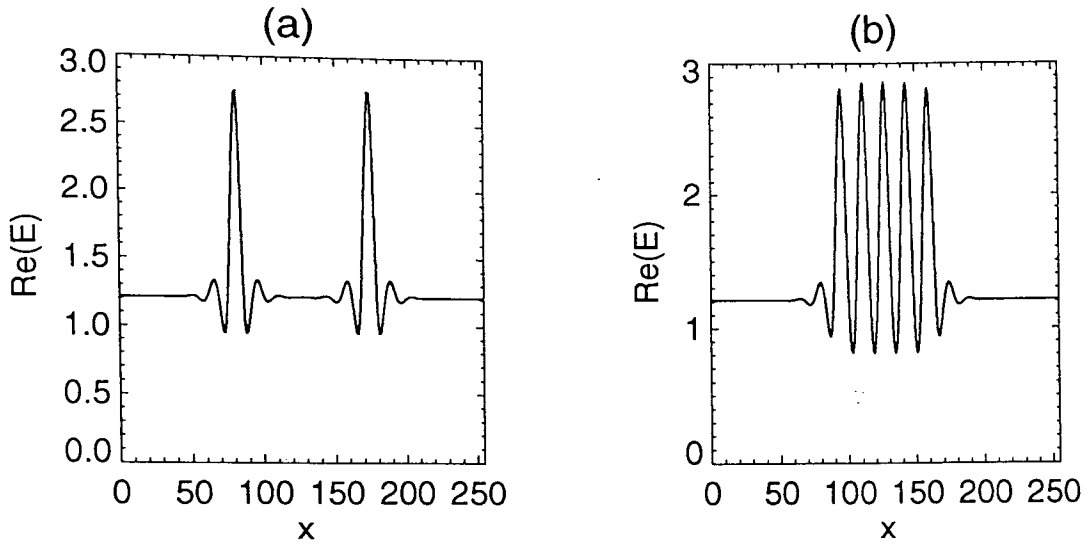

Figure 5.3: *Re(E) plotted as a function of the transverse co-ordinate x for (a) two isolated localised states and (b) a multiple-peaked localised state. In both cases the initial condition was a gaussian of F.W.H.M. (full width at half-maximum) equal to 30 space steps but for (a) the peak amplitude of the gaussian was 50 units while for (b) it was 10 units.* $\Delta = 0$, $\theta = -1$, $I = 1.53$ *and* $C = 5.1$

solution by means of switching waves which propagate outwards from the location of the initial spike. For values of the control parameter C below this instability threshold, the localised states exist and are stable in time until the point where the subcritical roll solution disappears. We also find that in the region where the L.S. is dynamically stable the amplitude of the initial pulse must exceed a certain threshold value or else the field does not form the L.S., but instead collapses to the homogeneous solution. On the other hand there seems to be no upper limit on the pulse amplitude: even amplitudes of up to 1000 units seem incapable of switching the field up to the pure roll solution.

The existence of a threshold for dynamic stability suggests that below this threshold a front separating regions of the pattern solution and the homogeneous solution tends to favour the latter. The reason that the homogeneous solution does not take over completely is due to a pinning of the switching-wave fronts on the diffraction ripples of the localised state, a mechanism investigated by Rosanov [52] in the context of so-called diffractive autosolitons. This observation from numerics then suggests that the dynamic stability threshold is associated

with a transition from the situation where the roll solution will invade the homogeneous solution to one where the homogeneous solution wants to invade the roll solution.

In addition to a single–peaked L.S. we can produce solutions corresponding to orbits in the phase space of system (5.3) which wrap around the roll limit cycle more than once before returning to the fixed point at the origin (Figure 5.3). Loosely speaking, the number of peaks produced depends on the width of the initial condition. However, things are slightly more complicated than this. We can choose a pulse width equivalent to a L.S. of m peaks and above a certain threshold amplitude this is what we will see. If the amplitude is increased, though, to the point where there is sufficient power in the wings of the initial pulse, the system will instead form separated localised states located near the wings of the pulse, corresponding instead to an orbit which leaves the origin, wraps around the limit cycle, returns close to the origin, returns to wrap around the limit cycle and returns to the origin again. For example, the differences in Figures 5.3(a) and 5.3(b) were produced simply by changing the amplitude of the initial condition. Thus a variety of different stable structures can be obtained simply by varying the initial condition.

This is about all we have to say about the one–dimensional localised states. Our basic understanding of them comes from a consideration of the phase space of the time–independent problem while investigation of their dynamic stability requires, at this moment in time, numerical simulations. Nevertheless, we have been able to demonstrate fairly convincingly that they do exist and are stable in time for certain parameter régimes.

5.3 Localised States in 2D

The nature of localised states is more difficult to visualise in two transverse dimensions, since even when $\partial_t A = 0$ there are still two independent variables, x

and y, in Equation (5.2). Despite this the system can be reduced to a one dimensional one in the special case in which we look for what we suppose will be a radially symmetric single localised state. If we work in cylindrical co–ordinates and define a variable $W = 1/r$ (5.2) can be written in the following autonomous form when there is no dependence on the azimuthal co–ordinate

$$\begin{aligned}
\frac{dU}{dr} &= -WU + \theta R + S + \frac{2CS}{1 + I\,(1 + 2R + R^2 + S^2)} \\
\frac{dR}{dr} &= U \\
\frac{dV}{dr} &= -WV + \theta S - R + \frac{2C(1 + R)}{1 + I\,(1 + 2R + R^2 + S^2)} + \frac{2C}{1 + I} \\
\frac{dS}{dr} &= V \\
\frac{dW}{dr} &= -W^2. \qquad (5.8)
\end{aligned}$$

We can do a linear stability analysis of the fixed point $(U_0, R_0, V_0, S_0, W_0) = (0, 0, 0, 0, 0)$. By inspection the only difference between the analysis for system (5.8) and that for (5.3) at the origin is that in the former case there is an additional eigenvalue ($\lambda = 0$) and associated eigenvector (parallel to the W–axis) attributable to the translational invariance of the solution. The other eigenvalues are the same as in the 1D case and the origin therefore has both a stable and an unstable manifold.

A numerical investigation of the localised states in two dimensions reveals behaviour which is similar to the 1D case. Again there is a threshold for dynamic stability, above which a pulse will either collapse to the plane–wave solution or, if its amplitude is sufficiently large, will initiate a switching wave which propagates outwards and switches the entire field to a space–dependent solution; the pattern formed in this way may be highly defected due to the curvature of the switching wave fronts as Figure 5.4 shows. We can infer, as in the 1D case, that the dynamic stability threshold is associated with an exchange of relative stability between the homogeneous and hexagon solutions.

Below the dynamical stability threshold an initial pulse of sufficiently large amplitude will create a single–peaked localised state (Figure 5.5) or, if it is broad

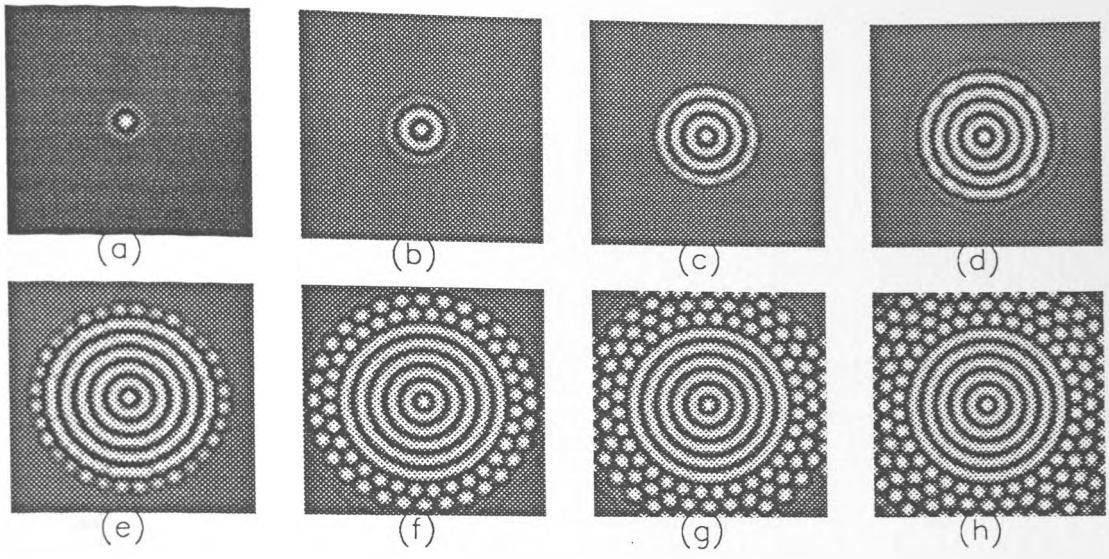

Figure 5.4: *Destabilisation of a 2D localised state with the resultant switching of the field to a patterned state through the propagation of a switching wave. The images show the real part of the field at (a) t=40, (b) t=80, (c) t=120, (d) t=160, (e) t=200, (f) t=240, (g) t=280 and (h) t=320 cavity lifetimes.* $\Delta = 0$, $\theta = -1$, $I = 1.53$ *and* $C = 5.56$

enough, a cluster of localised states arranged in some kind of pattern (Figure 5.6). Again, though, a pulse of sufficient width and amplitude will initiate localised states separated by a region of the homogeneous solution. For a radially symmetric initial condition this corresponds to a ring or annulus of localised states, as Figure 5.7 shows.

The connection between the isolated L.S. and the peak of a hexagonal pattern is suggested by Figure 5.8 which plots $Im(E)$ against $Re(E)$ for a section of the hexagonal pattern and for the L.S. showing that the L.S. tracks the hexagonal solution and then spirals off to the plane–wave fixed point, as the 1D localised state did with the stable roll solution. As in the 1D case there is no phase–winding associated with the localised states so that they do not appear to be topological in nature.

Since there is a danger that with no quantitative analytical backup the 2D localised states may just be numerical artefacts we can take advantage of the fact that the problem for a single localised state is essentially one–dimensional to provide an independent numerical check. We integrate the time–independent form

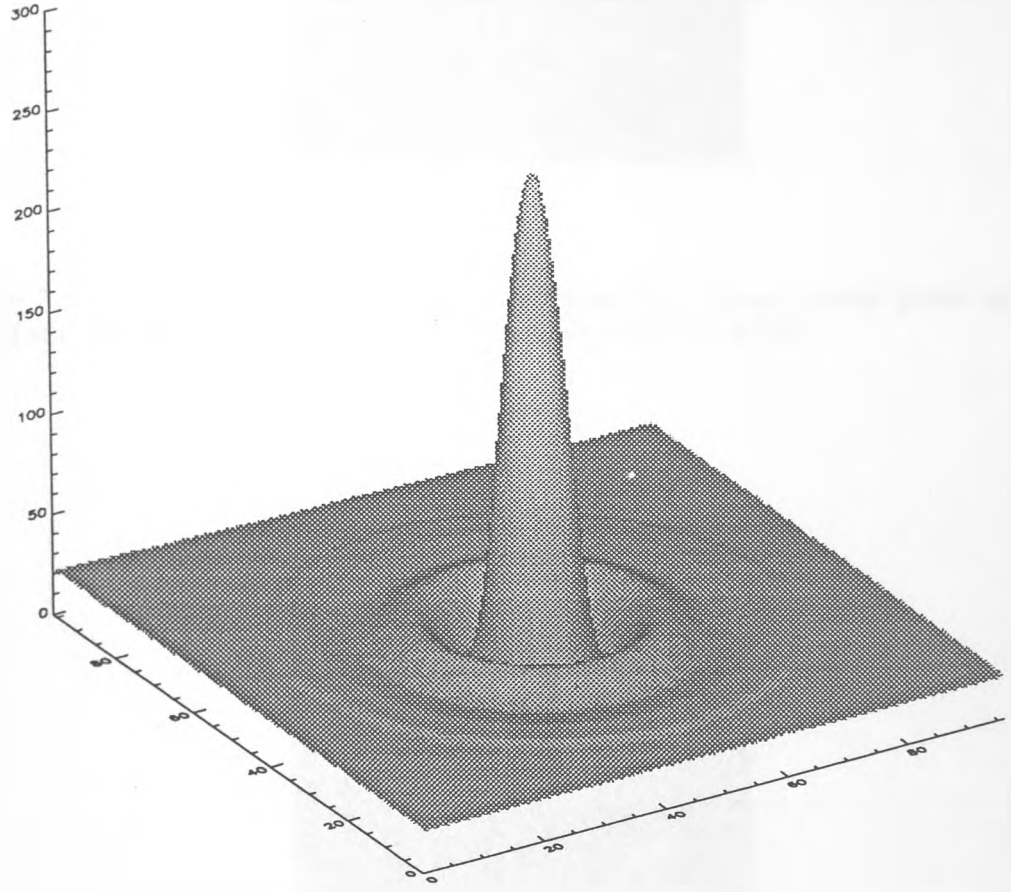

Figure 5.5: $|E|$ *plotted as a function of the transverse co-ordinates* x *and* y *(in arbitrary units) for a 2D localised state.* $\Delta = 0$, $\theta = -1$, $I = 1.53$ *and* $C = 5.4$

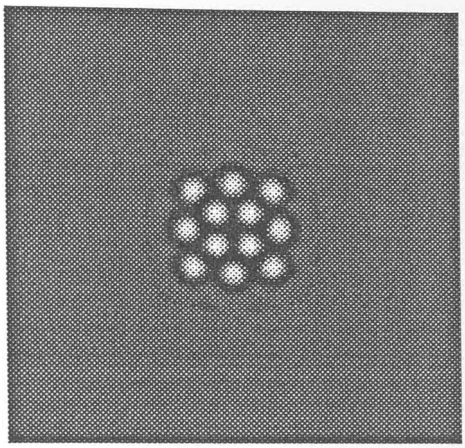

Figure 5.6: *Cluster of localised states produced by a broad initial pulse of peak amplitude 30 units.* $\Delta = 0$, $\theta = -1$, $I = 1.53$ *and* $C = 4.952$

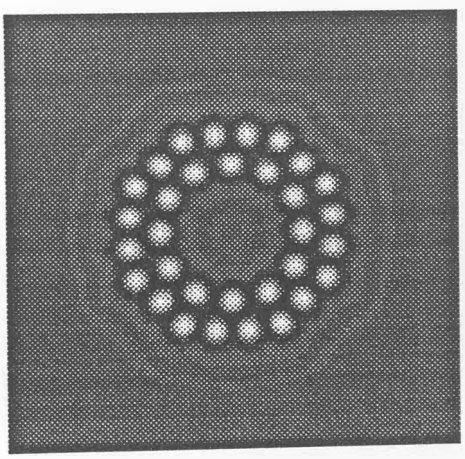

Figure 5.7: *"Annulus" of localised states produced by a broad initial pulse of peak amplitude 50 units.* $\Delta = 0$, $\theta = -1$, $I = 1.53$ *and* $C = 4.952$

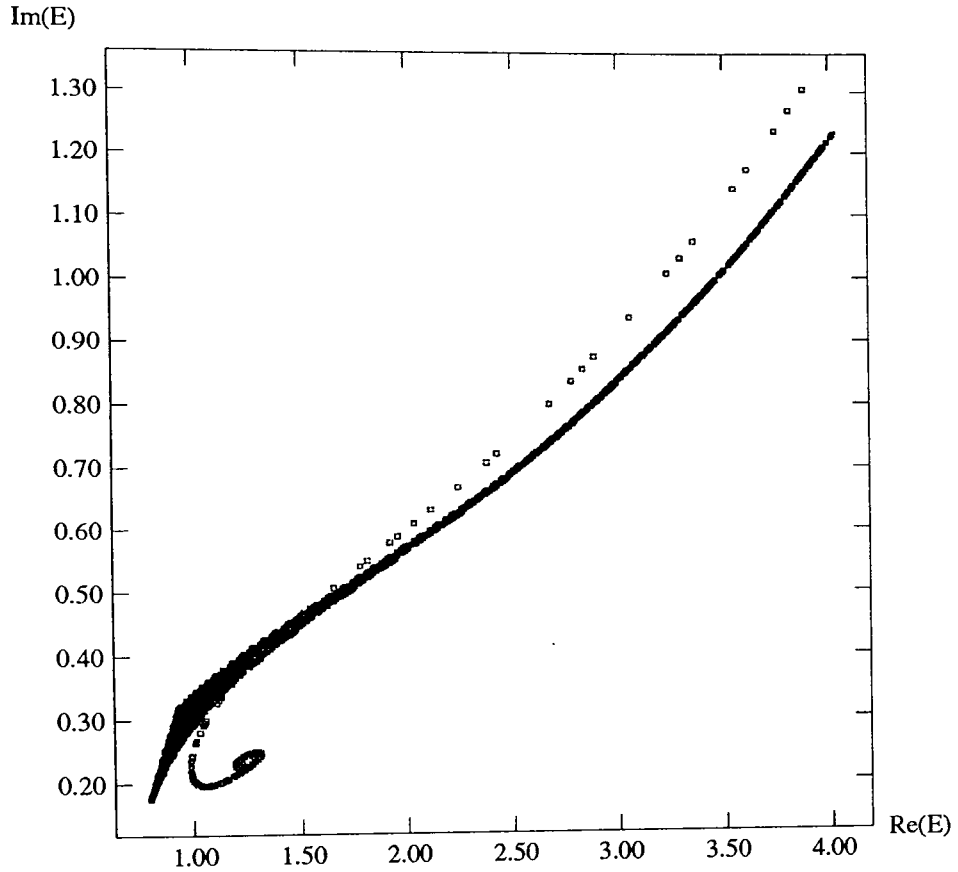

Figure 5.8: *$Im(E)$ plotted against $Re(E)$ for both the 2D localised state (blank squares) and the stable hexagon solution (solid black curve). The localised state spirals out from the plane–wave fixed point, tracks the hexagon solution and then spirals back in to the fixed point. The spread in the lower left part of the curve representing the hexagon solution is due to the variety of "routes" that the field can follow in two dimensions in going from a maximum of the pattern to a minimum.* $\Delta = 0$, $\theta = -1$, $I = 1.53$ *and* $C = 5.4$.

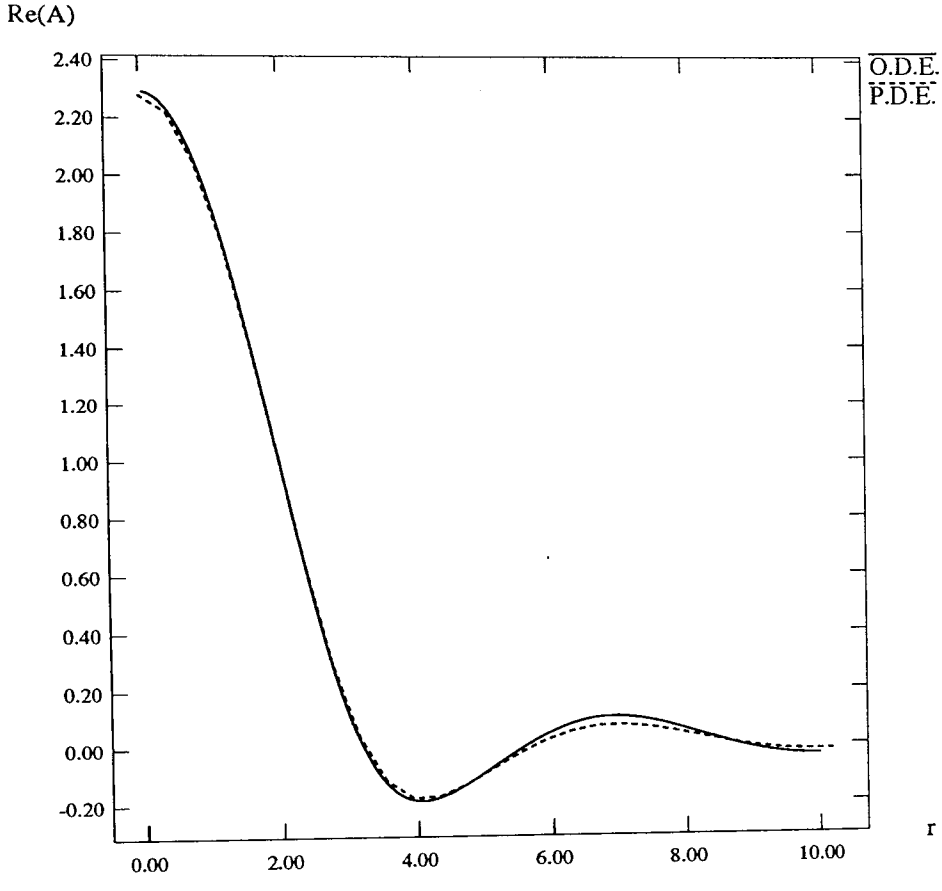

Figure 5.9: *Re(E) for the 2D localised state plotted against the radial co-ordinate r as calculated both by integration of the full P.D.E. and by integration in r of the time-independent dynamical system (5.8).* $\Delta = 0$, $\theta = -1$, $I = 1.53$ *and* $C = 5.4$

of Equation (5.2) in the radial co–ordinate by making a guess at the value of the field at $r = 0$ and then integrating outwards (a shooting method [47]). In general the solution will integrate forwards for a certain distance and then start to diverge. As our initial guess gets closer to one which actually corresponds to a solution of the equation, the distance to which the program can integrate before diverging increases, allowing us to home in on a solution. This process can be automated to some extent. We select a function, f, of the field which we wish to be minimal at some distance from the origin: for example, $f = |d_r A|^2$. We then select a value of r out to which we want to integrate so that we can calculate f for any pair of values we choose for $Re(A)$ and $Im(A)$ at the origin (the derivatives of both $Re(A)$ and $Im(A)$ must be zero at $r = 0$ in order to avoid a singularity). By this procedure we have defined f to be a function of two variables and so we just use a standard numerical technique (an AMOEBA routine [47]) to minimise f and give the closest approximation that we can find to the solution we are looking for, if it exists. When we do all of this we find that after a certain distance the integration method starts to diverge anyway due to numerical errors. It does allow us to integrate far enough, though, to get a solution which we can compare with the result from integration of the full P.D.E. As Figure 5.9 shows the agreement is quite good providing some evidence that the localised states are not just phenomena induced by the numerical grid.

5.4 Control of 2D Localised States

Equation (5.2) is translationally invariant which means that we can create a localised state at any point we wish and it should remain there; this is borne out by simulations. It also means, though, that the L.S. is neutrally stable with respect to changes in its position. In an experiment (or even a device) external perturbations which are inevitably present can therefore cause the L.S. to wander around after it has been created by a local address pulse. This is something to be avoided. In addition, for the purpose of writing and storing information we would like a system which allows a degree of imprecision about where our "pixels"

are written: as long as we write to approximately the right position, the system should be able to take the L.S. and put it exactly where it belongs.

All of this may seem like a bit of a tall order but in principle there is a way do it. We start off by pointing out an invariance which is possessed by Equation (5.2) and which has been observed in another nonlinear cavity model [53]. If we consider putting in a pump field which is tilted by an angle α with respect to the longitudinal axis of the cavity then it will take the form $E_I = E_{I_0} e^{i\mathbf{K}.\mathbf{x}}$ where $|\mathbf{K}| = k\sin(\alpha)$ and k is the component of the pump wavevector along its direction of propagation. We then expect a cavity field E of the form $E = Fe^{i\mathbf{K}.\mathbf{x}}$. From Equation (5.1) F must obey

$$\begin{aligned} D_t F &= -F - i[\theta + aK^2]F + E_{I_0} \\ &\quad -\frac{2C(1-i\Delta)F}{1+\Delta^2+|F|^2} + ai\nabla^2 F. \end{aligned} \tag{5.9}$$

Not surprisingly we see that the cavity detuning has been changed with respect to the one seen by a field driven by an on-axis pump. We also find that the partial derivative with respect to time has been changed to the convective derivative

$$D_t = \partial_t + (2a\mathbf{K}.\nabla). \tag{5.10}$$

The implication of this is that the solution we see should move with a velocity given by $2a\mathbf{K}$. In other words, the effect of tilting the pump beam is to produce solutions which, instead of being static, move in the transverse plane (assuming that the alteration of θ produces no qualitative change in behaviour by itself).

A solution which is uniformly translating is interesting but not very useful. Consider, however, generalising the above approach to the case where the input field has a space-dependent phase modulation:

$$E_I = E_{I_0} e^{i\phi(x,y)} \tag{5.11}$$

and again look for a cavity field of the form

$$E = Fe^{i\phi(x,y)}. \tag{5.12}$$

This time F obeys

$$D_t F = -[1 + a(\nabla^2\phi)]F - i[\theta + a(\nabla\phi).(\nabla\phi)]F + E_{I_0}$$

$$-\frac{2C(1 - i\Delta)F}{1 + \Delta^2 + |F|^2} + ai\nabla^2 F \tag{5.13}$$

with

$$D_t = \partial_t + (\mathbf{v}.\nabla) \tag{5.14}$$

where $\mathbf{v} = 2a(\nabla\phi)$. Again we have essentially the same form of equation as when the pump field is unmodulated, only now with spatially varying damping and detuning coefficients. More importantly, though, the velocity of the moving solution has acquired a spatial–dependence and is proportional to $\nabla\phi$. This means that if we initialise a localised state at some point it should move towards a local maximum of $\phi(x, y)$ and remain there.

If, for example, we choose ϕ to be of the form

$$\phi = \beta\,[\cos(m\pi x/L) + \cos(m\pi y/L)] \tag{5.15}$$

then we create a square array of local maxima which act as read/write locations for our "memory". All we have to do is fire a localised state into the region around the location to which we wish to write and the system itself will move the "pixel" into the correct place.

This is the principle but there is one thing about which one has to be careful. Since Equation (5.13) contains a spatially dependent damping the modulational instability threshold changes throughout the domain. If an L.S. is created at a point of the domain where it is dynamically stable and then starts to follow the phase gradient of the pump, it will see a steadily decreasing damping and will therefore be moving closer to the point where it destabilises in favour of the hexagon solution. This is what happens in the simulation shown in Figure 5.10. The localised state has not managed to reach the local maximum of $\phi(x, y)$ before $\nabla^2\phi$ becomes large and negative so that it destabilises and initiates a switching wave which spreads outwards and switches the whole field to the hexagon state.

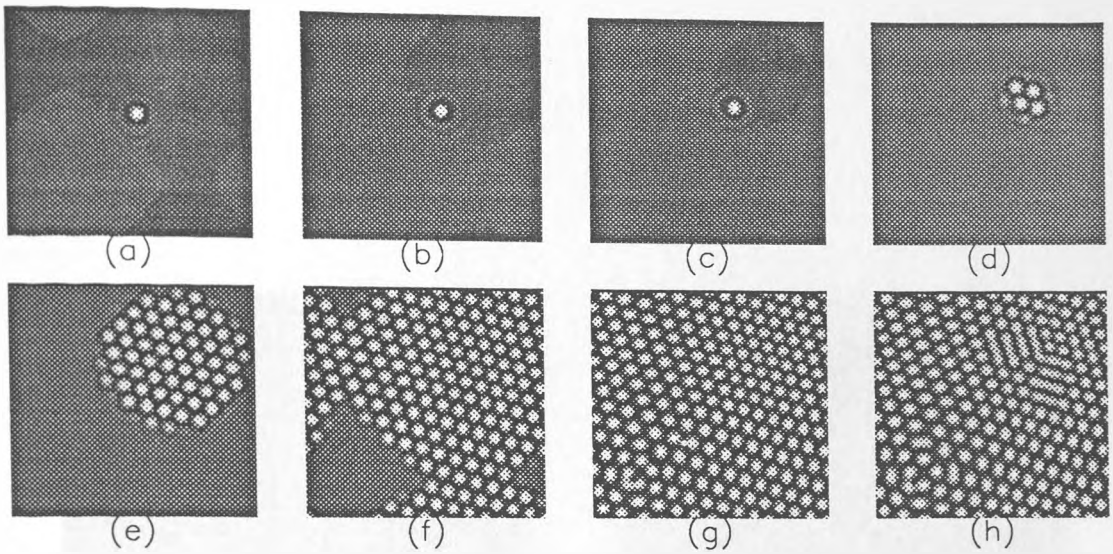

Figure 5.10: *Movement of a localised state up the phase gradient of a phase-modulated pump and subsequent destabilisation. The images show the real part of the field at (a) t=360, (b) t=720, (c) t=1080, (d) t=1400, (e) t=1540, (f) t=1680, (g) t=1820 and (h) t=1960 cavity lifetimes.* $\Delta = 0$, $\theta = -1$, $E_I = 6.63$, $C = 5.4$, $\beta = 0.1$ *and* $m = 2$.

Because of the phase moulation of the pump the hexagon pattern that results is not static; instead different parts of the pattern move in different directions and on the boundaries between two domains moving in opposite directions there is constant creation or annihilation of hexagonal spots. This is an interesting type of behaviour in its own right and one which may be experimentally observable.

There are two ways around this problem. The first is to make the depth of modulation of ϕ smaller but this will mean that the time taken for an L.S. to move to a maximum of ϕ will increase. The second method is to decrease the amplitude of the pump slightly so that even at a maximum of ϕ, the pump is not large enough to carry the L.S. out of its régime of dynamic stability. In the simulation whose result is pictured in Figure 5.11 the pump is smaller than that used for Figure 5.10 and we have created a four by four lattice of write locations. By producing a set of localised states in approximately the right positions we are able to write the letters "IT" as shown, indicating that this spatial addressing technique works, at least in simulations.

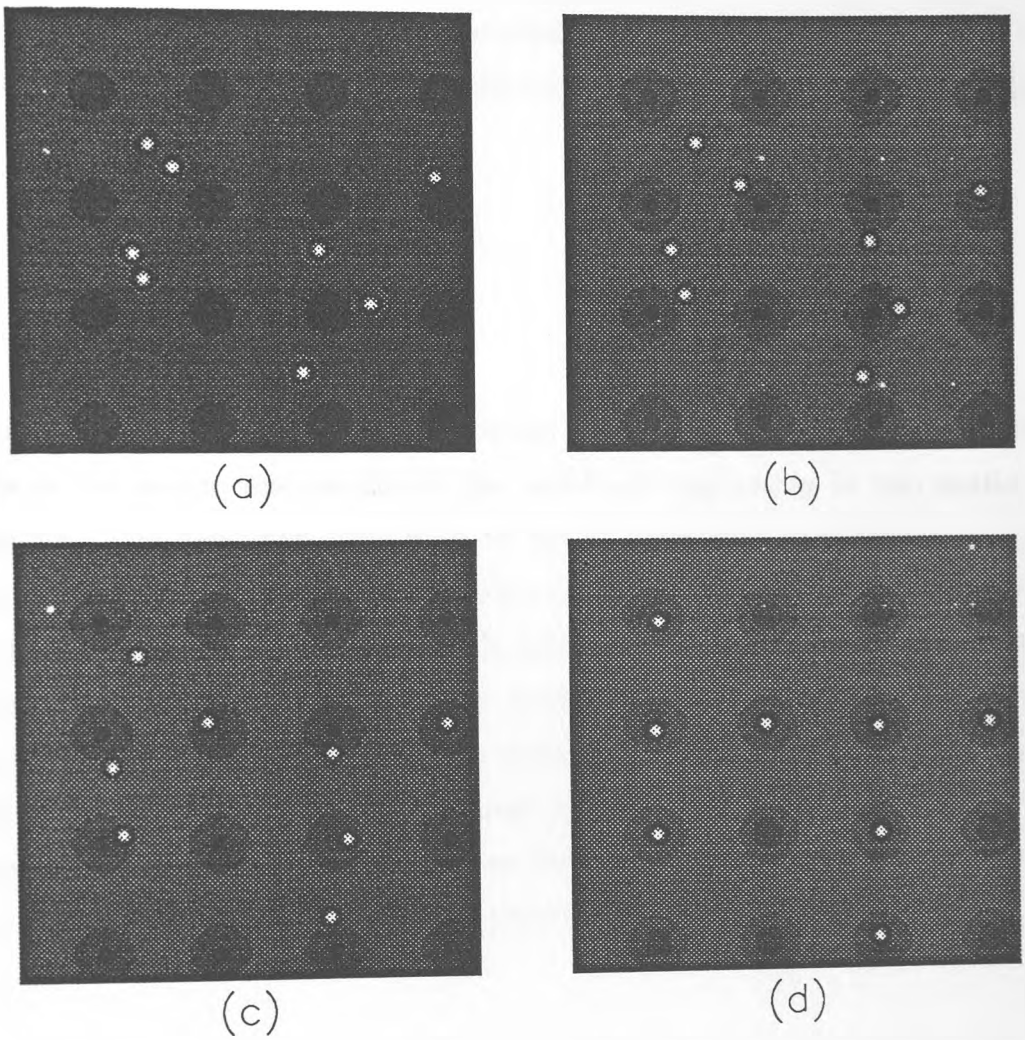

Figure 5.11: *Writing the letters IT in localised states.* $\Delta = 0$, $\theta = -1$, $I = 1.53$ *and* $C = 5.4$. *Real part of the field at (a) t=20, (b) t=160, (c) t=300 and (d) t=800 cavity lifetimes.*

One final question that we can ask is what happens if two localised states are written to the same point, for example as the result of a writing error in a device. Simulations show that in this case both spots move towards the appropriate location and when they get close enough to interact they lock onto each other's diffraction ripples and so remain stable. It might be preferable if the localised states annihilated each other so that the error could be corrected by simply writing to the required memory locations a second time. However, at least in this way the error does not corrupt the information stored elsewhere but remains local and can still be detected and corrected.

5.5 Conclusion

In this chapter we have provided numerical evidence for the existence of localised states in the mean–field model of the two–level ring cavity in two spatial dimensions. The next step should be to try to determine analytically, or semi–analytically, their existence and stability properties, although it is not obvious how to do this at the present time. In addition we have suggested one method for the control of such solutions in two transverse dimensions and demonstrated that it works, at least in simulations. Although the two–level ring cavity is not a realistic system for a practical optical memory, the study and control of localised states in simple systems such as this one will be necessary if they are to be exploited for applications at some time in the future.

Chapter 6

Conclusion

This thesis has been about transverse pattern formation in passive nonlinear optical systems, and in particular about behaviour close to the region where a homogeneous solution becomes unstable with respect to one with transverse structure. In the two systems examined we used standard mathematical techniques of linear stability analysis, weakly nonlinear analysis and finally numerical integration to locate the instability threshold of the flat solution and to determine the nature of the pattern which will emerge above this threshold, with reasonable success. We also made use of the knowledge gained by this process in the two–level ring cavity system to begin a study of the solitary wave structures known as localised states, demonstrating their existence and one possible method for their control. It only remains, now, to point out some of the ways in which this work can be continued and extended.

In the feedback mirror system we examined the case of plane–wave pumping but the effects of a finite pump should also be looked at, particularly in the light of the experimental results published in [34] which show flower–like patterns in the system on which Chapter 4 is based. It is also possible to generalise the model of Chapter 4 to take into account the effects of external magnetic fields which would allow it to describe the experiment of [35].

In neither the two–level cavity nor the four–level feedback mirror system has any attempt been made to study secondary bifurcations. It is possible that the uniform pattern solution itself becomes unstable far enough above threshold leading perhaps to solutions which oscillate in time or even to weakly turbulent behaviour.

Finally, it is necessary to try to find analytical or semi–analytical approaches to investigate the questions of existence and dynamical stability of localised states rather than relying simply on numerical integration of the model P.D.E. While the latter is indispensible a deeper understanding of these structures is, at the very least, desirable.

Appendix A

Numerical Methods

In this appendix we outline the two techniques used in this thesis to integrate P.D.E.s numerically: the split–step method [54] and the hopscotch method [55].

A.1 The Split–step Method

We consider equations of the form

$$\partial_t E = \hat{\mathcal{L}} E \tag{A.1}$$

where $\hat{\mathcal{L}}$ is an operator which contains no explicit time–dependence. Equation (A.1) can be formally integrated to give E at some time in terms of its value at an earlier time:

$$E(t + dt) = e^{dt\hat{\mathcal{L}}} E(t). \tag{A.2}$$

Now assume that $\hat{\mathcal{L}}$ can be written as the sum of two terms

$$\hat{\mathcal{L}} = \hat{\mathcal{L}}_1 + \hat{\mathcal{L}}_2 \tag{A.3}$$

and further assume that the error introduced by neglecting $[\hat{\mathcal{L}}_1, \hat{\mathcal{L}}_2]$ is of high enough order that we can write (A.2) as

$$E(t + dt) \simeq e^{dt\hat{\mathcal{L}}_1} e^{dt\hat{\mathcal{L}}_2} E(t). \tag{A.4}$$

In fact, it can be shown that the error introduced by neglecting $[\hat{\mathcal{L}}_1, \hat{\mathcal{L}}_2]$ can be reduced if we write (A.2) as

$$E(t+dt) \simeq e^{(dt/2)\hat{\mathcal{L}}_2} e^{dt\hat{\mathcal{L}}_1} e^{(dt/2)\hat{\mathcal{L}}_2} E(t). \tag{A.5}$$

$E(t+dt)$ is now calculated in three steps. We first calculate E' as the solution at $t = dt/2$ of the equation

$$\partial_t F = \hat{\mathcal{L}}_2 F \tag{A.6}$$

with initial condition $F(0) = E(t)$. Then we solve for E'' given by $F(dt)$ where

$$\partial_t F = \hat{\mathcal{L}}_1 F \tag{A.7}$$

and $F(0) = E'$. Finally, $E(t+dt)$ is given by solving (A.6) at time $t = dt/2$ with initial condition given by E''.

To calculate $E(t = ndt)$ the above procedure is carried out repeatedly. Thus

$$E(t) = e^{dt/2\hat{\mathcal{L}}_2} e^{dt\hat{\mathcal{L}}_1} e^{dt\hat{\mathcal{L}}_2} ... e^{dt\hat{\mathcal{L}}_2} e^{dt\hat{\mathcal{L}}_1} e^{dt/2\hat{\mathcal{L}}_2} E(0). \tag{A.8}$$

The motivation behind this method lies in finding a splitting of $\hat{\mathcal{L}}$ such that Equations (A.6) and (A.7) can each be solved fairly easily. Equations studied in optics, for example the ring–cavity equation of Chapter 3, often take the form

$$\partial_t E = a\nabla^2 E + g(E) \tag{A.9}$$

where g is a nonlinear function which contains no spatial dependence and a is a complex number. The most obvious splitting then reduces (A.6) and (A.7) to

$$\partial_t E = a\nabla^2 E \tag{A.10}$$

and

$$\partial_t E = g(E) \tag{A.11}$$

respectively.

Equation (A.10) is solved easily in Fourier space by using a Fast Fourier Transform [47] and then taking the inverse transform to convert back to real space, a process which is $O(ds^N)$ where ds is the space step and N is the dimension of the grid.

Since (A.11) contains no spatial dependence it can be solved at each point of the numerical grid using a standard technique for the solution of O.D.E.s. For example, the code used to produce the results described in Chapter 3 used a second order Runge–Kutta method ($O(dt^2)$) [47].

A.2 The Hopscotch Method

This technique is used for equations of the form

$$\partial_t E = \hat{\mathcal{L}} E + g(E) \tag{A.12}$$

where $\hat{\mathcal{L}}$ is a linear operator and g a nonlinear function. The method relies on a partition of the lattice points (i, j) of the numerical grid into two sets, denoted "odd" and "even"

$$\begin{aligned} \text{ODD GRID} &= \{(i,j) : i+j \text{ is odd}\} \\ \text{EVEN GRID} &= \{(i,j) : i+j \text{ is even}\} \end{aligned} \tag{A.13}$$

so that each lattice point is surrounded by four nearest neighbours on the other grid.

The first step of the algorithm involves advancing the solution from time $t = ndt$ to time $t = (n+1)dt$ on the odd grid by means of an explicit method:

$$E^{n+1} \simeq E^n + dt \left[\hat{\mathcal{L}} E^n + g(E^n)\right]. \tag{A.14}$$

We then advance the even grid by an implicit method

$$E^{n+1} \simeq E^n + dt \left[\hat{\mathcal{L}} E^{n+1} + g(E^{n+1})\right]. \tag{A.15}$$

To carry out this step we have to be able to solve (A.15) for E^{n+1}. This can be done for the linear part if the only spatial dependence contained in $\hat{\mathcal{L}}$ is of the form $a\nabla^2$, as it is in many of the equations in which we are interested. Then we can use the standard four–point finite difference approximation for ∇^2:

$$\nabla^2 E_{i,j} \simeq \frac{1}{h^2}\left(E_{i,j+1} + E_{i,j-1} + E_{i+1,j} + E_{i-1,j} - 4E_{i,j}\right) \tag{A.16}$$

where h is the space step, assumed to be the same in both the x and $y-$ directions. Since this expression involves only the nearest neighbours to the point (i,j) all of which lie on the odd grid and whose values are now known at time $(n+1)dt$, we can solve the linear part for $E_{i,j}^{n+1}$. In general we cannot solve the nonlinear part, so we make an approximation to $g(E_{i,j}^{n+1})$:

$$g(E_{i,j}^{n+1}) \simeq g\left(\frac{E_{i,j+1}+E_{i,j-1}+E_{i+1,j}+E_{i-1,j}}{4}\right). \tag{A.17}$$

This enables us to advance the even grid by one time step so that we now know the entire field at time $(n+1)dt$. The algorithm now proceeds by performing the explicit step on the even grid and the implicit step on the odd grid and so on.

The speed of the method can be improved by omitting the explicit steps except for the initial one at $t=0$. We advance the odd grid by one time step using the explicit step. We then advance the even grid by one time step by the implicit step. Now we advance the even grid by a further time step using the expression

$$E^{n+2} \simeq 2E^{n+1} - E^{n}. \tag{A.18}$$

We then advance the odd grid by two time steps and so on. It is this alternate advancement of the two grids that gives the method its name.

For equations of the form (A.9) the finite difference expression used to evaluate ∇^2 means that the method is second order in space as well as being second order in time.

Appendix B

Four–Level Bloch Equations

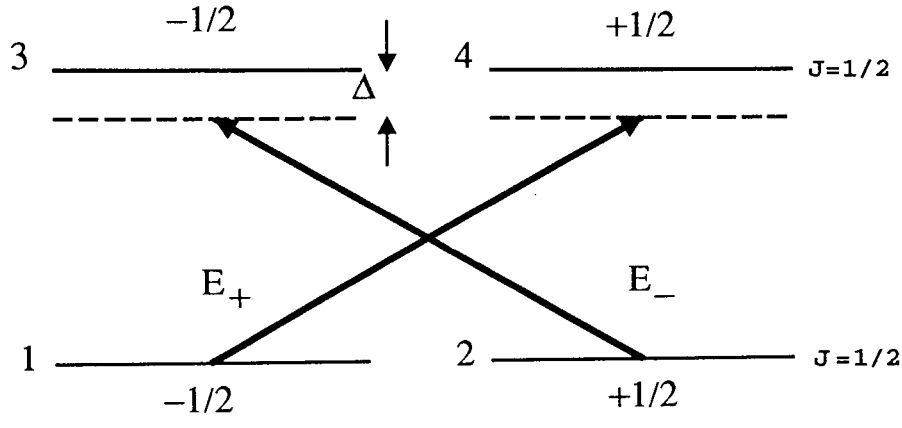

Figure B.1: *Energy level diagram for the four–level system.*

In this appendix we apply the procedure of Chapter 2 to write down Bloch equations for the four–level system shown in Figure B.1 and studied in Chapter 4. Our treatment follows [46] whose notation we use.

We use a circular basis and write the electric field as

$$\mathcal{E} = -\frac{1}{2}\left(E_- e^{i\omega t}\hat{e}_+ - E_-^* e^{-i\omega t}\hat{e}_- + E_+ e^{i\omega t}\hat{e}_- - E_+^* e^{-i\omega t}\hat{e}_+\right) \qquad \text{(B.1)}$$

where

$$\hat{e}_{\pm} = \mp\frac{1}{\sqrt{2}}\left(\hat{e}_x \pm i\hat{e}_y\right). \tag{B.2}$$

The only non–zero dipole matrix elements are $\langle 3|-\boldsymbol{\mu}.\mathbf{E}|2\rangle$ and $\langle 4|-\boldsymbol{\mu}.\mathbf{E}|1\rangle$. $\boldsymbol{\mu}$ is the sum of three terms which transform like the components of a spherical tensor operator of rank 1 so that applying the Wigner–Eckart theorem [56] gives the following expressions for the non–zero matrix elements

$$\begin{aligned}
\langle 3|-\boldsymbol{\mu}.\mathbf{E}|2\rangle &= \hbar\beta_+ e^{i\omega t} - \hbar\beta_-^* e^{-i\omega t} \\
\langle 4|-\boldsymbol{\mu}.\mathbf{E}|1\rangle &= -\hbar\beta_- e^{i\omega t} + \hbar\beta_+^* e^{-i\omega t}
\end{aligned} \tag{B.3}$$

where $\beta_{\pm} = \mu_E E_{\pm}/2\hbar$.

In order to remove terms of the form $e^{i\pm\omega t}$ from the Bloch equations we define

$$\tilde{\rho}_{ij} = \rho_{ij} e^{i\omega t} \qquad i = 3,4, \quad j = 1,2. \tag{B.4}$$

An application of Equation (2.32) then yields the following set of equations for the matrix elements, ρ_{ij}, of the density operator

$$\begin{aligned}
\partial_t\rho_{11} &= i(\beta_+^*\tilde{\rho}_{14} - \beta_+\tilde{\rho}_{41}) - \gamma_1(\rho_{11}-\rho_{22}) + \gamma_2(\rho_{33}+\rho_{44}) \\
\partial_t\rho_{22} &= i(\beta_-\tilde{\rho}_{32} - \beta_-^*\tilde{\rho}_{23}) + \gamma_1(\rho_{11}-\rho_{22}) + \gamma_2(\rho_{33}+\rho_{44}) \\
\partial_t\rho_{33} &= -i(\beta_-\tilde{\rho}_{32} - \beta_-^*\tilde{\rho}_{23}) - \gamma_3(\rho_{33}-\rho_{44}) - 2\gamma_2\rho_{33} \\
\partial_t\rho_{44} &= -i(\beta_+^*\tilde{\rho}_{14} - \beta_+\tilde{\rho}_{41}) + \gamma_3(\rho_{33}-\rho_{44}) - 2\gamma_2\rho_{44} \\
\partial_t\rho_{12} &= -i(\beta_+\tilde{\rho}_{42} + \beta_-^*\tilde{\rho}_{13}) - \gamma_4\rho_{12} \\
\partial_t\rho_{34} &= i(\beta_-^*\tilde{\rho}_{24} + \beta_+\tilde{\rho}_{31}) - \gamma_5\rho_{34} \\
\partial_t\tilde{\rho}_{13} &= (i\Delta - \gamma_6)\tilde{\rho}_{13} - i(\beta_+\rho_{43} + \beta_-\rho_{12}) \\
\partial_t\tilde{\rho}_{14} &= (i\Delta - \gamma_6)\tilde{\rho}_{14} + i\beta_+(\rho_{11}-\rho_{44}) \\
\partial_t\tilde{\rho}_{23} &= (i\Delta - \gamma_6)\tilde{\rho}_{23} - i\beta_-(\rho_{22}-\rho_{33}) \\
\partial_t\tilde{\rho}_{24} &= (i\Delta - \gamma_6)\tilde{\rho}_{24} + i(\beta_-\rho_{34} + \beta_+\rho_{21}).
\end{aligned} \tag{B.5}$$

We now assume that the populations of the excited–states relax very rapidly so that $\rho_{33}, \rho_{44}, \rho_{34} \simeq 0$. We also assume that the time scale for the evolution of

the ground–state variables is longer than the scale of the evolution of the other variables; then we can adiabatically eliminate ρ_{13}, ρ_{14}, ρ_{23} and ρ_{24}. We then have

$$\begin{aligned}
\tilde{\rho}_{13} &= \frac{\beta_-}{\Delta + i\gamma_6}\rho_{12} \\
\tilde{\rho}_{14} &= \frac{-\beta_+}{\Delta + i\gamma_6}\rho_{11} \\
\tilde{\rho}_{23} &= \frac{\beta_-}{\Delta + i\gamma_6}\rho_{22} \\
\tilde{\rho}_{24} &= \frac{-\beta_+}{\Delta + i\gamma_6}\rho_{21}.
\end{aligned} \tag{B.6}$$

Now we define

$$\gamma = 2\gamma_1, \quad \Gamma = \gamma_6, \quad \bar{\Delta} = \frac{\Delta}{\Gamma}, \quad \Lambda_\pm = \frac{|\beta_\pm|^2}{\Gamma(1+\bar{\Delta}^2)} \tag{B.7}$$

and the new variables

$$u = \rho_{12} + \rho_{21}, \quad v = i(\rho_{12} - \rho_{21}), \quad w = \rho_{11} - \rho_{22}. \tag{B.8}$$

The remaining Bloch equations written in terms of u, v and w are then

$$\begin{aligned}
\partial_t u &= -(\Lambda_+ + \Lambda_- + \gamma)\, u - (\Lambda_- - \Lambda_+)\, \bar{\Delta} v \\
\partial_t v &= -(\Lambda_+ + \Lambda_- + \gamma)\, v + (\Lambda_- - \Lambda_+)\, \bar{\Delta} u \\
\partial_t w &= -(\Lambda_+ + \Lambda_- + \gamma)\, w + (\Lambda_- - \Lambda_+).
\end{aligned} \tag{B.9}$$

It can be seen that the equation for w is decoupled from the other equations.

We now want an equation for the polarisation, $\mathcal{P}$, which we decompose onto the circular basis as we did for the electric field

$$\begin{aligned}
\mathcal{P} &= -\frac{1}{2}\left(P_- e^{i\omega t}\hat{e}_+ - P_-^* e^{-i\omega t}\hat{e}_- + P_+ e^{i\omega t}\hat{e}_- - P_+^* e^{-i\omega t}\hat{e}_+\right) \\
&= n_a Tr\left(\boldsymbol{\mu}\rho\right)
\end{aligned} \tag{B.10}$$

where n_a is the number density of atoms. Using Equations (B.6) we find the following expressions for $P_\pm$

$$\begin{aligned}
P_\pm &= \frac{n_a \mu^2 (\bar{\Delta} - i)}{2\hbar\Gamma(1+\bar{\Delta}^2)}(1 \pm w)E_\pm \\
&= \epsilon_0 \chi_\pm E_\pm.
\end{aligned} \tag{B.11}$$

We therefore see that $P_\pm$ depend only on w so that the medium can be described by the equation of motion for w in Equations (B.9).

Bibliography

[1] M. C. Cross and P. C. Hohenberg, Rev.Mod.Phys. **65**, 851 (1993)

[2] H. M. Gibbs, *Optical Bistability: Controlling Light with Light*, Academic, Orlando (1985)

[3] J. V. Moloney and H. M. Gibbs, Phys.Rev.Lett.**48**, 1607 (1982);
J. V. Moloney, H. Adachihara, D. W. McLaughlin and A. C. Newell, in *Chaos, Noise and Fractals*, eds. R. Pike and L. A. Lugiato, Hilger, Bristol, 1988

[4] J. V. Moloney, H. Adachihara, R. Indik, C. Lizaragga, R. Northcutt, D. W. McLaughlin and A. C. Newell, J.Opt.Soc.Am. B **7**, 1039 (1990)

[5] G. S. McDonald and W. J. Firth, J.Opt.Soc.Am.B **7**, 1328 (1990);
G. S. McDonald and W. J. Firth, J.Opt.Soc.Am.B **10**, 1081 (1993)

[6] L. A. Lugiato and C. Oldano, Phys.Rev. A **37**, 3896 (1988)

[7] W. J. Firth and A. J. Scroggie, Europhys. Lett. **26**, 521 (1994)

[8] Paul Mandel, M. Georgiou and T. Erneux, Phys.Rev. A **47**, 4277 (1993)

[9] M. Tlidi and Paul Mandel, Special issue on "Nonlinear Optical Systems, Chaos, Noise", to appear in *Chaos, Solitons and Fractals*

[10] L. A. Lugiato and R. Lefever, Phys.Rev.Lett. **58**, 2209 (1987)

[11] W. J. Firth, A. J. Scroggie, G. S. McDonald and L. A. Lugiato, Phys.Rev. A **46**, R3609 (1992)

[12] J. B. Geddes, J. V. Moloney, E. M. Wright and W. J. Firth, Opt.Commun. **111**, 623 (1994)

[13] P. La Penna and G. Giusfredi, Phys.Rev. A, **48**, 2299 (1993)

[14] G. Grynberg, E. Le Bihan, P. Verkerk, P. Simoneau, J. R. R.Leite, D. Bloch, S. Le Boiteux and M. Ducloy, Opt.Commun. **67**, 363 (1988)

[15] J. Pender and L. Hesselink, J.Opt.Soc.Am. B **7**, 1361 (1990)

[16] A. Petrossian, M. Pinard, A. Maitre, J. Y. Courtois and G. Grynberg, Europhys.Lett. **18**, 689 (1992)

[17] W. J. Firth and C. Paré, Opt.Lett. **13**, 1096 (1988)

[18] W. J. Firth, A. Fitzgerald and C. Paré, J.Opt.Soc.Am. **B7**, 1089 (1990)

[19] G. Grynberg, Opt.Commun. **66**, 321 (1988)

[20] G. Grynberg and J. Paye, Europhys.Lett. **8**, 29 (1989)

[21] J. Y. Courtois and G. Grynberg, Opt.Comm. **87**, 186 (1992)

[22] R. Chang, W. J. Firth, R. Indik, J. V. Moloney and E. M. Wright, Opt. Commun. **88**, 167 (1992)

[23] J. B. Geddes, R. A. Indik, J. V. Moloney and W. J. Firth, Phys.Rev. A **50**, 3471 (1994)

[24] W. J. Firth, J.Mod.Opt. **37**, 151 (1990)

[25] G. D'Alessandro and W. J. Firth, Phys.Rev.Lett. **66**, 2597 (1991); G. D'Alessandro and W. J. Firth, Phys.Rev.A **46**, 537 (1992)

[26] F. Papoff, G. D'Alessandro, G. L. Oppo and W. J. Firth, Phys.Rev.A **48**, 634 (1993)

[27] R. Macdonald and H. J. Eichler, Opt.Commun. **89**, 289 (1992)

[28] M. Tamburrini, M. Bonavita, S. Wabnitz and E. Santamato, Opt.Lett. 18, 855 (1993)

[29] B. Thüring, R. Neubecker and T. Tschudi, Opt. Commun. **102**, 111 (1993)

[30] R. Neubecker, B. Thüring and T. Tschudi, Special issue on "Nonlinear Optical Systems, Chaos, Noise", to appear in *Chaos, Solitons and Fractals*

[31] E. Pampaloni, S. Residori and F. T. Arecchi, Europhys. Lett. **24**, 647 (1993)

[32] E. Pampaloni, S. Residori, P.–L. Ramazza and F. T. Arecchi, Europhys. Lett. **25**, 587 (1994)

[33] R. Neubecker, G.–L. Oppo, B. Thüring and T. Tschudi, submitted to Phys. Rev. A

[34] G. Grynberg, A. Maitre and A. Petrossian, Phys. Rev. Lett. **72**, 2379 (1994)

[35] T. Ackemann and W. Lange, Phys. Rev. A **50**, R1 (1994)

[36] Melvin Lax, William H. Louisell and William B. McKnight, Phys. Rev. A **11**, 1365 (1975)

[37] R. Loudon, *The Quantum Theory of Light* (2nd edition), Oxford University Press (1983)

[38] A. C. Newell and J. V. Moloney, *Nonlinear Optics*, Addison–Wesley (1992)

[39] M. Haelterman, G. Vitrant and R. Reinisch, J. Opt. Soc. Am. B **7**, 1309 (1990)

[40] G.-L. Oppo, G. D'Alessandro and W. J. Firth, Phys. Rev. A **44**, 4712 (1991)

[41] P. Manneville *Dissipative Structures and Weak Turbulence*, Academic Press, San Diego (1990)

[42] A. C. Newell, T. Passot and J. Lega, Annu. Rev. Fluid Mech. **25**, 399 (1993)

[43] S. Ciliberto, P. Coullet, J. Lega, E. Pampaloni and C. Perez–Garcia, Phys.Rev.Lett. **65**, 2370 (1990)

[44] P. K. Jakobsen, J. V. Moloney, A. C. Newell and R. Indik, Phys.Rev.A **45**, 8129 (1992)

[45] G.-L. Oppo, M. Brambilla and L. A. Lugiato, Phys.Rev.A **49**, 2028 (1994)

[46] F. Mitschke, R. Deserno, W. Lange and J. Mlynek, Phys. Rev. A **33**, 3219 (1986)

[47] W. H. Press, B. P. Flannery, S. A. Teukolsky and W. T. Vetterling, *Numerical Recipes: The Art of Scientific Computing*, Cambridge University Press, 1986.

[48] L. Gil, Ph.D. Thesis, University of Nice (1989)

[49] W. van Saarloos and P. C. Hohenberg, Phys. Rev. Lett. **64**, 749 (1990)

[50] M. Tlidi, Paul Mandel and R. Lefever, Phys. Rev. Lett. **73**, 640 (1994)

[51] John Guckenheimer and Philip Holmes, *Nonlinear Oscillations, Dynamical Systems, and Bifurcations of Vector Fields*, Springer (1983)

[52] N. N. Rosanov, SPIE **1840**, 130 (1991)

[53] M. Haelterman and G. Vitrant, J. Opt. Soc. Am. B **9**, 1563 (1992)

[54] R. H. Hardin and F. D. Tappert, SIAM Rev. **15**, 423 (1973)

[55] A.R. Gourlay, J. Inst. Math. Applics. **6**, 375 (1970); A.R. Gourlay, G.R. MacGuire, J. Inst. Math. Applics. **7**, 216 (1971)

[56] A. Messiah, *Quantum Mechanics* (Vol. II), North–Holland (1966)